Search for New Heavy Neutral Gauge Bosons in $\sqrt{s} = 8$ TeV pp Collisions with ATLAS

Yan-Jie Schnellbach
September 2014

Thesis submitted in accordance with the requirements of
the University of Liverpool for the degree of Doctor in Philosophy

Abstract

This thesis describes the search for new heavy neutral gauge bosons decaying into di-electron pairs, focussing on the Z'_{SSM} boson described by the Sequential Standard Model. The analysis uses $20.3\,\text{fb}^{-1}$ of pp collisions at $\sqrt{s} = 8\,\text{TeV}$ recorded with the ATLAS detector during the 2012 data taking period at the Large Hadron Collider at CERN. The invariant mass spectrum of di-electron pairs is used as the search variable and is analysed in the region $80\,\text{GeV} < m_{ee} < 4500\,\text{GeV}$. The spectrum is compared to the Standard Model expectation dominated by the neutral current Drell-Yan process. Several novel techniques are developed to improve the description of both, the Drell-Yan process and photon-induced di-lepton production. As no significant excess is found in the data, statistical techniques are used to interpret the result as limits on the production and decay of a new heavy gauge boson. A 95% C.L. Bayesian lower limit is set on the Z'_{SSM} mass at 2.78 TeV with a corresponding upper limit on the Z'_{SSM} cross-section times branching ratio $\sigma \times Br(Z'_{SSM} \to e^+e^-)$ of $3.53 \times 10^{-4}\,\text{pb}$.

Declaration

This dissertation is the result of my own work, except where explicit reference is made to the work of others, and has not been submitted for another qualification to this, or any other, university. This dissertation does not exceed the word limit for the respective Degree Committee.

Yan-Jie Schnellbach

Acknowledgements

This thesis and the work behind it have been an exciting and interesting journey, a journey that was not made alone, so I owe my thanks to many, many people:

First of all, I would like to thank my PhD supervisors, Uta Klein and Jan Kretzschmar, not only for your advice, collaboration and being deeply knowledgable about parton distribution functions and ATLAS electrons alike, but also for your support, patience and wisdom. My thanks and gratitude also go to whole Liverpool HEP group, the HEP computing staff, the University of Liverpool and the Science and Technology Facilities Council for their support, funding and organising my stay at CERN, keeping things running and their ability to put up with us PhD students year after year.

Furthermore, I want to extend my thanks to the people of the ATLAS Z' and the Mainz ATLAS group, in particular, Paul Bell, Rozmin Daya, Dan Hayden and Simon Viel; I have learnt a lot working with you (too many things to list!). And while it has been some time, I would not have made it this far if not for my physics teacher Werner Marré back home and my MPhys supervisor Terry Wyatt in Manchester.

Also, thanks for the fun times together, Miffy, Will, Alex, Rik, Greg, Danny, Joe, Pete, "Ken", Henry, Harvey, Ben and Dean, my fellow PhD students; you were invaluable sources of support, advice, fun, cake, weirdness, dice-rolling and pizza evenings.

And, of course, lots of love to Kirsty, for all your love and your patience with me while I was pouring my hours and (too) many weekends into this thesis.

Finally, my utmost and deepest thanks and love to you, Andreas, Thuy-Thanh and Yan-Ting, my dad, my mom and my sister. For everything.

Contents

Introduction

"One should never mistake pattern for meaning."
— Iain M. Banks, *The Hydrogen Sonata*

Curiosity has always been a basic human drive, making us interested in the world surrounding us and what comprises that world. The continuing study of nature has led us to many successful theories capable of powerful predictions. One of humanity's most consistent and successful theories is the Standard Model of particle physics, describing the most basic constituents of all currently known matter.

Developed during the 20^{th} century, the Standard Model not only described existing phenomena extraordinarily well, its predictive qualities led to the discovery of the Z boson in the early 80s as well as to the discovery of the Higgs bosons in mid-2012. Despite its success, however, it does not incorporate another extremely successful theory of the 20^{th} century, the general theory of relativity which describes gravitation. Furthermore, other observations, including dark matter, dark energy, the matter/antimatter asymmetry seen in the universe and the existence of neutrino masses hint at physics beyond the Standard Model.

In order to test the Standard Model, particle physics has a tradition of using collider experiments to reach the high energies required to study the Standard Model. The Large Hadron Collider at CERN is the latest such experiment, providing the highest energy collisions currently achievable. In order to observe and study these collisions, the ATLAS detector is used to detect, identify, record and reconstruct particles produced in the collisions.

This thesis describes the search for a new heavy ($> 150\,\text{GeV}$) neutral gauge boson using the ATLAS detector. As such a particle would be very short-lived, the decay products of said new particle are sought, specifically an electron-positron pair. By comparing the invariant mass spectrum of all recorded electron pairs with the Standard

Model prediction, it is possible to search for any peak-shaped signals produced by a hypothetical new particle or, in its absence, to set limits on the mass of such a new particle.

The analysis and work done for this thesis is also part of a larger analysis, recently published by the ATLAS collaboration [1]. This thesis is organised in eleven chapters:

Theory and Motivation: This chapter describes the underlying theory by giving a short overview of the Standard Model, describing the major Standard Model contribution to the di-electron invariant mass spectrum, the neutral current Drell-Yan Process and discussing Standard Model extensions leading to the production of new neutral gauge bosons.

The Large Hadron Collider: This chapter provides an overview of the Large Hadron Collider and its operational parameters during the data taking period.

A Large Toroidal LHC ApparatuS: This chapter describes the ATLAS experiment which recorded the data for this analysis, including a description of its sub-detectors and the principles involved in reconstructing electrons from the recorded data.

Simulated Standard Model Processes: This chapter gives a description of the simulation samples used to quantify the Standard Model predictions as discrete events. This chapter also describes the work done as part of this analysis to improve the description of the neutral current Drell-Yan process by incorporating state-of-the-art theoretical knowledge into correction factors which are then applied to the simulation samples.

Simulated Signal Samples: This chapter is the counterpart to the previous chapter and describes samples quantifying the effect of new physics in a form that can be compared to the data.

Event and Electron Selection: This chapter introduces the recorded data as well as the selection criteria applied to the events in order to reject events which are not of interest. It presents an initial comparison of the data to the simulation prediction as well as a list of corrections to the simulation samples to account for detector effects.

Fake Electron Background: This chapter gives a description of a data-driven technique to quantify Standard Model contributions to the data that cannot be simulated in a viable fashion.

Data-Monte Carlo Comparisons: This chapter presents a full comparison of the observed data with the Standard Model expectation, including all known corrections and additions necessary to describe the Standard Model processes involved.

Systematic Uncertainties: This chapter briefly lists and discusses the systematic uncertainties associated with the analysis, including experimental uncertainties from the detector and experiment setup as well as uncertainties based on the modelling of the Standard Model expectation.

Statistical Test of Signal Hypotheses: This chapter describes the statistical procedure used to quantify the statistical significance of the results with respect to the Standard Model-only hypothesis and the signal hypothesis describing new physics in the form of a new heavy gauge boson, resulting in a minimum limit on the mass of a new particle.

Conclusions: This chapter summarises the work done in the thesis and places it in the larger context of particle physics.

Chapter 1

Theory and Motivation

This chapter is a discussion of the Standard Model of particle physics (1.1) and the neutral current Drell-Yan process (1.2), followed by a short discussion of extensions to the Standard Model resulting in events with topology similar to the neutral current Drell-Yan process (1.3).

1.1 Standard Model of Particle Physics

The Standard Model (SM) of particle physics is the most successful theory describing the properties and non-gravitational interactions of the fundamental particles making up all known matter at a subatomic level [2]. Developed during the mid-20^{th} century, it culminated in its current form during the 1970s [3, 4] and has been tested by a succession of increasingly powerful experiments. In the SM, the matter content is described by fermions, particles with half-integer spin, while integer spin bosons are associated with the fundamental forces.

As there is no quantum theory of gravity, only three forces are described within the SM, the strong nuclear force, the weak nuclear force and the electromagnetic force, where the latter two can be unified to form the electroweak force. The strong force is mediated by gluons (g), the weak force by the massive W and Z bosons and the electromagnetic force by photons (γ) as shown in table 1.1.

Fermions fall into two categories, quarks which participate in strong interactions and leptons that do not. All fermions have an antimatter counterpart with the same mass but opposite charge. Due to the nature of the strong force, quarks are never seen in isolation

Table 1.1: Overview of the three forces described by the SM and the associated force carrier bosons [5].

Interaction	Boson	Mass [GeV]	Charge [e]
Electromagnetic	γ	0	0
Weak	W	80.395	± 1
	Z	91.1876	0
Strong	g	0	0

Table 1.2: Overview of the three generations of fermions and their properties [5].

Type	Charge [e]	Generation		
		I	II	III
Quark	2/3	u	c	t
	-1/3	d	s	b
Lepton	-1	e	μ	τ
	0	ν_e	ν_μ	ν_τ

but only as part of compound particles, mesons (a quark-antiquark pair) and baryons (a quark triplet). Leptons exist in two varieties, charged and neutral leptons. The fermions are also divided into three generations forming three quark doublets and three lepton doublets. An overview of the particles comprising the SM is shown in table 1.2.

The fermions couple differently to the three SM interactions, quarks carry a *colour charge* and couple to the strong interaction, all fermions carrying an electric charge couple to the electromagnetic interaction and all particles couple to the weak interaction. Mathematically, the SM is a gauge quantum field theory [6, 7, 8], which can be constructed as a Lagrangian density $\mathcal{L}$. As the SM is also a relativistic theory, the Lagrangian density must be Lorentz invariant. The Lagrangian can be split into four parts:

$$\mathcal{L}_{SM} = \mathcal{L}_{Fermion} + \mathcal{L}_{Gauge} + \mathcal{L}_{Higgs} + \mathcal{L}_{Yukawa}, \tag{1.1}$$

where $\mathcal{L}_{Fermion}$ describes the kinetic energy of the fermion fields and their interaction with the gauge bosons, $\mathcal{L}_{Gauge}$ describes the kinetic terms for the gauge bosons and their self-interaction terms, $\mathcal{L}_{Higgs}$ describes the kinetic energy and self-interactions of the Higgs bosons and its interactions with the gauge bosons and $\mathcal{L}_{Yukawa}$ describes the

couplings of the Higgs to the fermions, giving rise to the fermion masses. The interactions arise from the gauge fields which are associated with gauge symmetry groups [9] as follows:

$$SU(3) \times SU(2) \times U(1), \tag{1.2}$$

where $SU(3)$ corresponds to quantum chromodynamics (QCD) and $SU(2) \times U(1)$ to the electroweak interaction resulting from the mixing of the electromagnetic and weak fields. A result of the symmetry requirement is that all interaction bosons are massless, which contradicts the experimental observation of the massive $W^{\pm}$ and Z bosons. Due to the "spontaneous symmetry breaking" of the Higgs mechanism, the $SU(2) \times U(1)$ is broken down to give rise to the $U(1)_E$ subgroup describing quantum electrodynamics (QED). In this process, the Z^0 and the $W^{\pm}$ acquire masses of $m_Z = 91.1876 \pm 0.0021\,\text{GeV}$ and $m_W = 80.385 \pm 0.015\,\text{GeV}$ respectively. This spontaneous symmetry breaking also predicts an additional boson, the Higgs boson, which was found at the LHC in 2012 [10, 11], confirming the Standard Model.

1.2 Neutral current Drell-Yan Process

In a high energy hadron collider environment, Drell-Yan (DY) pair production is one of the main processes producing lepton pairs [12], in which a quark and antiquark annihilate to form an intermediate boson, which then decays into two leptons:

$$q\bar{q} \rightarrow Z/\gamma^* \rightarrow l^+l^-. \tag{1.3}$$

The intermediate boson can either be a Z boson or a virtual off-shell photon (γ^*) as both bosons have the same quantum numbers, allowing the conservation of quantum numbers of the incoming and outgoing particles in either process. The Feynman diagram for the di-electron production through Neutral Current (NC) Drell-Yan is shown in figure 1.1.

For $2 \rightarrow 2$ scatterings like the DY process, it is customary to use the Mandelstam variables [8]. For two incoming particles with momenta p_A, p_B and two outgoing particles

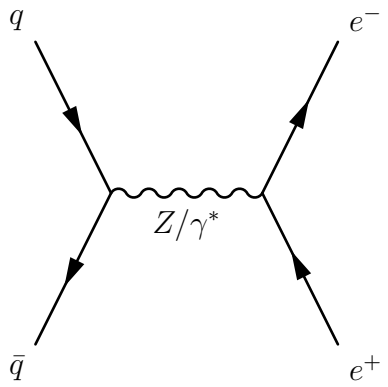

Figure 1.1: Feynman diagram for the neutral current Drell-Yan process $q\bar{q} \to Z/\gamma^* \to e^+e^-$.

with momenta k_A, k_B, they are:

$$\hat{s} \equiv (p_A + p_B)^2, \tag{1.4}$$

$$\hat{t} \equiv (p_A - k_A)^2, \tag{1.5}$$

$$\hat{u} \equiv (p_A - k_B)^2, \tag{1.6}$$

where $\hat{s}$ corresponds to the centre-of-mass energy of the incoming $q\bar{q}$ system and, at leading order, to the invariant mass m_{ee} of the outgoing e^+e^- pair.

The particles involved in the scattering are then described as:

$$q(p_A, \sigma_A) + \bar{q}(p_B, \sigma_B) \to e^-(k_A, \tau_A) + e^+(k_B, \tau_B), \tag{1.7}$$

where σ, τ describe the helicities of the incoming quarks and outgoing electrons, respectively. The cross-section for the Drell-Yan process is given as [13]:

$$\hat{\sigma}(q\bar{q} \to e^+e^-) = \frac{|\mathcal{M}|^2}{16\pi\hat{s}^2}. \tag{1.8}$$

Here the matrix element $|\mathcal{M}|^2$ for the process is the sum over the amplitudes for the allowed chirality combination states [14], giving:

$$|\mathcal{M}| = |\mathcal{A}_{LL}|^2\hat{u}^2 + |\mathcal{A}_{RR}|^2\hat{u}^2 + |\mathcal{A}_{LR}|^2\hat{t}^2 + |\mathcal{A}_{RL}|^2\hat{t}^2, \tag{1.9}$$

where the individual amplitudes are obtained by applying the Feynman rules for the electroweak Feynman diagrams comprising the process [2, 8]:

$$\mathcal{A}_{ij} = g_{EM}^2 \frac{Q_q Q_e}{\hat{s}} + g_Z^2 \frac{q_{qi} q_{ej}}{\hat{s} - M_Z^2 - iM_z\Gamma_Z}, \tag{1.10}$$

where g_{EM} and g_Z are the electromagnetic coupling constant and the coupling of the Z boson and indicate which terms in the amplitude are associated with the scattering via the γ^* and via the Z.

The cross-section $\hat{\sigma}$ alone, however, only holds for direct $q\bar{q}$ collisions. In the LHC, the collisions are between protons, which are composite particles. Following the parton model the constituents of hadrons are called "partons" [15]. Protons not only contain the uud quarks ("valence quarks"), but also virtual particles from the interactions between the valence quarks. These virtual particles are mainly gluons responsible for binding the valence quarks, but also virtual $q\bar{q}$ pairs created through the interactions inside the proton ("sea quarks"). These sea quarks contribute the necessary antiquarks for the Drell-Yan production. In a pp collision, the centre-of-mass energy $\hat{s}$ of the $q\bar{q}$ system can be defined as [16, 17, 18]:

$$\hat{s} = M^2 = x_1 x_2 s \tag{1.11}$$

where s is the centre-of-mass energy of the pp system, $x_1 and x_2$ represent the fraction of the proton's momentum carried by each parton and M is the mass of the produced resonance. Furthermore, while the pp collision is at rest in the laboratory frame, the $q\bar{q}$ system usually is not, as in most collisions $x_1 \neq x_2$, making it useful to introduce the rapidity of the system:

$$y_{cm} = \frac{1}{2} \ln \frac{x_1}{x_2} = \frac{1}{2} \ln \frac{E + p_z}{E - p_z}, \tag{1.12}$$

where E, p_z describe the energy and longitudinal momentum of the boson, as the boson is at rest in the centre-of-mass frame of the $q\bar{q}$ system, meaning $y_{cm} = y_Z$. Using equation 1.11 and 1.12, the energy fraction carried by each parton can be described as:

$$x_{1,2} = \sqrt{\frac{M^2}{s}} e^{\pm y_{cm}}. \tag{1.13}$$

The probability to find a parton carrying a momentum fraction x is then characterised by a parton distribution function (PDF) written as $F_q(x, Q^2)$, where q is the parton flavour and Q^2 the scale of the momentum transfer. In this case, the scale $Q^2 = M^2$ as the momentum transfer in the $2 \to 2$ scattering is mediated through the intermediate

boson. This leads to the overall cross-section:

$$\sigma_{pp\to e^+e^-} = \int dx_1 dx_2 \sum_q (F_q(x_1, Q^2)F_{\bar{q}}(x_2, Q^2) + F_{\bar{q}}(x_1, Q^2)F_q(x_2, Q^2))\hat{\sigma}_{q\bar{q}\to e^+e^-}, \tag{1.14}$$

which convolves the partonic cross-section $\hat{\sigma}_{q\bar{q}\to e^+e^-}$ with the PDFs for both incoming partons.

As PDFs cannot be calculated from first principles, they are parametrised at an arbitrarily chosen starting scale Q_0^2. The evolution of the PDFs is then computed using the DGLAP evolution equations [19]. The parameters at Q_0^2 are determined from experiment, mainly deep inelastic lepton-hadron scattering experiment like HERA [20], an electron-proton collider. Measurements at hadron colliders like the Tevatron or the LHC itself can also be used to improve these fits [21, 22] through jet production measurements or precision measurements of the neutral current and charged current DY process [23].

An example of the parton distribution inside the proton can be seen in figure 1.2, showing the MSTWnnlo PDF obtained by the MSTW collaboration [24] at two different momentum scales, Q^2.

The PDFs extracted from experiment are accompanied by uncertainties corresponding to the measurement uncertainties entering the global fit. As the uncertainties from measurements can be highly correlated, they cannot be propagated directly. Instead, they are described using the Hessian method, resulting in a set of i eigenvectors, each containing a pair of eigenvalues corresponding to up- and downward variations. These can be combined as follows [25, 24]:

$$\Delta f^+(S) = \sqrt{\sum_i^n [\max(f(S_i^+) - f(S_0), f(S_i^-) - f(S_0), 0)]^2}, \tag{1.15}$$

$$\Delta f^-(S) = \sqrt{\sum_i^n [\max(f(S_0) - f(S_i^+), f(S_0) - f(S_i^-), 0)]^2}, \tag{1.16}$$

where $f(S)$ is a function depending on the PDF, S_0 corresponds to the central value of the PDF set and $S_i^\pm$ to the up- and downward variation of the i^{th} PDF eigenvector.

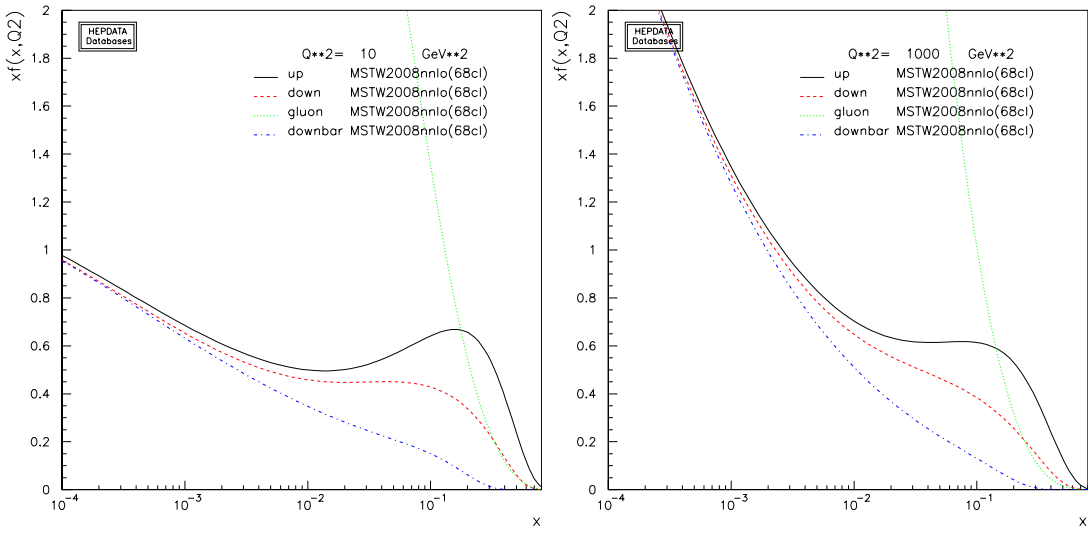

Figure 1.2: Proton PDFs at NNLO from the MSTW collaboration, plotted at the momentum transfer scales $Q^2 = 10\,\mathrm{GeV}^2$ and $Q^2 = 1000\,\mathrm{GeV}^2$. Plots generated using [26].

1.3 Production of New Gauge Bosons

Despite the overwhelming success of the SM, it is a limited theory and not all predictions match the observations made in nature. Examples are the observed matter/antimatter asymmetry [27, 28], the existence of neutrino masses implied by neutrino oscillations [29, 30, 31] or the astrophysical observations of a cosmological constant [32]. Even more puzzling is the "hierarchy problem": Gravity is exceedingly weak, meaning its influence on particle interactions would occur at the Planck scale at around $10^{19}\,\mathrm{GeV}$ whereas the EW scale is at the order of $100\,\mathrm{GeV}$.

This large difference in energy scales has two consequences, "fine-tuning" and a "particle desert". Radiative corrections cause the effective Higgs boson mass to diverge, meaning it naturally tends towards the Planck scale. In order to explain the observed Higgs mass close to the EW scale, large radiative terms have to cancel almost perfectly, which is seen as excessive fine-tuning of the model. Additionally, if the SM is fully valid up to the Planck scale before it breaks down due to the effects of quantum gravity, it means there is a large parameter space between the EW and Planck scale where "nothing happens", in contrast to the comparatively small difference in scales for the strong, weak and electromagnetic interactions.

A solution to both problems is the existence of new physics at the TeV scale as it would introduce a cut-off scale for the SM and populate the region between the EW and Planck scale. One way to introduce new physics is to postulate an additional gauge

Table 1.3: Overview of Z'_{SSM} limits set by previous analyses, showing the limits in the electron channel or multi-channel combinations. A dash indicates that no information can be found.

	Observed Limit	
Experiment	e^+e^- [TeV]	l^+l^- [TeV]
LEP (2009) [41]	—	1.79
CDF (2009) [42]	0.96	—
D∅ (2010) [43]	1.02	—
CMS (2010) [44]	0.96	1.14
CMS (2011) [45]	2.12	2.33

symmetry group $U(1)'$, extending the SM symmetries to [33, 34]:

$$SU(3)_C \times SU(2)_L \times U(1)_Y \times U(1)'. \tag{1.17}$$

As a result, additional W′ and Z' bosons would arise from the extra symmetry group analogous to the W and Z bosons of the Standard model. As a benchmark model for searches, the Sequential Standard Model (SSM) is chosen [34], which sets the couplings of the Z' from the new $U(1)'$ to the existing fermions to the same coupling as for the Z boson with the only difference being the mass of the Z'_{SSM}. While this model has no strong theoretical motivation, it is a useful benchmark model to compare the reach and sensitivity of a search between different experiments. Additionally, it forms a narrow resonance peak in a mass spectrum and searches for resonance peaks have proven to be powerful tools, as resonance searches in the past have led to the discovery of the J/Ψ [35, 36], the Υ [37] and the Z [38, 39].

Previous searches for new bosons at LEP have established indirect limits on the boson mass [40, 41], and direct limits at the Tevatron and the LHC itself, as shown in table 1.3. Limits set by the ATLAS collaboration are not shown here but can be found in section 10.4, table 10.1.

Chapter 2

The Large Hadron Collider

The LHC is a circular proton-proton synchrotron collider located in a 26.7 km circumference underground tunnel at the European Organisation for Nuclear Research (CERN). CERN and the LHC are located in Geneva, Switzerland and cross the French-Swiss border, as shown in figure 2.1 [46]. The LHC is designed to accelerate protons to an energy of up to 7 TeV producing collisions with a centre-of-mass energy of $\sqrt{s} = 14\,\text{TeV}$ at the four interaction points (IP). In addition, the LHC can also accelerate lead ions, with a design energy of 2.8 TeV per nucleon. The LHC not only provides unprecedented centre-of-mass energy, but is also designed to provide a high rate of collisions, with an instantaneous luminosity of up to $10^{34}\,\text{cm}^{-2}\text{s}^{-1}$. Together, the high energy and the high rate of collisions allow the study of previously unreachable kinematic regions and rare processes.

Each interaction point is the location of one of the four main LHC experiments: ALICE (A Large Ion Collider Experiment) [47], ATLAS (A Toroidal LHC Apparatus) [48], CMS (Compact Muon Solenoid) [49] and LHCb [50]. ALICE is an experiment dedicated to the study of heavy ion physics, using the LHC's capability to produce lead-lead and lead-proton collisions to study strongly interacting systems and the quark-gluon plasma. For the remainder of this chapter (and thesis) the focus will be on pp collisions. ATLAS and CMS are two General Purpose Detectors (GPDs) providing 4π solid angle coverage and are able to test the SM of particle physics and probe various beyond the Standard Model theories. LHCb is a single-arm spectrometer with tracking sensors close to the interaction point for high-precision vertex reconstruction necessary for heavy flavour physics at high pseudorapidity, η (see section 3.1).

The LHC synchrotron is located between 50 m–175 m underground and consists of two beam pipes integrated into a single structure, as shown in the dipole magnet schematic in

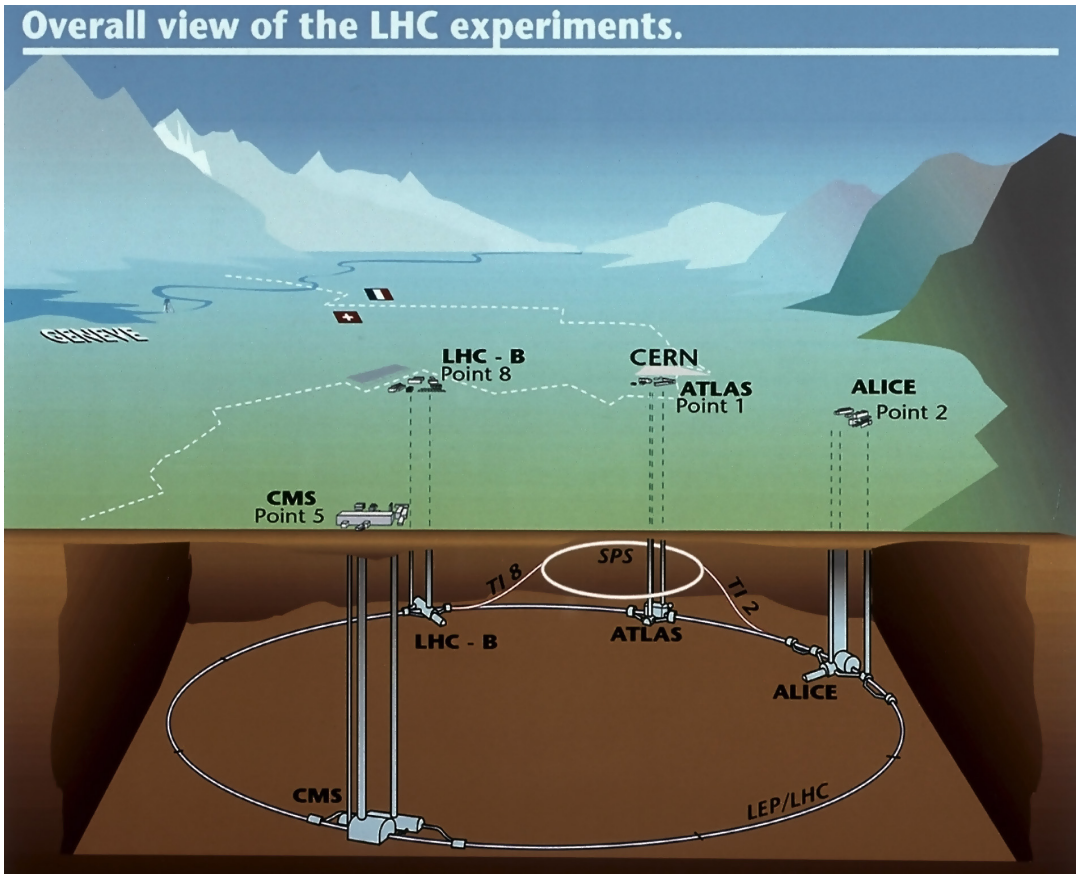

Figure 2.1: Overall view of the LHC tunnel and the four main experiments in relation to Geneva and the Franco-Swiss border [51].

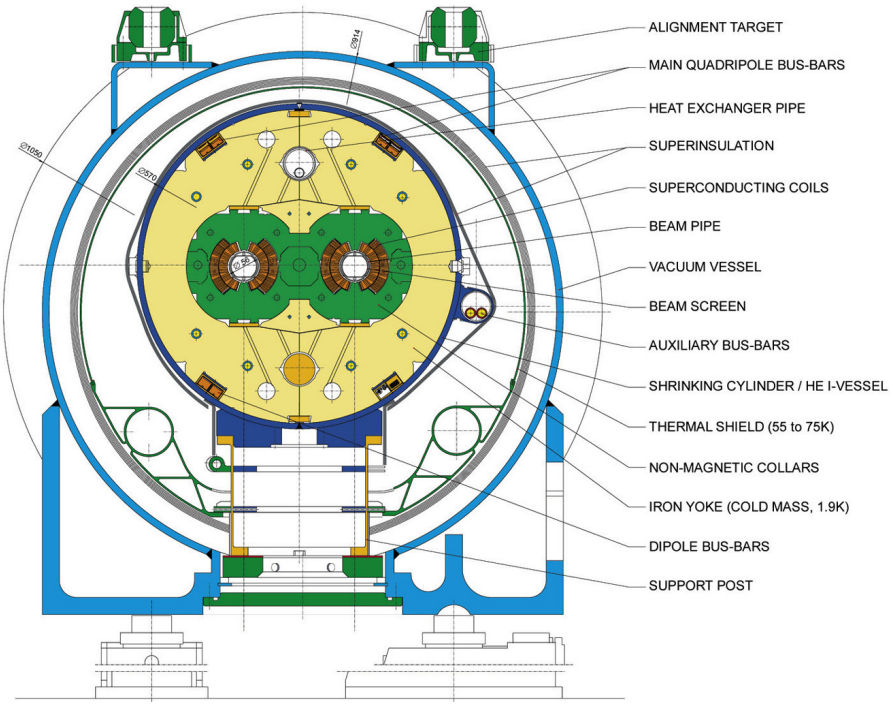

Figure 2.2: Cross-section of a LHC dipole magnet, showing the two beam apertures and surrounding dipole magnets and services. Schematic adapted from [52]

figure 2.2. This dipole design allows the simultaneous control of two beams with a single accelerator ring by using the return field of one ring as field for the other ring. The beam is accelerated using 16 radio-frequency cavities (RF cavities), which accelerate particles using an alternating electric field tuned to the frequency of the beam. The beam is bent using 1232 superconducting Nb-Ti dipole magnets kept at 1.9 K using liquid helium, while quadrupole and sextupole magnets of the same type are used to focus the beam in the plane orthogonal to the beam axis.

The LHC accelerator chain (see figure 2.3) begins with protons accelerated to an energy of 50 MeV in the Linac2 linear accelerator. From there on, the protons are accelerated further in three stages in three different circular accelerators: to an energy of 1.4 GeV in the Proton Synchrotron Booster, to 25 GeV in the Proton Synchrotron (PS) and to 450 GeV in the Super Proton Synchrotron (SPS). Once the protons reach 450 GeV, they are injected into the LHC. The LHC accelerates the protons further in two beams travelling in opposite directions, until each beam reaches an energy of 7 TeV per proton. The protons are injected into the LHC in bunches, with 2808 bunches per beam and 1.15×10^{11} particles per bunch. Collisions occur at the interaction points where the two beams cross, allowing two bunches to meet and collide. The LHC is designed to achieve a bunch spacing of 25 ns, corresponding to a bunch crossing rate of 40 MHz. A single run

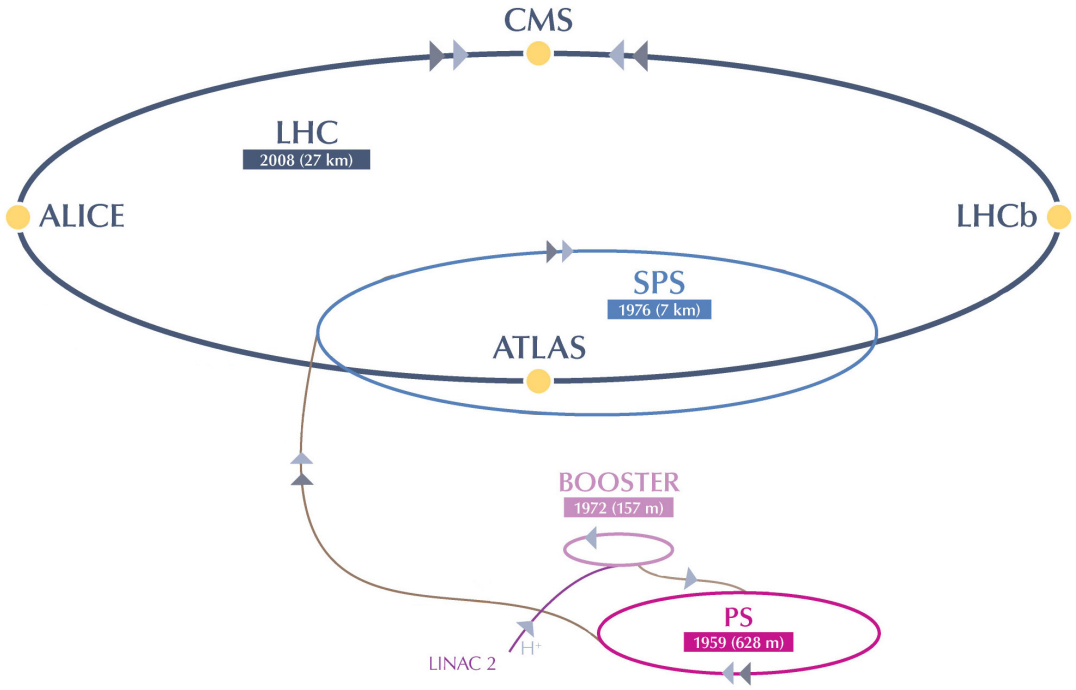

Figure 2.3: LHC accelerator chain, showing the accelerators used to produce and inject the proton beam for the LHC. Schematic adapted from [53].

with a beam is usually called a "beam fill" or "fill". Fills last until the luminosity of the beam has reduced to an undesirably low level or until a technical reason requires removal of the beam from the ring. In either case, the beam is "dumped" into the beam dump absorbers, water-cooled carbon cylinders 7700 mm in length and 700 mm in diameter, embedded in about 900 tons of radiation shielding blocks.

In order to quantify the number of interactions, the concept of luminosity is used. The instantaneous luminosity $\mathcal{L}$ is given in units of $\mathrm{cm}^{-2}\mathrm{s}^{-1}$ and determines the expected number of events for a process with the cross-section σ. Integrated over time, this gives the integrated luminosity L, usually given in units of inverse barn ($1\,\mathrm{b} = 10^{-24}\,\mathrm{cm}^{-2}$), hence the total number of events is calculated as:

$$N = \sigma L = \sigma \int \mathcal{L} dt \tag{2.1}$$

The 2012 run of the LHC lasted from April to December 2012, yielding a total integrated luminosity of approximately $23\,\mathrm{fb}^{-1}$ [54]. This run was not only longer than the 2011 run, but also pushed the run parameters closer to the design specifications as shown in table 2.1 and even exceeding them in the number of protons per bunch. Beam energy calibration studies yielded a beam energy of $3988 \pm 26\,\mathrm{GeV}$ for the 2012 run [55].

Table 2.1: Comparison of LHC design and run parameters during the 2012 run, adapted from [54].

Parameter	Design Value	2012 Value
Beam Energy [TeV]	7.0	4.0
Bunch Spacing [ns]	25	50
Number of Bunches	2808	1374
Protons per Bunch	1.15×10^{11}	1.7×10^{11}–1.8×10^{11}
Peak Luminosity [$\mathrm{cm}^{-2}\mathrm{s}^{-1}$]	1×10^{34}	7.7×10^{33}

Chapter 3

A Large Toroidal LHC ApparatuS

The LHC provides high energy collisions of protons, producing a large number of particles that allow insight into the physics driving interactions at these energy scales. To study these interactions, it is necessary to reliably observe, identify and measure the particles produced in the collisions. This chapter gives an overview of the ATLAS experimental apparatus (3.1), the sub-systems comprising the detector (3.2, 3.3, 3.4), the trigger and luminosity systems necessary to record events and understand the event rates (3.5, 3.6) and describes the reconstruction process for electrons (3.7) and finishes with a short discussion of the data taking in 2012 (3.8).

3.1 Goals and Overview of ATLAS

The ATLAS detector is a general purpose detector built to record high-energy collisions at the LHC. The unprecedented centre-of-mass energies and luminosities at the LHC not only allow studies of the SM but also of physics beyond the Standard Model. In order to facilitate such studies and searches, ATLAS was designed [56] to have an excellent electromagnetic calorimeter for electron and photon identification and hermetic calorimetry with large polar acceptance and total azimuthal coverage for jet and missing E_T measurements. Additionally, the tracking provides precise lepton momentum measurements and vertex identification at high luminosity, while allowing triggers with a low momentum threshold.

The coordinate system used in ATLAS uses the interaction point in its centre as origin. The z-axis is defined by the beam direction with the x-y plane orthogonal to the z-axis. The x-y plane is also referred to as the transverse plane. The positive x-direction

points towards the the centre of the LHC ring and the positive y-direction points directly upwards. Since the interaction point serves as the origin, the polar angle of an particle created at the interaction point can be described in terms of the pseudorapidity η, defined as

$$\eta = -\ln \tan \theta/2 = \frac{1}{2} \ln \frac{|\mathbf{p}| + p_z}{|\mathbf{p}| - p_z} \tag{3.1}$$

For massless particles ($m \ll E$, i.e. $|\mathbf{p}| \approx E$), pseudorapidity η is a good approximation for the rapidity y as defined in equation 1.12.

As Lorentz boosts only add a constant to the rapidity y of a particle, Δy and $\Delta \eta$ are invariant for Lorentz boosts along the z-axis. Using a polar coordinate system, R is the distance from the z-axis, ϕ describes the azimuthal angle around the z-axis while θ is the polar angle from the z-axis. Hence it is possible to describe the radial separation ΔR of particles in $\eta - \phi$ space as

$$\Delta R = \sqrt{\Delta\eta^2 + \Delta\phi^2}. \tag{3.2}$$

The transverse components of variables (e.g. transverse momentum p_T, transverse energy E_T) are defined in the x-y plane.

In its entirety, the ATLAS detector is approximately barrel-shaped, about 25 m in diameter and 44 m in length with the interaction point located in the centre of the detector as shown in figure 3.1. ATLAS consists of several sub-detector systems: the Inner Detector (ID) [57] in the centre, the Electromagnetic CALorimeter (ECAL) [58] surrounding the inner detector, followed by the Hadronic Calorimeters (HCAL) [59] and the Muon Spectrometers [60] defining the outside dimensions of ATLAS. In addition, the solenoid magnet system surrounds the inner detector and the toroid magnets are located outside the calorimeters.

3.2 The Inner Detector

The inner detector surrounds the beam pipe at the interaction point and consists of three detector systems: the Pixel Detector, the SemiConductor Tracker (SCT) [62] and the Transition Radiation Tracker (TRT) [63]. All three are used to detect the tracks of charged particles in a pseudorapidity range of $|\eta| < 2.5$, allowing the reconstruction

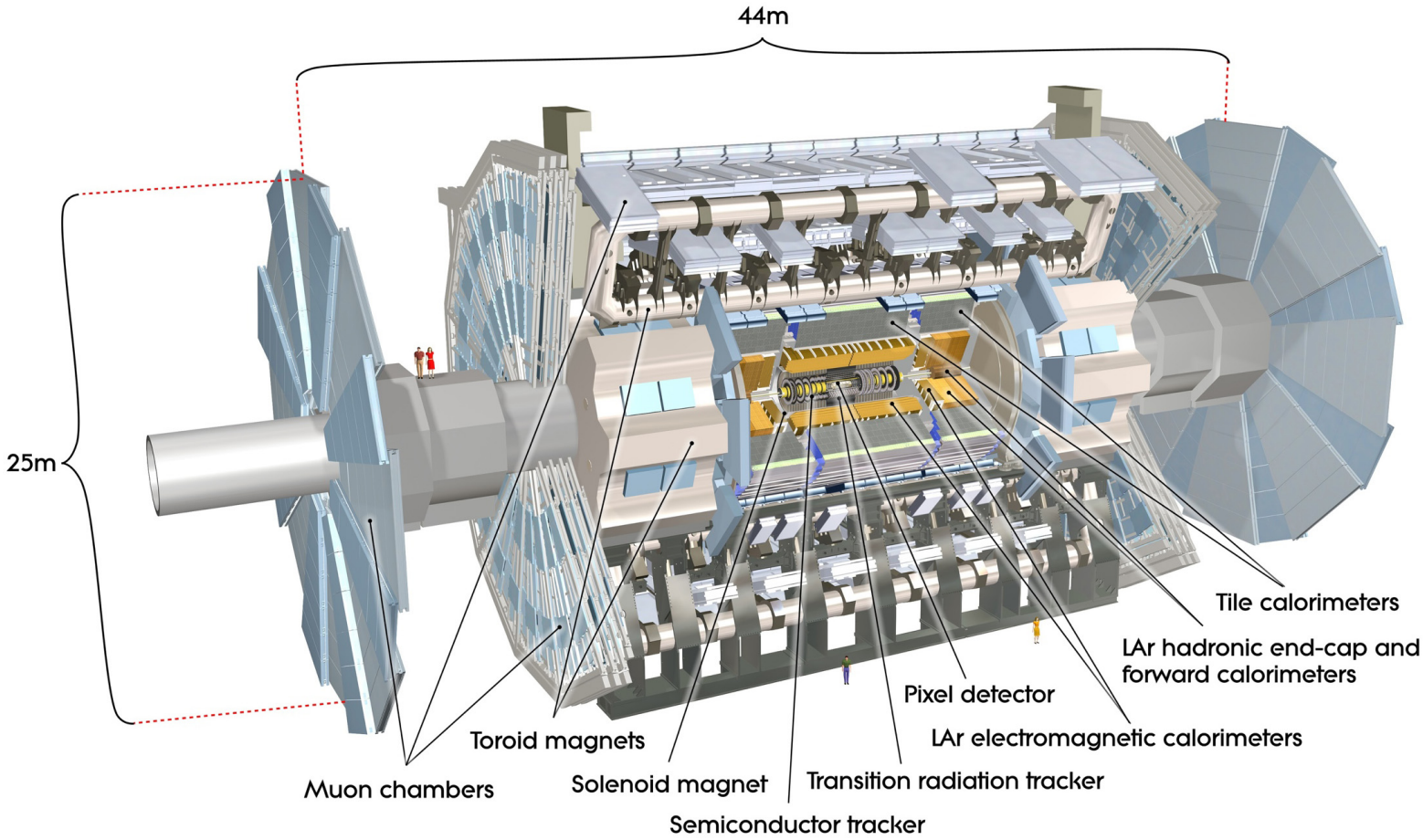

Figure 3.1: Cutaway view of ATLAS, showing the individual sub-detectors as well as the magnet system and the overall size of the detector [61].

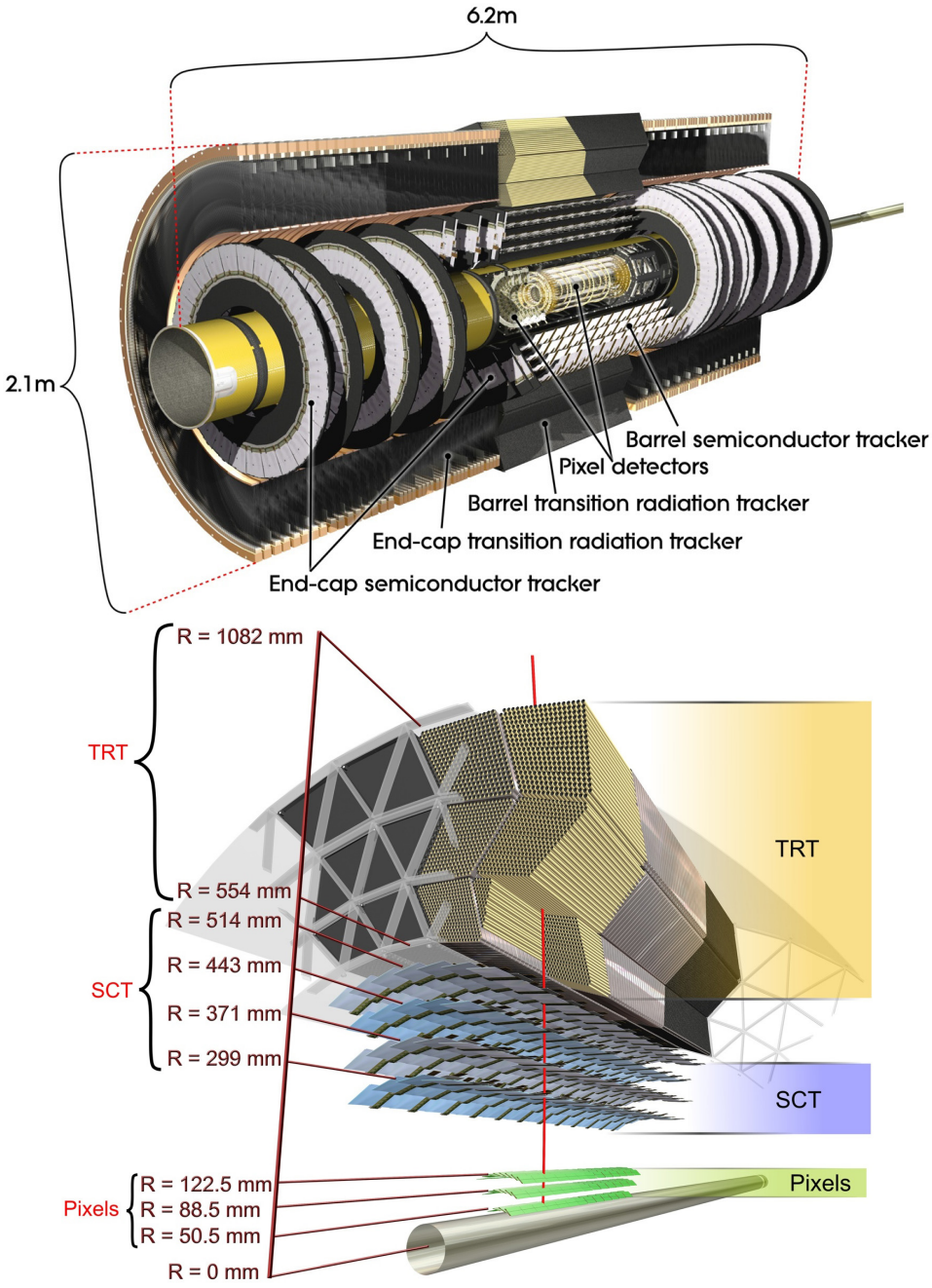

Figure 3.2: *Top:* Cutaway view of the ATLAS Inner Detector, showing the Pixel detector, the SCT and the TRT. *Bottom:* Layers of the Pixel detector, SCT and TRT and their distance from the beamline [64].

of their origin and momentum determination via the curvature of their paths in the solenoidal magnetic field. The arrangement of the tracking detectors is illustrated in figure 3.2.

The innermost sub-detector is the Pixel detector, consisting of 1744 individual sensor modules arranged around the interaction point in three barrel layers parallel to the beam axis with a radius of $R = 50.5\,\text{mm}$, $88.5\,\text{mm}$ and $122.5\,\text{mm}$. The innermost layer is called the *b-layer*. Both ends of the barrel structure are capped by five wheel-shaped end-caps perpendicular to the beam axis. Each individual barrel sensor module is $63.4\,\text{mm} \times 24.4\,\text{mm}$ in size and features 47232 individual pixels, each measuring $50\,\mu\text{m} \times 400\,\mu\text{m}$. Due to the segmentation into individual layers, each track typically crosses three layers with a position resolution of $10\,\mu\text{m}$ in $R - \phi$ and $115\,\mu\text{m}$ in z. The pixels are silicon-based detectors, using *pn*-junctions with an applied bias voltage to detect ionisation caused by charged particles passing through them [65]. This technology also provides the radiation hardness necessary to withstand the radiation damage caused by the proximity to the beam. Nevertheless, the b-layer will require replacement after about three years.

The SCT envelops the Pixel detector, consisting of a barrel and end caps, much like the Pixel detector itself. The four barrel SCT layers span are located at $R = 299\,\text{mm}$, $371\,\text{mm}$, $443\,\text{mm}$ and $514\,\text{mm}$ and consist of 2112 SCT modules in total. The end-caps consist of 9 wheel-shaped layers on each end of the barrel, totalling 1976 individual modules. The SCT modules are based on the same silicon technology as the Pixel detector, but instead of pixels, they are arranged in two layers of strips with a strip pitch of $80\,\mu\text{m}$ and a stereo angle of $40\,\text{mrad}$. Particles traversing a SCT module are detected in both strip layers, allowing the z-position determination thanks to the stereo angle between the two strips. The SCT provides a position resolution of $17\,\mu\text{m}$ in $R - \phi$ and $580\,\mu\text{m}$ in z in the barrel region and a resolution of $580\,\mu\text{m}$ in $R - \phi$ and $17\,\mu\text{m}$ in z in the end-cap region.

The TRT makes up the outermost part of the inner detector, occupying the region between the radii of 554 and $1082\,\text{mm}$. The TRT uses polyamide tubes of $4\,\text{mm}$ diameter as drift tubes (or "straws"), filled with a Xenon-based gas mixture, with a gold-plated tungsten wire in the centre acting as anode. The straw tubes are interleaved with polypropylene-polyethylene fibres as transition radiation material. The TRT consists of a barrel region, covering $|\eta| < 1.0$, with $144\,\text{cm}$ long straws parallel to the z-axis, and an end-cap region of 37 cm long radial straws, covering $1.0 < |\eta| < 2.0$. As ultra-relativistic particles traverse the TRT, crossing the material, they produce transition radiation. The transition radiation photons then ionise the gas mixture, enhancing the signal from straw hits. The TRT only provides a measurement in $R - \phi$ (in the barrel) with a resolution of 130 μm, but since approximately 36 hits are expected per track, this measurement is

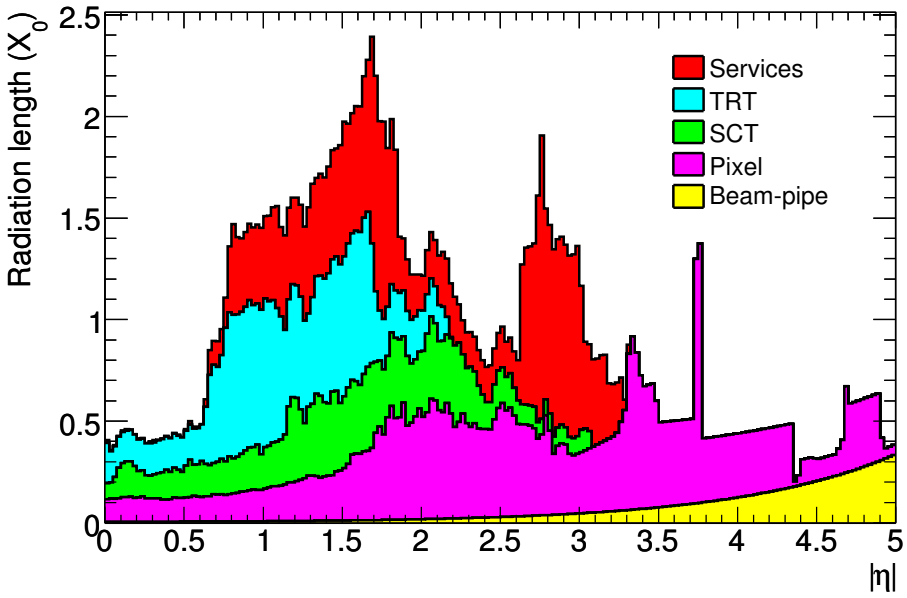

Figure 3.3: Material distribution in terms of radiation length X_0 as a function of $|\eta|$ in the inner detector [48].

used to improve the momentum accuracy of the overall track measurement together with the pixel detector and the SCT.

The inner detector is surrounded by the solenoid magnet, which provides an axial magnetic field of 2 T. As charged particles travel through the field, they are affected by the Lorentz force, causing them to bend in the transverse plane. By measuring the curvature of the track, it is possible to determine the momentum of charged particles.

3.3 Calorimetry

The calorimeter is split into two main systems, the Electro-magnetic CALorimeter (ECAL) and the Hadronic CALorimeter (HCAL), used to measure electro-magnetically interacting and strongly interacting particles respectively. As implied by the name, the calorimeters are used to measure the total energy of the particles, requiring the containment of the particle and the shower it produces within the calorimeter. As a result, the material in the calorimeter is often described in terms of *radiation lengths* X_0 (the mean distance over which high energy electrons lose $1/e$ of their energy, which is relevant to the ECAL) and *interaction lengths* λ (mean distance over which the number of relativistic particles is reduced by $1/e$, which is important for hadrons and hence relevant to the HCAL).

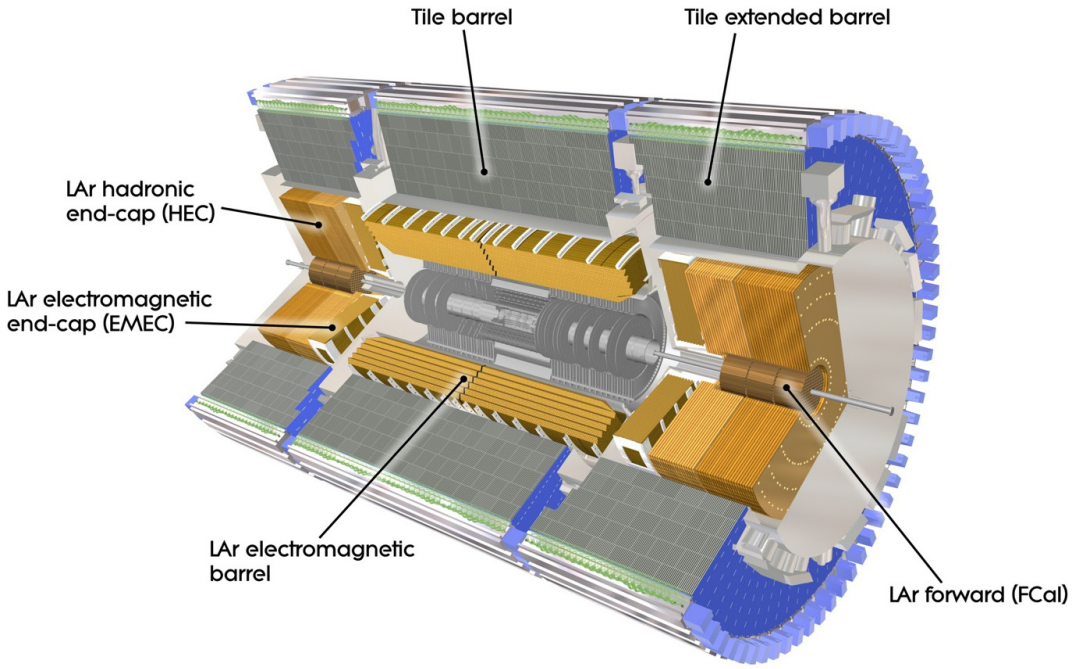

Figure 3.4: Cutaway view of the ATLAS calorimetry surrounding the inner detector (greyed out in the centre), showing the individual calorimeters [66].

The calorimeters surround the inner detector, as shown in figure 3.4. The material in inner detector is mapped in radiation lengths X_0, shown in figure 3.3. This determines the expected energy loss of electromagnetically interacting particles before reaching the ECAL.

The ECAL measures the energy of photons and electrons entering it and also performs the measurement of the energy of the electro-magnetic component of jets. The ECAL consists of two barrels with a 4 mm gap between them at z = 0 m, covering a range of $|\eta| < 1.475$, and an end-cap at each end of the barrel. Each end-cap consists of two wheels, an inner and an outer wheel, which cover a range of $1.375 < |\eta| < 2.5$ and $2.5 < |\eta| < 3.2$, respectively. The ECAL consists of accordion-shaped lead layers as energy absorber and liquid argon (LAr) as active detection medium, filling the space between the lead layers, with individual cells segmented in $\eta - \phi$. The structure is split into three layers, a thin initial layer for high position precision thanks to its extremely high granularity (less than 0.025 in $\Delta\eta$ for the majority of the covered η range), a second layer to contain the majority of the shower and a third layer to estimate the shower leakage out of the ECAL into the HCAL, as illustrated in figure 3.5. Additionally, in the range $|\eta| < 1.8$, another layer is placed in front of the first layer, the so-called pre-sampler, which is used to estimate the energy losses of photons and electrons before they reach

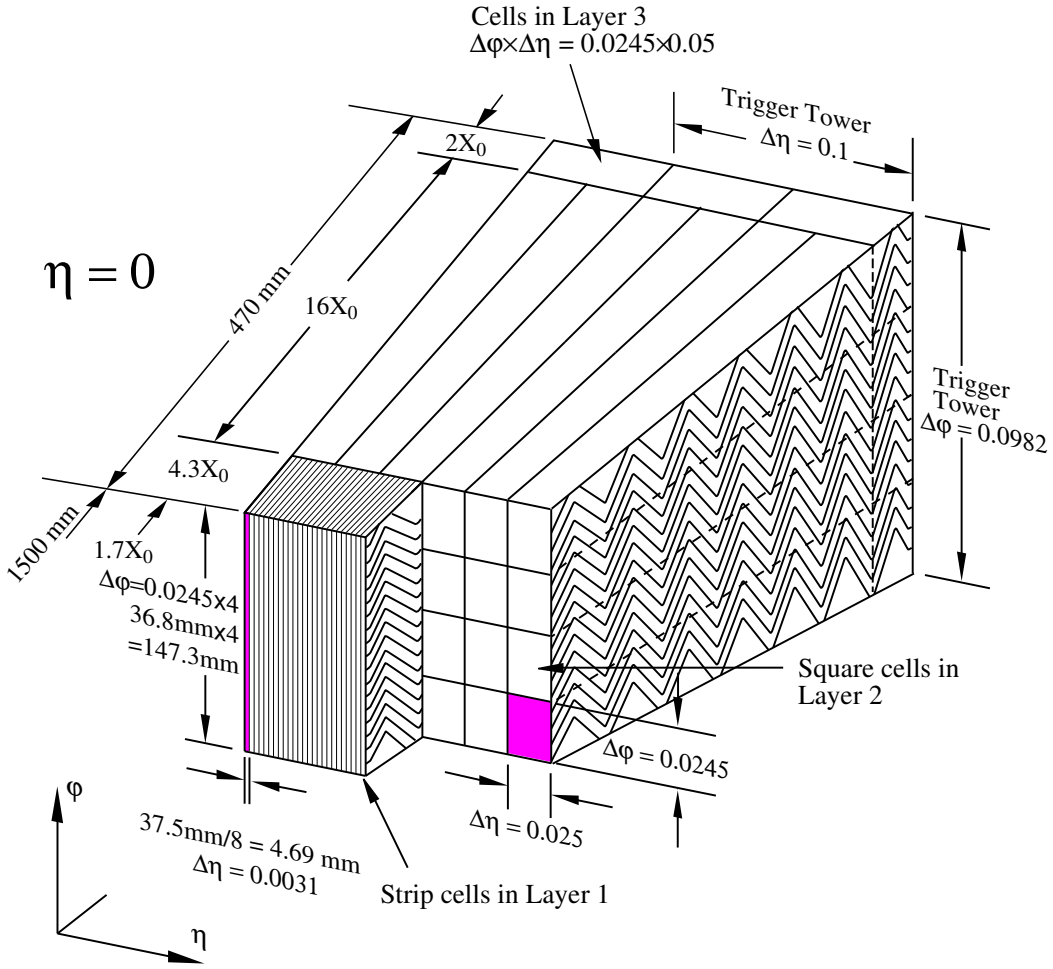

Figure 3.5: Schematic of an ECAL barrel segment, showing the cell segmentation and the three layers.

the calorimeter. In total, the ECAL has 9344 individual pre-sampler readout channels (7808 in the barrel and 768 in each end-cap) and 163968 readout channels for the three main layers (101760 in the barrel, 31104 in each end-cap). The high granularity of the ECAL allows for high precision in locating energy deposits and allows for shape-based discrimination between leptons, photons and jets. In order to contain the liquid argon, the ECAL is housed in three cryostat vessels, one for the barrel and one for each end-cap.

The hadronic calorimeter is used to measure the energy of the strongly interacting component of jets and to absorb all particles (apart from muons) that passed through the ECAL in order to perform a measurement of the total energy of an event. The hadronic calorimetry is split into a barrel region (HCAL) and the hadronic end-caps (HEC). The barrel region consists of a central barrel and an extended barrel on each end, covering a range of $|\eta| < 1.0$ and $0.8 < |\eta| < 1.7$, respectively. The three barrels together are also

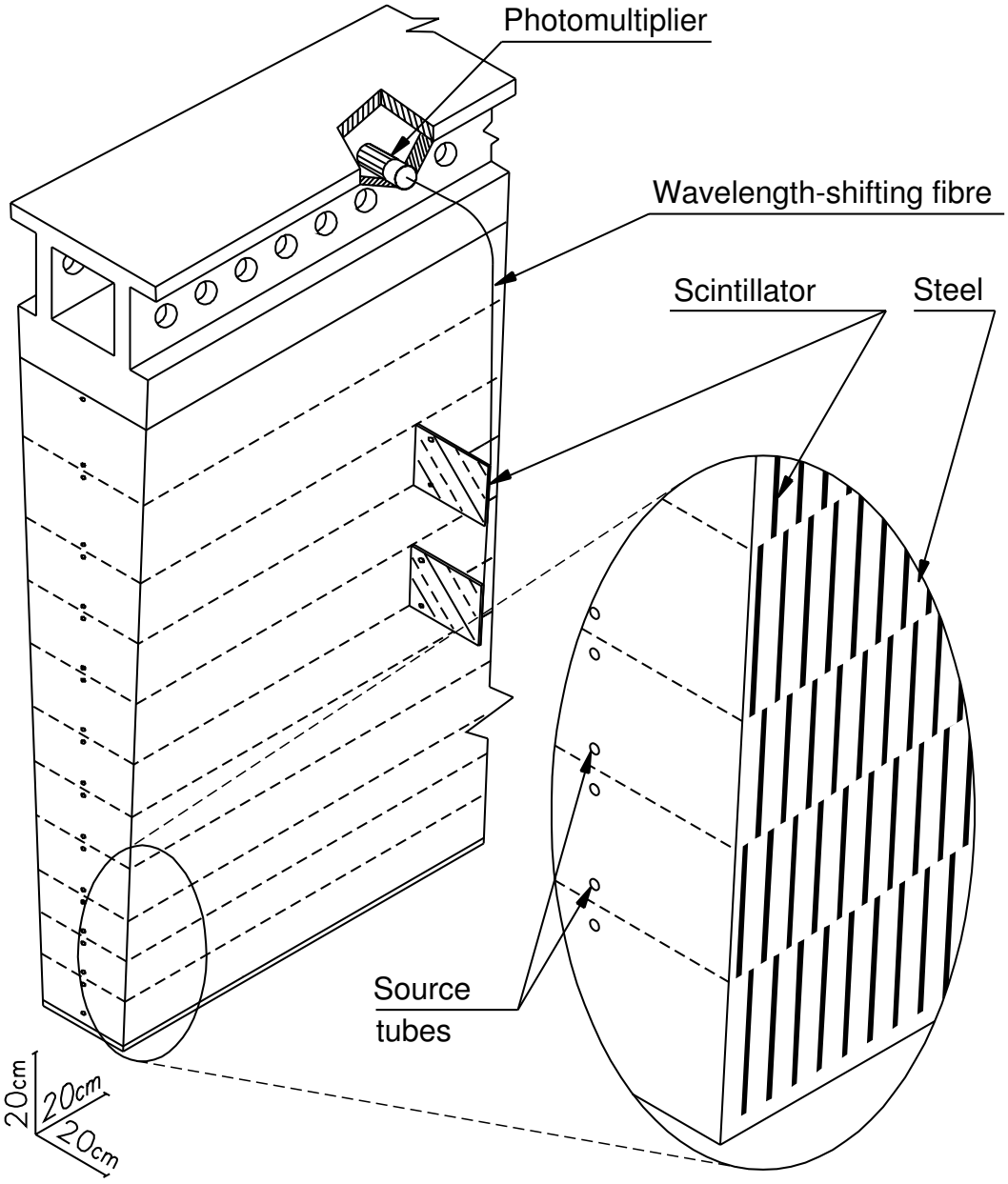

Figure 3.6: Schematic of a HCAL tile, showing the interleaved scintillator-steel structure.

called the tile calorimeter, as they use scintillating tiles as detection medium and steel as energy absorber, as shown in figure 3.6. This allows the absorber to act as the return yoke for the magnetic field of the inner detector solenoid.

The hadronic end-cap uses liquid argon as active detector medium, similar to the ECAL, but uses copper as energy absorber instead of steel. The hadronic end-cap consists of two wheels at each end, located directly after the end-caps of the ECAL and shares the cryostat with the ECAL end-caps.

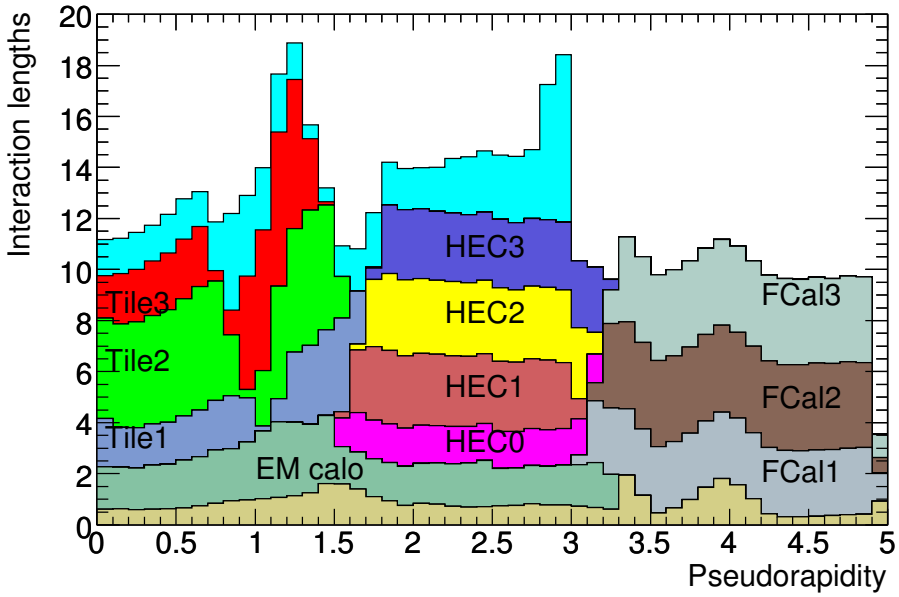

Figure 3.7: Material distribution in λ as function of $|\eta|$ in the calorimeter [48].

Contained within the same cryostat are the forward calorimeters (FCAL). One FCAL is located at each end of the overall calorimeter, nestled inside the ECAL end-caps and the HEC, close to the beam pipe, providing a coverage of $3.1 < |\eta| < 4.9$. Each FCAL is further segmented into three modules. All modules use liquid argon as detection medium, but vary in the choice of energy absorber. The first module, closer to the interaction point, uses tungsten as absorber and is optimised for electromagnetic energy deposition, while the other two modules use copper and are optimised for hadronic energy measurements.

As shown in figure 3.7, the calorimeter provides at least nine interaction lengths or more of material in an η range of up to 4.9, ensuring that the majority of all hadronic energy measurements record the full energy of the particles.

3.4 Muon Spectrometer

The largest sub-detector, defining the overall dimensions of ATLAS, is the muon spectrometer (MS), shown in figure 3.8. The MS surrounds the calorimeter and detects muon tracks, as muons are capable of traversing the entire detector, leaving tracks in the MS. The muon system also encompasses the three superconducting air-core toroid magnets: one barrel toroid, consisting of eight coils, and two end-cap toroids. The barrel toroid

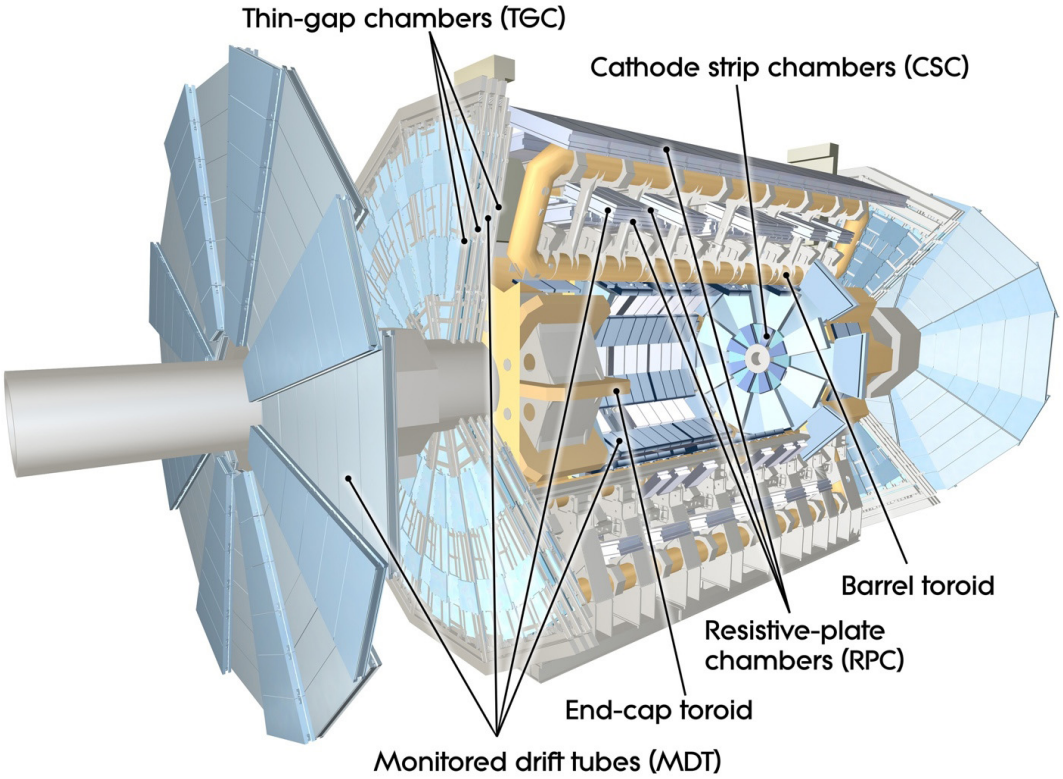

Figure 3.8: Overview of the ATLAS muon spectrometer [67].

provides a 0.5 T field in the range $|\eta| < 1.0$ and the end-cap toroids provide a field of 1 T in the range $1.4 < |\eta| < 2.7$. In the transition region from $1.0 < |\eta| < 1.4$, where both magnets provide deflection. This configuration of magnetic fields is orthogonal to most muon trajectories, providing magnetic deflection for momentum determination.

The muon chambers making up the MS are arranged in three layers ("stations") around the interaction point. The MS contains 1150 monitored drift tubes (MDTs) with 32 Cathode Strip Chambers (CSCs) supplementing them at the inner end-cap station for the high η-range of $2.0 < |\eta| < 2.7$ [68]. The CSCs have a higher granularity and are more suited to the high rates in that region. The MDTs have a position resolution of 35 µm in z and the CSCs have a position resolution of 40 µm in R and 5 mm in ϕ, making them the precision chambers of the MS.

In addition to the high-precision MDTs and CSCs, trigger chambers are spread throughout the MS. In the barrel, Resistive Plate Chambers (RPCs) are used, while the end-caps use Thin Gap Chambers (TGCs). These trigger chambers are optimised for fast response instead of resolution and are used for the trigger system (see below) and also for the ϕ measurement in the barrel region. The RPCs provide a position resolution of

10 mm in z and 10 mm in ϕ, while the TGCs provide a position resolution of 2 mm–6 mm in R and 3 m–7 m in ϕ.

3.5 Luminosity Monitoring

ATLAS uses special sub-detectors to measure the LHC luminosity delivered to the experiment [69]. These detectors are the the LUminosity measurement using Cherenkov Integrating Detector (LUCID), Beam Condition Monitor (BCM) [70] and the Absolute Luminosity For Atlas (ALFA) [71]. In addition, the tile calorimeter and the FCAL are used to supplement the luminosity determination by measuring overall detector currents which are proportional to the particle flux [72].

LUCID is the main system and consists of two detectors close to the beam pipe, located at $z = \pm 17$ m. Each detector consist of 20 aluminium tubes arranged around the beam pipe. Each pipe is 1.5 m in length and 15 mm in diameter, filled with C_4F_{10} gas. As these tubes are hit by particles from p-p inelastic scatterings, the particles emit Cherenkov light, which is registered by photomultiplier tubes. This gives a measure of the particles traversing LUCID, allowing a luminosity measurement for each bunch crossing.

The BCM is used to monitor the general beam conditions in particular to detect unstable beams and abort operations before the detector can be damaged. In addition, the BCM is used to obtain luminosity information, complementary to the measurements from LUCID. The BCM consists of two stations, placed at $z = \pm 1.84$ m from the interaction point. Due to the radiation hardness needed close to the interaction point, the BCM uses diamond sensors, operating in a manner similar to the silicon sensors of the inner detector, but using chemical vapour deposited diamond instead of silicon.

Since these measurements are simply interaction rates, the luminosity is calibrated using *van der Meer* scans [72, 73]. During these scans, the colliding beams are slowly swept across each other in x and y independently, allowing the determination of the effective area of the beams. Using the effective area of the beam in conjunction with the known beam parameters (number of bunches, particles per bunch, frequency of bunch crossings), it is possible to determine the absolute luminosity.

Since each proton bunch consists of a number of protons, multiple interactions can occur during a single bunch crossing. This is called “pile-up”. As part of the luminosity

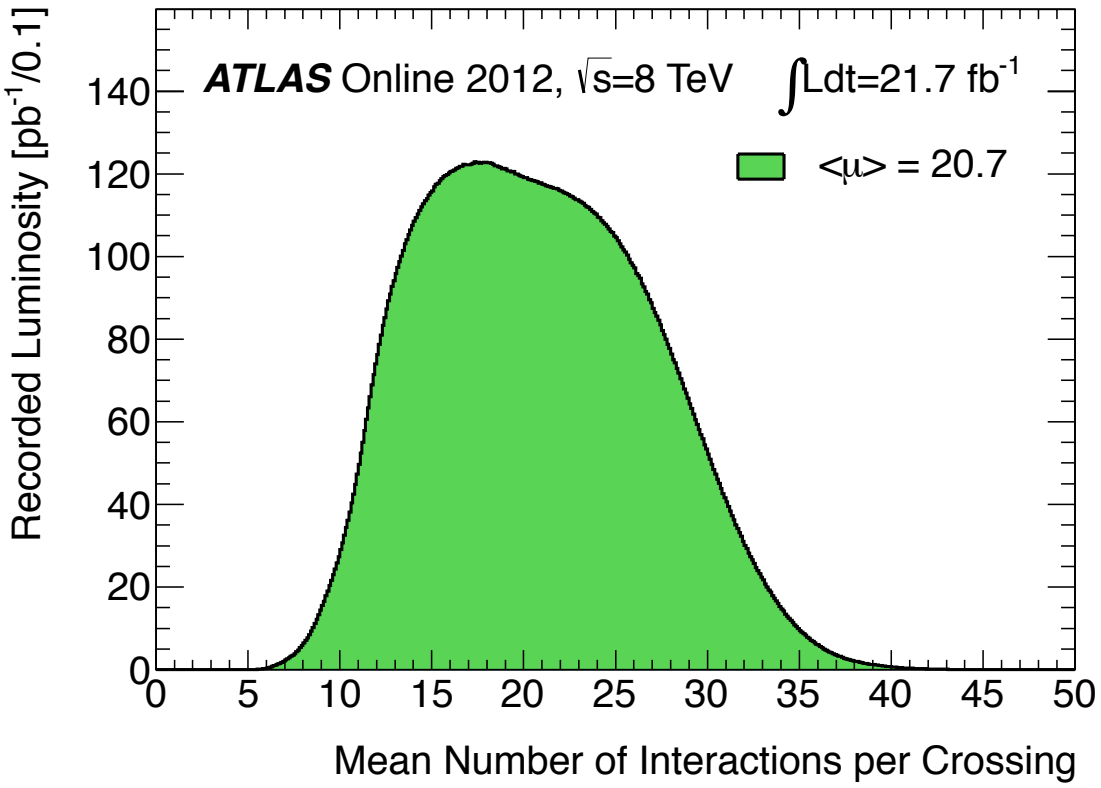

Figure 3.9: Average number of interactions $\langle\mu\rangle$ in the 2012 data taking, from [75].

monitoring, the average number of interactions in a bunch crossing is determined as well as shown in figure 3.9 [74]. More detail on pile-up can be found in section 6.4.

3.6 Trigger Systems

The LHC produces collisions ever 25 ns or at a rate of 40 MHz (50 ns and 20 MHz during the 2012 run), which produces a data rate too large to be recorded in its entirety. In order to make it feasible to gather data, the trigger system decides which events are of interest and which events can be discarded. This system runs in three stages: the Level 1 (L1) trigger implemented in the form of dedicated hardware; the Level 2 (L2) trigger; and the Event Filter (EF), which are software-based and are called High Level Triggers (HLT) [76, 77].

Due to bandwidth and buffer size constraints, the L1 trigger only uses information from the calorimetry and the trigger muon chambers. The system triggers on combinations of sufficiently localised high energy deposits in the calorimeters, as these are associated

with physics objects of interest (electron, photons, taus and jets), sufficiently high total transverse energy E_T, large missing transverse energy $E_T^{miss}$and/or muon tracks. This step reduces the total rate of recorded events to approximately 75 kHz [78].

The L2 trigger is a software trigger running on dedicated computers using data collected after the L1 trigger. With the lower rate, it is now possible to use more detector information from all detectors at full granularity and the inclusion of tracking data allows distinction between photons and electrons. This step reduces the effective event rate down to about 3.5 kHz.

Finally, the EF trigger is applied to all events passing the L2 trigger. With the further increased time to process events, the EF can not only access the full detector data, but also uses event reconstruction algorithms similar to those used offline, allowing greater discrimination between physics signatures of interest and background This step brings down the rate of events to about 200 Hz, which it is feasible to record. The events are separated in several categories, so called "streams", depending on the physics objects involved in triggering (example streams are the electron stream, the jet stream or the missing E_T stream).

3.7 Electron Reconstruction and Identification

Electrons are reconstructed based on information recorded by the detectors, mainly the tracking systems of the ID and electromagnetic calorimetry provided by the ECAL. Track fits and energy deposits are used to determine the 4-vector of electrons by combining energy measurements with track-derived direction and momentum measurements.

The inner detector track reconstruction uses the recorded data together with the information about the detector design to transform individual hits into spatial information and then fits tracks [78, 79]. The track reconstruction is done in three stages:

1. Pixel and SCT data are converted into individual space points while the TRT timing information is used to construct drift circles.

2. Track finding algorithms are applied to build tracks. The algorithms use information from the three pixel layers as well as the first SCT layer to form track seeds. The track seeds are extended through the rest of the SCT using hits in the remaining SCT layers to form track candidates. The track candidates are then fitted and quality

requirements are applied to reject fake tracks. The tracks passing the requirements are then extended into the TRT, using the drift circles to resolve ambiguities in the track curvature. Once the track is built, it is refitted using the position information from all three detectors together.

3. Tracks are used to reconstruct the primary vertices by extrapolating them back to the interaction point. Further algorithms are used to find photon conversions and secondary vertices.

The electron-specific reconstruction itself begins with the calorimeter data. The precision region ($\eta < 2.5$) of the calorimeter is divided into an η-ϕ grid with 200 divisions in η and 256 divisions in ϕ. Each sector measures $\Delta\eta \times \Delta\phi = 0.025 \times 0.025$, corresponding to the ECAL cells in the second layer, as shown in figure 3.5. First, the calorimeter is scanned for cluster seeds using a sliding window algorithm [80]: a 5×5 sector window runs over the η-ϕ grid until it finds an energy deposit with a transverse energy $E_T < 2.5\,\text{GeV}$. Once such a cluster seed is found, track matching is performed, searching for reconstructed tracks that, when extrapolated to the calorimeter, impact near the cluster within $|\Delta\eta| < 0.1$ and $|\Delta\phi| < 0.1$ with the track bend and $|\Delta\phi| < 0.05$ away from the track bend. This asymmetric requirement accounts for radiative losses due to Bremsstrahlung. If no track match is possible, the cluster is discarded. In the case of multiple track matches, tracks with pixel or SCT hits are preferred, using the closest track with pixel or SCT hits. After the track match, the cluster is rebuilt using a 3×7 or a 5×5 window in the barrel or end cap, respectively.

The overall reconstruction efficiency is measured by the ATLAS electron performance group using the tag-and-probe method. In this method, $Z \to ee$ decays are used to test the efficiency by using one electron with a high quality identification (see below) to "tag" an event as $Z \to ee$. The second electron can then be used as a "probe" by comparing the number of "tag" events to the number of "probe" events. The result can be seen in figure 3.10, demonstrating an efficiency of over 95% for the whole E_T range as well as the minor difference between the reconstruction efficiency found in data and established from simulation.

Once the clusters are built, electron identification follows, using track and shower shape variables, as detailed in [79, 82]. The electron identification allows rejection of hadronic jets containing pions, kaons or protons as these leave tracks and produce a cluster as well as electrons stemming from photon conversions. The three identification levels are called *loose*, *medium* and *tight*, with each step adding additional criteria and

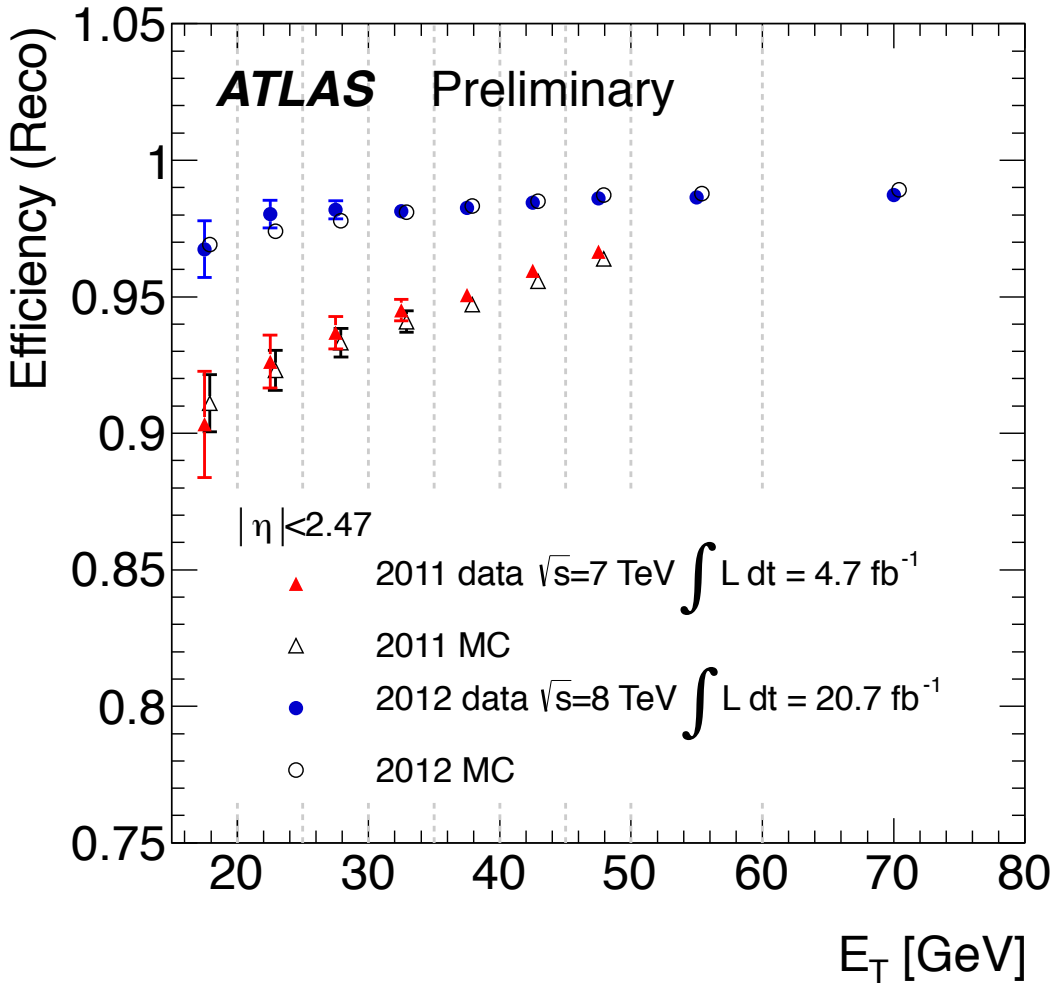

Figure 3.10: Efficiency of the electron-specific reconstruction for data and simulations for electrons as function of electron E_T measured using the $Z \to ee$ tag-and-probe method. Plot from [81].

making existing criteria more stringent. The full list of categories and variables used for the identification for central electrons can be seen in table 3.1. The exact requirements are optimised in 10 η-bins and E_T-bins from 5 GeV to 80 GeV.

The *loose* identification is based on the shower shape within the calorimeter. Two variables introduced to characterise the cluster are the shower width in the first layer ω_{stot} and the lateral shower width $\omega_{\eta,2}$, defined as follows:

$$\omega_{stot} = \sqrt{\frac{\sum_i E_i (i - i_{max})^2}{\sum_i E_i}}, \tag{3.3}$$

where i is the strip index in the first layer and i_{max} the index of the strip with the maximal energy deposition of the cluster:

$$\omega_{\eta,2} = \sqrt{\frac{\sum_i E_i \eta_i^2}{\sum_i E_i} - (\frac{\sum_i E_i \eta_i}{\sum_i E_i})^2}, \tag{3.4}$$

where i is the cell index in the middle layer of the calorimetry. $\omega_{\eta,2}$ describes the width of the shower in the middle layer, while ω_{stot} describes the total shower width, using the front layer of the ECAL, allowing the quantification of different shower shapes. Furthermore, the *loose* criterion involves the ratio of energy in the ECAL to the energy deposition in the hadronic calorimetry; this is called "hadronic leakage" and is helpful in identifying hadrons as they deposit more energy in the hadronic calorimetry. Finally, the *loose* requirement requires a minimum amount of hits in the pixel and silicon detectors as measure of the track quality.

The *medium* identification uses the same requirements as the *loose* identification, but imposes more stringent requirements for the already defined criteria. Additionally, it requires hits from the innermost layer of the pixel detector in order to reject conversion electrons from photons - the inner layer hit means the particle leaving the hit is charged before it interacted with the material of the detector. Furthermore, the transverse impact parameter d_0 is introduced, measuring the minimum distance in the transverse plane between the extrapolated electron track and the primary vertex. To improve rejection of charged hadrons, a requirement on transition radiation in the TRT is imposed as well.

The *tight* identification again takes the *medium* requirements and makes them more strict. In order to ensure that the track and cluster originate from the same object, the measured momentum from the track and the deposited energy are compared using the ratio E/p. Furthermore, the match between the cluster and track is tightened, the

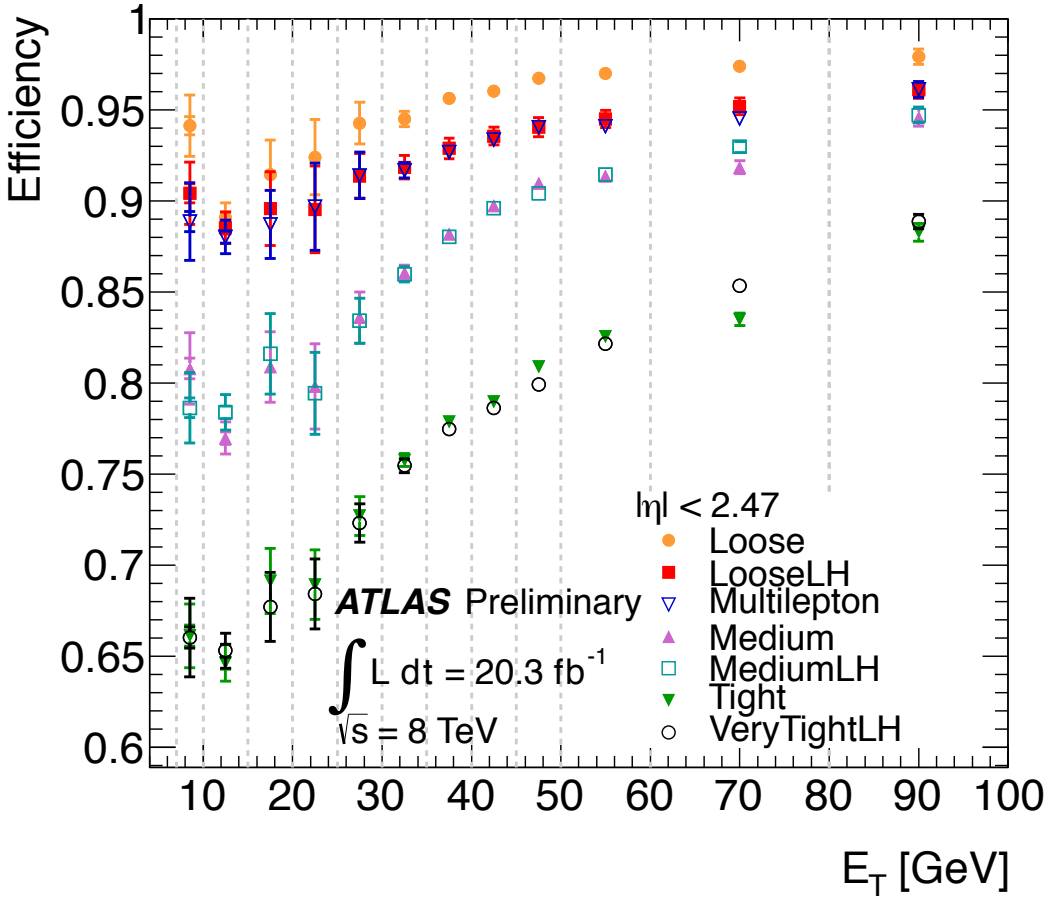

Figure 3.11: Identification Efficiency for *loose*, *medium* and *tight* electron depending on E_T measured using the $Z \to ee$ tag-and-probe method. Plot from [81].

transverse impact parameter cut is more stringent, a minimum number of TRT hits is required and electrons matching reconstructed photon conversions are rejected.

Similarly to the reconstruction, the identification efficiency is measured using the tag-and-probe method using $Z \to ee$ events. As can be seen in figure 3.11, the efficiency drops with more stringent identification requirements but uniformly rises with E_T. Furthermore, the *medium* identification efficiency rises well above 90% for electrons with $E_T > 50\,\text{GeV}$.

3.8 Data Taking in 2012

During the 2012 run, the LHC delivered $22.8\,\text{fb}^{-1}$ of $\sqrt{s} = 8\,\text{TeV}$ pp collisions in the period from the 4$^{\text{th}}$ of April to the 6$^{\text{th}}$ of December. In this period, ATLAS recorded

Table 3.1: List and explanation of the variables used in the *loose*, *medium* and *tight* electron identification criteria in the central region of the detector ($|\eta| < 2.47$), adapted from [82].

Category	Description	Variable
	loose	
Acceptance	$\|\eta\| < 2.47$	
Hadronic leakage	In $\|\eta\| < 0.8$ and $\|\eta\| > 1.37$: ratio of E_T in the first layer of the hadronic calorimeter to E_T of the EM cluster	$R_{\text{had},1}$
	In $0.8 < \|\eta\| < 1.37$: ratio of E_T in whole hadronic calorimeter to E_T of the EM cluster	R_{had}
Middle layer of the EM	Ratio of energies in 3×7 cells over 7×7 cells	R_η
	Lateral width of the shower	$w_{\eta 2}$
Front layer of the EM	Total shower width	w_{stot}
	Energy difference of the largest and second largest energy deposits in the cluster divided by their sum	E_{ratio}
Track quality and track–cluster matching	Number of hits in the pixel detector (> 0)	
	Number of hits in the silicon detectors (≥ 7)	
	$\|\Delta\eta\|$ between the cluster position in the first layer and the extrapolated track (< 0.015)	$\Delta\eta_1$
	medium **(includes *loose* with tighter requirements on shower shapes)**	
Track quality and track–cluster matching	Number of hits in the b-layer > 0 for $\|\eta\| < 2.01$	
	Number of hits in the pixel detector > 1 for $\|\eta\| > 2.01$	
	Transverse impact parameter $\|d_0\| < 5$ mm	d_0
	Tighter $\|\Delta\eta_1\|$ cut (< 0.005)	
TRT	Loose cut on TRT high-threshold fraction	
	tight **(includes *medium*)**	
Track quality and track–cluster matching	Tighter transverse impact parameter cut ($\|d_0\| < 1$ mm)	
	Asymmetric cut on $\Delta\phi$ between the cluster position in the middle layer and the extrapolated track	$\Delta\phi$
	Ratio of the cluster energy to the track momentum	E/p
TRT	Total number of hits in the TRT	
	Tighter cut on the TRT high-threshold fraction	
Conversions	Reject electron candidates matched to reconstructed photon conversions	

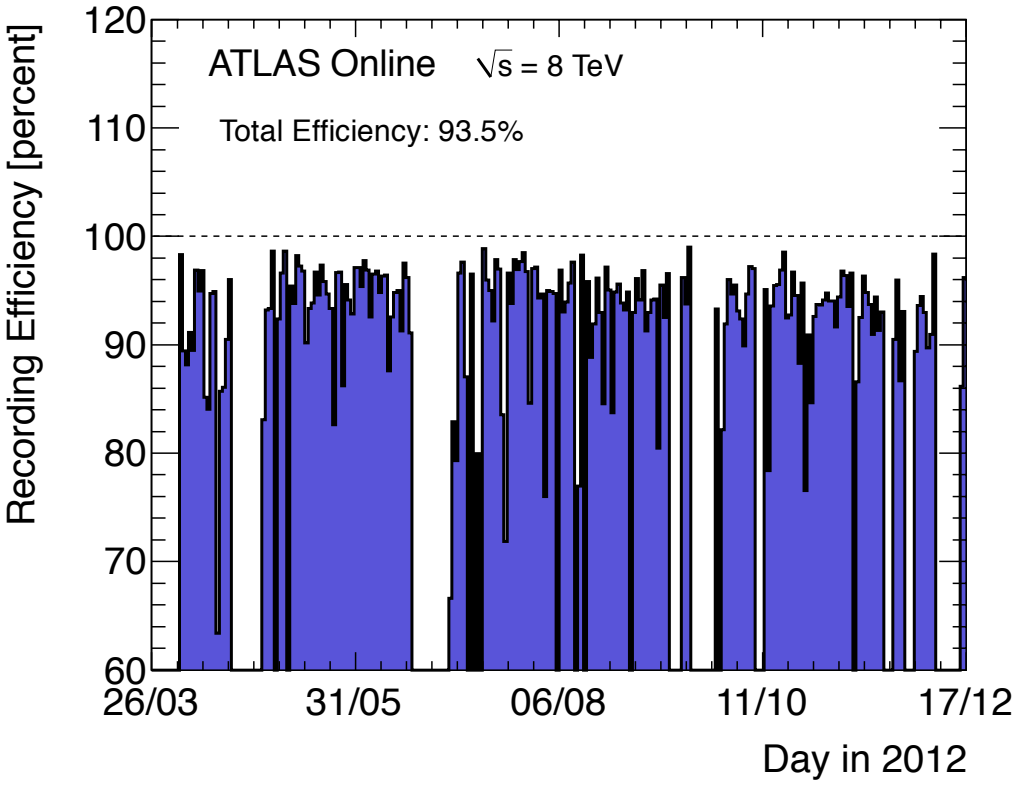

Figure 3.12: ATLAS data taking efficiency over time, comparing LHC reported luminosity to ATLAS recorded luminosity [75].

$21.3\,\text{fb}^{-1}$ of data with a preliminary uncertainty of 2.8%[1]. By comparing the luminosity recorded by ATLAS to the luminosity delivered by the LHC, the overall efficiency of ATLAS is determined to be 93.5%. The efficiency over time is shown in figure 3.12. The 2012 run is divided into individual periods with the same running conditions, labelled period A to L in alphabetical order[2]. During each period, there are individual data taking runs, which usually encompass an entire LHC beam fill (see chapter 2), and have unique identification numbers. The runs are further divided into 60 s long luminosity blocks of approximately constant instantaneous luminosity and beam conditions. Each luminosity block is flagged either as useful or not for physics analysis in a Good Run List (GRL).

During online data recording, the data quality (DQ) is measured by automated systems registering the status of the detector as well as by "shifters" (shift personnel) comparing performance plots to reference plots. After data recording, offline monitoring is performed by automated checks and shifter comparisons of detector parameters and reference plots. The DQ information is then used to produce the GRLs indicating which luminosity blocks of data are good for physics analysis. This process resulted in $20.3\,\text{fb}^{-1}$ of data that is good for all physics analyses, as shown in figure 3.13.

In addition, the data were also reprocessed after the 2012 data taking finished. This reprocessing implemented improvements in the calibration and remonstration obtained after the end of the run. Additionally, during reprocessing, the requirements of the individual physics streams are checked with the defects in the DQ information, allowing the use of select streams that are unaffected by particular defects irrelevant to the physics stream in question.

[1] Luminosity measurement as described in [72], updated for the 2012 run
[2] Periods F and K did not involve data taking for physics analyses

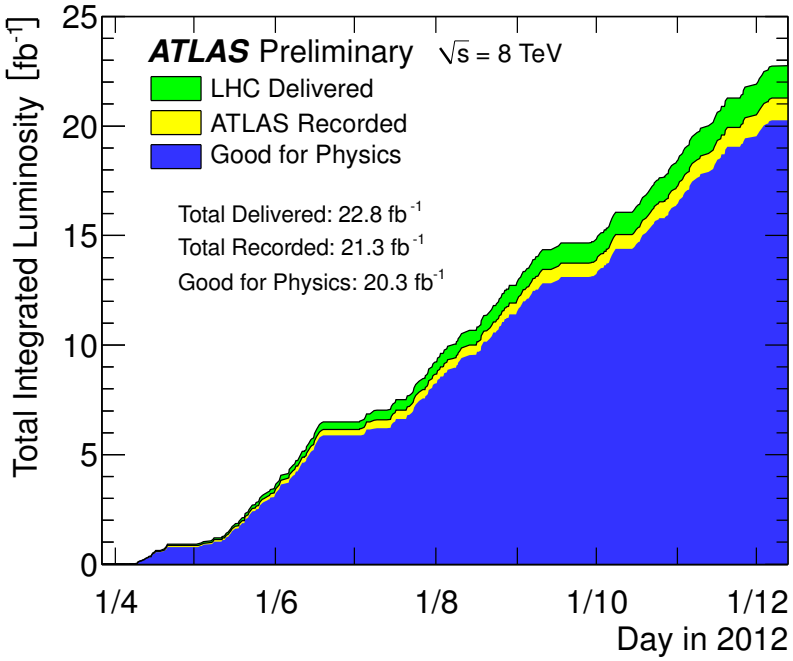

Figure 3.13: ATLAS integrated luminosity in 2012 [75].

Chapter 4

Simulated Standard Model Processes

An essential tool in modern particle physics are physics simulations of known SM processes as well as simulations of new physics. As the simulations produce samples with individual events, it becomes viable to compare theory directly to data in the form of histograms. This chapter provides an overview of Monte Carlo simulations (4.1) and the simulation samples used to describe SM processes (4.2, 4.3, 4.4).

4.1 ATLAS Monte Carlo Simulation

SM events are simulated in order to compare the current SM theory with the experimental data. The simulation can be divided into two main steps, event generation and detector simulation. During event generation, physics processes are simulated on an event-by-event basis, integrating over the allowed phase space by random number sampling. This integration method is known as Monte Carlo integration, hence the simulation is usually referred to as Monte Carlo.

As described in chapter 1, the protons colliding in the LHC are composite particles. In a proton-proton collision typical for this analysis, one parton from each incoming proton interacts in the main hard process of interest while the rest of the partons undergo softer interactions and are described as beam remnants. The overall picture is sketched in figure 4.1 and roughly follows the following process [83]: The flavour and energy of the incoming partons contained in the beam are characterised by PDFs. These incoming partons are shown as three parallel incoming lines from the left and the right in figure 4.1. Both beams have one parton as shower initiator, building up an initial state shower for each beam as shown in blue in figure 4.1. Both showers contribute one parton entering

the hard process which is calculated using the matrix element up to a specific order in α_S and α, usually Leading Order (LO) or Next-to-Leading Order (NLO), shown as the large solid red circle in figure 4.1. This hard process determines the nature of the event and may form an intermediate particle, such as the Z boson in the neutral current Drell-Yan process. The next step is the parton showering of any outgoing partons, tracking the progression of coloured partons and gluons, shown in red, followed by the hadronisation where the subsequent formation of colour-neutral states is simulated, shown in figure 4.1 in red. The simulation of the underlying event follows the evolution of the proton remnants, usually partons with much lower energy than the particles involved in the hard process, shown in purple in figure 4.1. Finally, the decay of short-lived particles is simulated, resulting in a record of all final state particles that can reach the detector, indicated in green in figure 4.1.

At this stage, it is possible to apply an event filter. An event filter discards events not fulfilling the requirements for final state particles, e.g. the production of certain particles. This enriches the sample with events of interest and can be used to reduce disk space requirements and computing time. The ratio of kept events to total events is called the filter efficiency $\epsilon_{filter} = N_{MC}/N_{total}$, where N_{MC} is the number of kept events and N_{total} the number of events generated in total. This modifies the integrated luminosity (equation 2.1) for a Monte Carlo sample to:[1]

$$L_{MC} = \frac{N_{MC}}{\sigma_{total}} = \frac{N_{MC}}{\sigma_{process} \times \epsilon_{Filter}}. \tag{4.1}$$

The final state particles are then tracked further in the detector simulation, using GEANT4 [85]. The GEANT4 program simulates the interaction of the final state particles with the detector material. This includes the interaction with the active detector material in order to simulate the detector response. Based on the simulated detector response, the digitisation produces data similar to the read-out of the real detector during data taking, allowing comparison of Monte Carlo samples with data samples. A few samples do not undergo the full detector simulation and use a fast simulation instead, where the effects of the GEANT4 simulation are approximated. These samples are called fast simulation or ATLFAST-II samples.

As Monte Carlo is modelling the physics processes before and after the full detector response (plus event selection, see chapter 6), it is useful to define $A \times \epsilon_{eff}$ here, the

[1] In the case of some NLO samples, such as the MC@NLO samples, events can have negative weights representing as higher order processes can interfere with lower order processes. In this case, the number of events N_{MC} is the sum of all individual event weights.

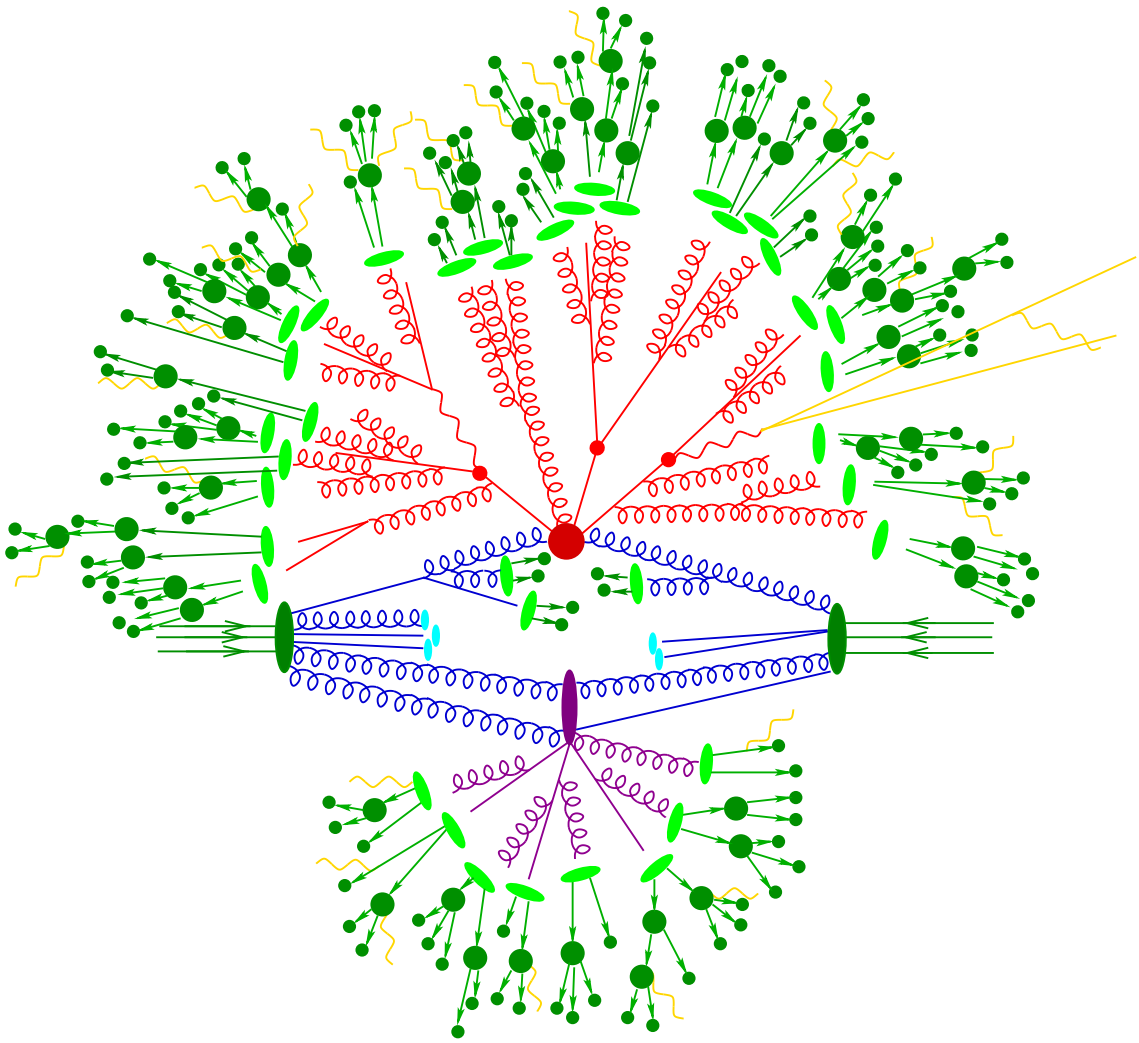

Figure 4.1: Sketch of a high-energy proton-proton collision, showing the incoming partons (green incoming lines), the initial parton shower (blue lines), the hard process (dark red), the parton showering (red), the beam remnants (cyan) and their interactions forming the underlying event (purple) and the subsequent decay products (dark green outgoing lines). The sketch shows a fully hadronic process with initial and final states mainly consisting of strongly interacting particles. Adapted from [84].

acceptance times efficiency. The acceptance A describes the fraction of particles within the fiducial range of the detector, while the efficiency ϵ_{eff} incorporates all detector-related efficiency effects. This quantity is defined as:

$$A \times \epsilon_{eff} = \frac{N_{pass}}{N_{MC}}, \tag{4.2}$$

where N_{pass} is the number of events passing the full detector simulation (plus event selection as described in chapter 6) and N_{MC} the number of filtered generated events from equation 4.1. In total, the number of reconstructed and selected events from a Monte Carlo sample can then be described as:

$$N_{pass} = A \times \epsilon_{eff} \times N_{MC} = A \times \epsilon_{eff} \times \sigma_{process} \epsilon_{filter} L_{MC} \tag{4.3}$$

4.2 Simulation of Drell-Yan Di-electron Production

The main SM contribution to the di-electron mass spectrum at high mass is the neutral current Drell-Yan production of electron pairs ($pp \to Z/\gamma^* \to e^+e^-$) as described in chapter 1. The event generation is done by the POWHEG [86] Monte Carlo generator using the CT10 PDF [87]. POWHEG is interfaced with PYTHIA8 [88] and PHOTOS 3.0 [89]. POWHEG is used for the hard scattering part of the event generation while PYTHIA8 handles the parton shower, hadronisation and particle decays and PHOTOS simulates the effects of the QED Final State Radiation (FSR).

Due to the exponentially falling production cross-section over the mass range considered here, the region of interest (66 GeV–5000 GeV) is divided into 16 mass bins for the event generation. Each bin covers a separate region of generated Z/γ^*masses as shown in table 4.1. This division into individual mass bins allows sufficient statistical precision to be obtained over the entire mass range. In order to avoid overlap from the open-ended $M_Z \geq 60$ GeV sample, events with Z/γ^*s with a generated masses of $M_Z \geq 120$ GeV are removed during the event selection. All samples are then scaled to the same luminosity and are added together.

The Drell-Yan Monte Carlo samples are generated at NLO for QCD and with a LO implementation of weak interaction effects. Current state-of-the-art theory calculations

Table 4.1: List of Drell-Yan Monte Carlo samples, including details on the generation range, the MC run identifier, the cross-section and the total number of generated events and associated Monte Carlo luminosity.

m_{ee}[GeV]	MC Run	$\sigma\times$ Br [pb]	N_{gen} $[1 \times 10^3]$	L_{MC} [fb^{-1}]
60+	147806	1.1098×10^{3}	10000	8.968×10^{0}
120 - 180	129504	9.846×10^{0}	500	5.058×10^{1}
180 - 250	129505	1.571×10^{0}	100	6.328×10^{1}
250 - 400	129506	5.492×10^{-1}	100	1.810×10^{2}
400 - 600	129507	8.966×10^{-2}	100	1.110×10^{3}
600 - 800	129508	1.510×10^{-2}	100	6.621×10^{3}
800 - 1000	129509	3.750×10^{-3}	100	2.653×10^{4}
1000 - 1250	129510	1.293×10^{-3}	100	7.706×10^{4}
1250 - 1500	129511	3.577×10^{-4}	100	2.777×10^{5}
1500 - 1750	129512	1.123×10^{-4}	100	8.872×10^{5}
1750 - 2000	129513	3.838×10^{-5}	100	2.598×10^{6}
2000 - 2250	129514	1.389×10^{-5}	100	7.179×10^{6}
2250 - 2500	129515	5.226×10^{-6}	100	1.904×10^{7}
2500 - 2750	129516	2.017×10^{-5}	100	4.930×10^{7}
2750 - 3000	129517	7.891×10^{-6}	100	1.262×10^{8}
3000+	129518	5.039×10^{-5}	100	1.974×10^{8}

allow for theory predictions at NNLO in QCD and NLO for the electroweak effects [14, 90], apart from the QED FSR effect, which is already factored in using PHOTOS [89]. There is no full event generation implemented at this level, but the cross-sections can be calculated. Here, FEWZ3.1.2b [91] provides cross-section calculations using the MSTW2008nnlo PDF [24][2]. The Z/γ^* mass region of interest is split into 20 bins with logarithmically increasing width, covering the mass region $M_Z = 120\,\text{GeV}$–$5000\,\text{GeV}$ and a single bin for the region covering 66 GeV–120 GeV, as shown in table 4.2. The POWHEG Drell-Yan sample cross-sections for the same bins are extracted to form the k-factor k_{NNLO}, covering the NNLO QCD and NLO EW corrections:

$$k_{NNLOQCD} = \frac{\sigma_{FEWZ,QCD_{NNLO}+EW_{NLO}}}{\sigma_{MC}}. \tag{4.4}$$

Additionally, real W/Z-radiation corrections [92] are included here as they are not implemented as part of the diboson event generation (see below). Sufficiently energetic electrons produced in the Drell-Yan process can radiate W- and Z-bosons, which can decay into additional electrons. The resultant cross-section modification is calculated in MADGRAPH5 [93] for the fiducial region of $|\eta| < 2.5$ and $p_T > 25\,\text{GeV}$[3]. This factor is applied after the k-factor in the form of a polynomial, yielding the following total k-factor k_{total}:

$$k_{total} = \frac{\sigma_{FEWZ,QCD_{NNLO}+EW_{NLO}}}{\sigma_{MC}} \times k_{W/Z}. \tag{4.5}$$

The POWHEG Drell-Yan Monte Carlo sample, including the nominal k-factor k_{total}, is used as nominal Drell-Yan Monte Carlo sample for this analysis. Three types of theoretical systematic uncertainties are included, α_S-uncertainty, PDF uncertainty and uncertainty due to PDF choice.

The PDF uncertainty is determined using the set of PDF uncertainty eigenvectors, calculating the upward and downward variations of the cross-section following equations 1.15 and 1.16. The PDF uncertainty and the 90% confidence level for upwards

[2] FEWZ calculations provided by U. Klein.
[3] MADGRAPH calculations provided by U. Klein.

Table 4.2: Cross-sections of the FEWZ NNLO calculations and the POWHEG DY sample and the k-factors derived from the cross-sections

M_Z [GeV]	σ_{FEWZ} [pb/GeV]	Stat. Uncert. [%]	$\sigma_{MC,NLO}$ [pb/GeV]	k_{NNLO}	$k_{W/Z}$	k_{total}
66 - 116	2.229×10^{1}	0.022	2.163×10^{1}	1.0305	1.0009	1.0314
116 - 140	3.626×10^{-1}	0.018	3.543×10^{-1}	1.0234	1.0014	1.0249
140 - 169	1.106×10^{-1}	0.017	1.081×10^{-1}	1.0231	1.0018	1.0250
169 - 204	4.179×10^{-2}	0.016	4.114×10^{-2}	1.0158	1.0024	1.0182
204 - 246	1.696×10^{-2}	0.015	1.651×10^{-2}	1.0273	1.0032	1.0305
246 - 297	7.053×10^{-3}	0.014	6.937×10^{-3}	1.0167	1.0042	1.0210
297 - 359	2.922×10^{-3}	0.013	2.879×10^{-3}	1.0149	1.0055	1.0205
359 - 433	1.202×10^{-3}	0.013	1.176×10^{-3}	1.0221	1.0070	1.0293
433 - 522	4.901×10^{-4}	0.012	4.823×10^{-4}	1.0162	1.0091	1.0254
522 - 631	1.938×10^{-4}	0.012	1.937×10^{-4}	1.0005	1.0115	1.0120
631 - 761	7.396×10^{-5}	0.012	7.324×10^{-5}	1.0098	1.0142	1.0242
761 - 919	2.710×10^{-5}	0.011	2.699×10^{-5}	1.0041	1.0163	1.0204
919 - 1110	9.343×10^{-6}	0.011	9.278×10^{-6}	1.0070	1.0189	1.0260
1110 - 1339	3.006×10^{-6}	0.011	3.007×10^{-6}	0.9997	1.0193	1.0190
1339 - 1617	8.852×10^{-7}	0.011	8.912×10^{-7}	0.9933	1.0228	1.0159
1617 - 1951	2.320×10^{-7}	0.012	2.336×10^{-7}	0.9932	1.0258	1.0188
1951 - 2355	5.256×10^{-8}	0.012	5.308×10^{-8}	0.9902	1.0291	1.0190
2355 - 2843	9.739×10^{-9}	0.013	9.866×10^{-9}	0.9871	1.0316	1.0183
2843 - 3432	1.351×10^{-9}	0.014	1.388×10^{-9}	0.9733	1.0346	1.0070
3432 - 4142	1.192×10^{-10}	0.015	1.277×10^{-10}	0.9334	1.0363	0.9673
4142 - 5000	4.921×10^{-12}	0.015	5.826×10^{-12}	0.8447	1.0344	0.8737

and downwards variation in $\alpha_S(M_Z) = 0.1171^{+0.0014}_{-0.0014}$ at NNLO [94] are performed using FEWZ calculations in the same manner as the determination of the nominal value.

VRAP [95] is used to sample the cross-sections for four different PDF sets, ABM11 [96], CT10 [87], HeraPDF1.5 [20, 97] and NNPDF 2.3 [98], using MSTW2008NNLO's preferred $\alpha_S = 0.1171$ to avoid factoring in the already covered α_S uncertainty[4]. In addition, VRAP-values for MSTW2008NNLO are calculated as well to be used as the nominal baseline. Unlike FEWZ, which calculates the integrated process cross-section over a mass range, namely the bins shown in table 4.2, VRAP calculates the exact cross-section at specific mass points in the range 10 GeV–5000 GeV. In order to compare the values to the MSTW2008NNLO baseline, the ratio $\sigma_{PDF}/\sigma_{MSTW2008NNLO}$ is formed and fitted with a spline function. The spline fits are shown in figures 4.2 and 4.3. The spline fits are then integrated over the bins used for the FEWZ calculations, resulting in a set of fractional differences due to the PDF choice. These fractional differences are applied to the k-factor and are shown in 4.4.

An envelope is formed for the α_S-, PDF and PDF choice variations, using the minimum values for each point for the lower bound and the maximum values for each point for the upper bound.

Finally, the nominal k-factor as well as the upper and lower bounds of the 90% C.L. PDF + α_S + PDF choice uncertainty envelope are fitted with a polynomial as shown in figure 4.4. As can be seen in the figure, the k-factor and the uncertainties are within a tight band up to 1000 GeV. Above 1000 GeV, the uncertainties start to increase, with the upper end being driven by the intrinsic 90% C.L. PDF + α_S uncertainty, while the lower end of the uncertainty band is driven by the PDF choice, mainly the contribution from ABM11, mirroring the behaviour shown in figure 4.2. The envelope and fit provides a continuous, mass-dependent description of higher-order corrections to the neutral current Drell-Yan cross-section and the theoretical uncertainties of the process.

4.3 Photon-Induced Di-Lepton Contribution

Photon-induced (PI) di-lepton production is an additional contribution to the SM background [14] with potentially large effects at high masses, as was seen in a mass differential cross-section analysis of the 2011 data at ATLAS [99]. The PI production of

[4] VRAP calculations provided by U. Klein.

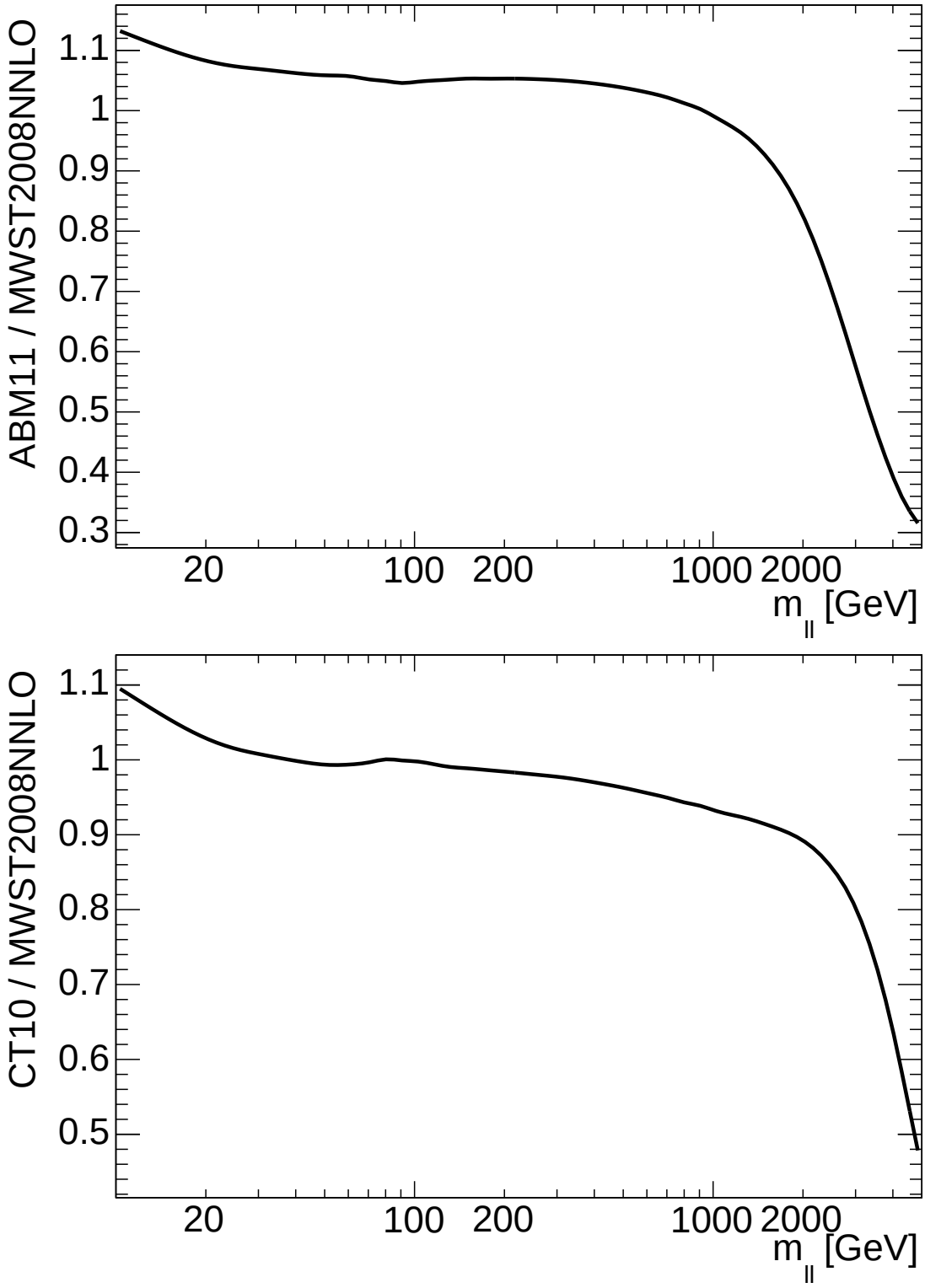

Figure 4.2: Spline fits to the VRAP-ratios of the ABM11 PDF (*top*) and the CT10 PDF (*bottom*) with respect to the nominal MSTW2008NNLO PDF.

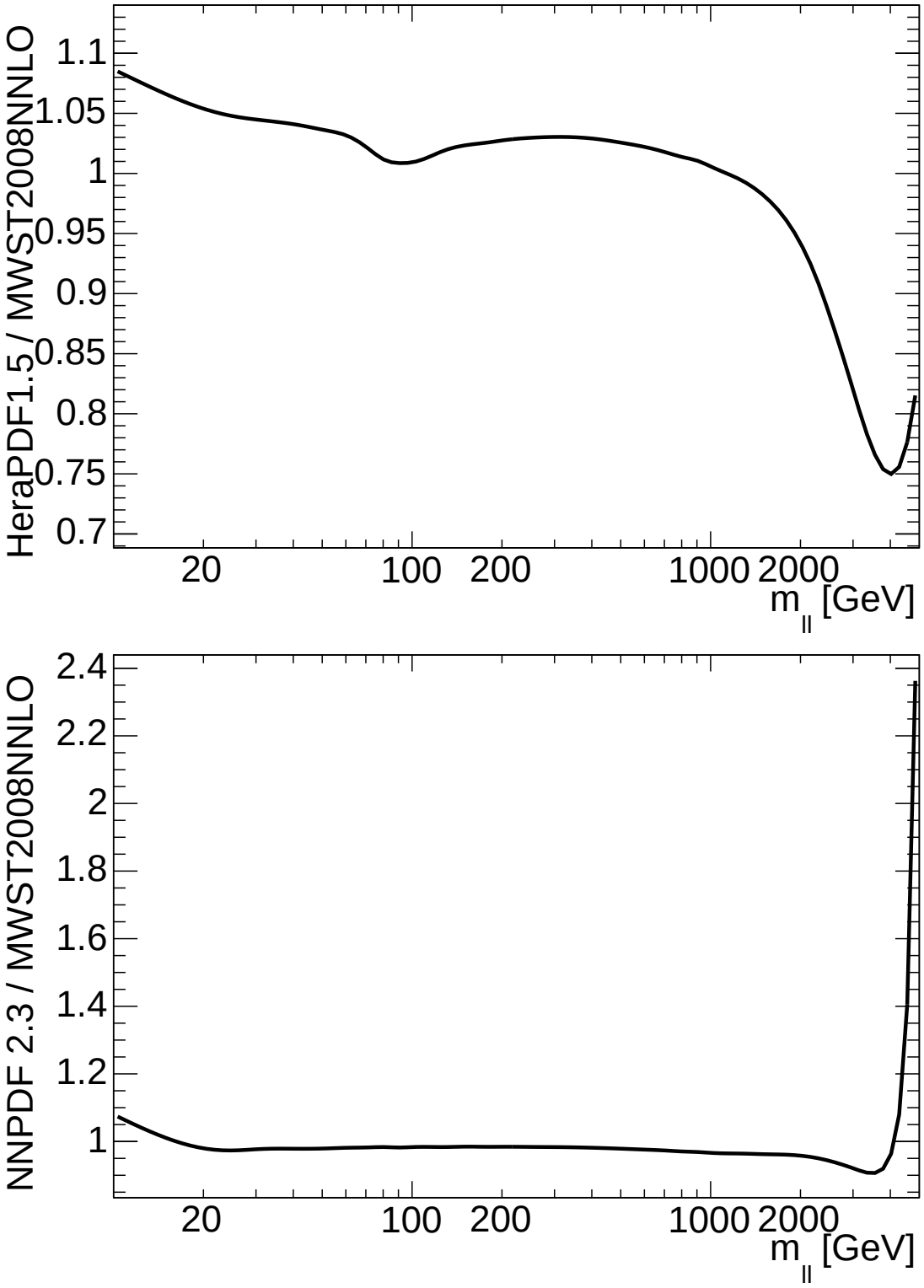

Figure 4.3: Spline fits to the VRAP-ratios of the HeraPDF1.5 PDF (*top*) and the NNPDF 2.3 PDF (*bottom*) with respect to the nominal MSTW2008NNLO PDF.

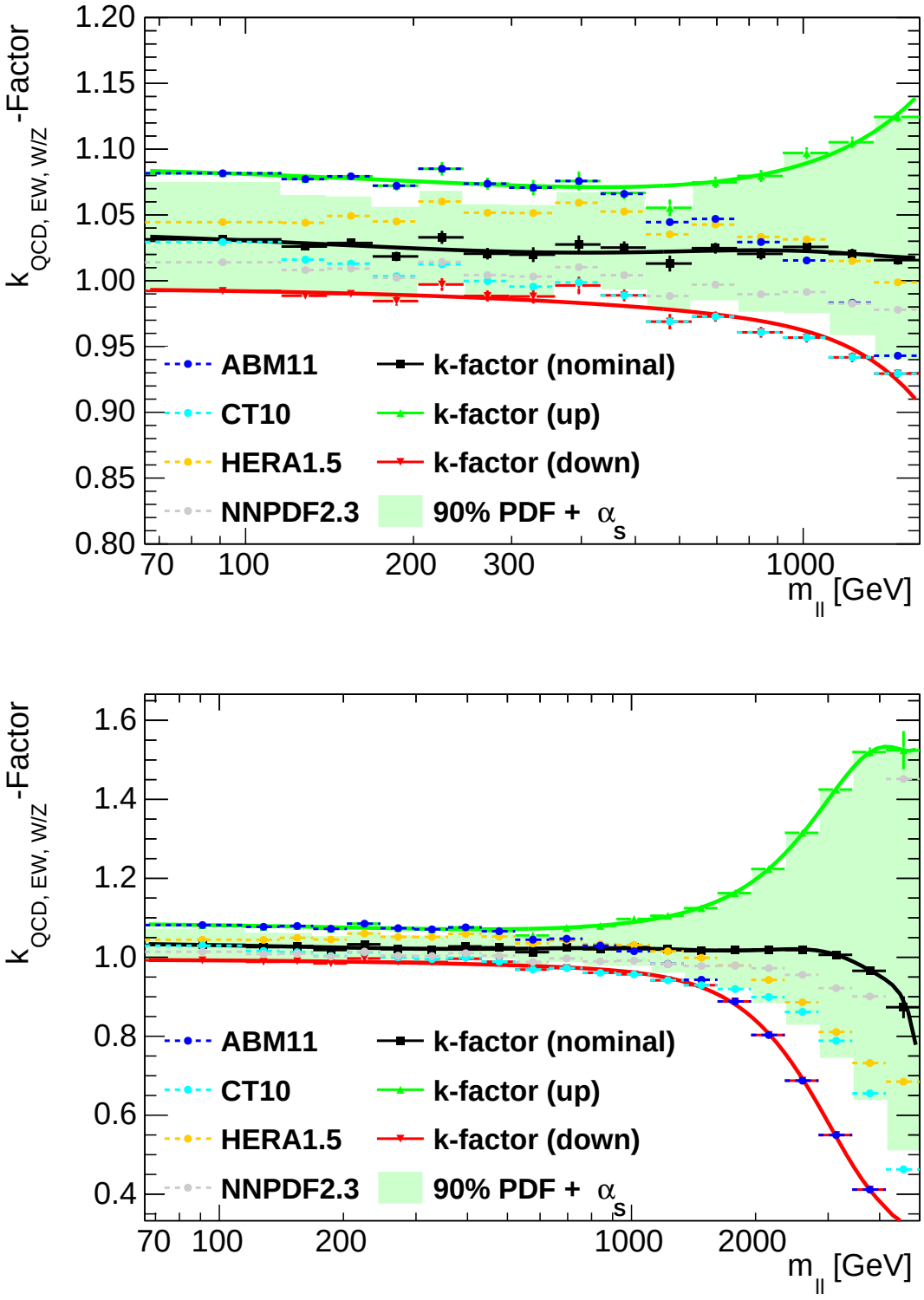

Figure 4.4: Polynomial fits of the nominal k-factor k_{total} and its upward and downward variation with α_S at a 90% confidence level, incorporated PDF uncertainties and the uncertainty due to PDF choice. *Top:* mass region 66 GeV–1617 GeV; *Bottom:* mass region 66 GeV–5000 GeV.

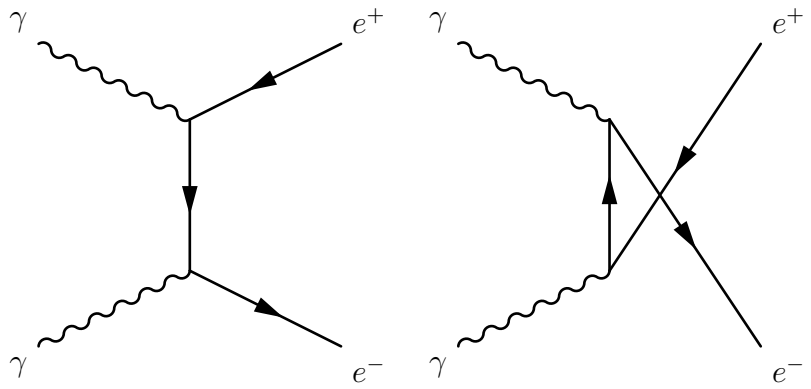

Figure 4.5: Photon-induced $2 \to 2$ production of electrons.

leptons is via photons radiated by the quarks in the proton, illustrated in figure 4.5. The PI production contribution can be described using a cross-section calculation similar to the higher order correction factors that were included, or as a simulated Monte Carlo sample.

The cross-section calculation with FEWZ results in a LO partonic cross-section in the fiducial region $|\eta| < 2.5$ and $p_T > 25\,\text{GeV}$. MRST2004QED [100] is chosen as PDF for the calculation, as it is the most up-to-date PDF with a description of the photon content of the proton. Two parametrisations of the quark mass are possible, using either the current quark mass or the constituent quark mass [90]. These two parametrisations lead to two different cross-section results. Both results are used together to estimate the uncertainty due to the quark mass parametrisation: the mean of both results is taken as the nominal value and the upper and lower values are used as an uncertainty band as shown in table 4.3.

The cross-sections are added to the Drell-Yan sample cross-section (after inclusion of the higher order k-factors) and are fitted with a polynomial. This results in an additional k-factor k_{PI}, that is applied to the Drell-Yan sample, shown in figure 4.6. Here, the upper and lower bands correspond to the two different quark mass parametrisation and the nominal value to the averaged value. Similar to the NNLO k-factor, the effect is small up to around 1000 GeV with a low dependence on mass. At higher masses, the k-factor increases rapidly, as does the associated uncertainty, indicating potentially large effects at high masses.

In order to improve the description of the PI contribution, another approach is considered: a Monte Carlo description of the PI di-lepton production. The PI Monte

Table 4.3: Partonic photon-induced di-lepton production cross-sections within the fiducial region $|\eta| < 2.5$ and $p_T > 25\,\text{GeV}$ as calculated with FEWZ using the MRST2004QED PDF.

m_{ee}[GeV]	σ_{mean} [pb]	Error [%]
66 - 116	3.0151×10^{-1}	35.48
116 - 140	5.1481×10^{-2}	36.36
140 - 169	3.4093×10^{-2}	36.95
169 - 204	2.1701×10^{-2}	37.64
204 - 246	1.3260×10^{-2}	38.38
246 - 297	7.8860×10^{-3}	39.24
297 - 359	4.5065×10^{-3}	40.19
359 - 433	2.4629×10^{-3}	41.24
433 - 522	1.3283×10^{-3}	42.38
522 - 631	7.0543×10^{-4}	43.64
631 - 761	3.5133×10^{-4}	45.01
761 - 919	1.7191×10^{-4}	46.50
919 - 1110	7.9299×10^{-5}	48.10
1110 - 1339	3.4319×10^{-5}	49.94
1339 - 1617	1.3999×10^{-5}	51.95
1617 - 1951	5.1515×10^{-6}	54.18
1951 - 2355	1.6996×10^{-6}	56.72
2355 - 2843	4.7660×10^{-7}	59.63
2843 - 3432	1.0744×10^{-7}	62.93
3432 - 4142	1.7549×10^{-8}	66.81
4142 - 5000	1.7505×10^{-9}	71.01

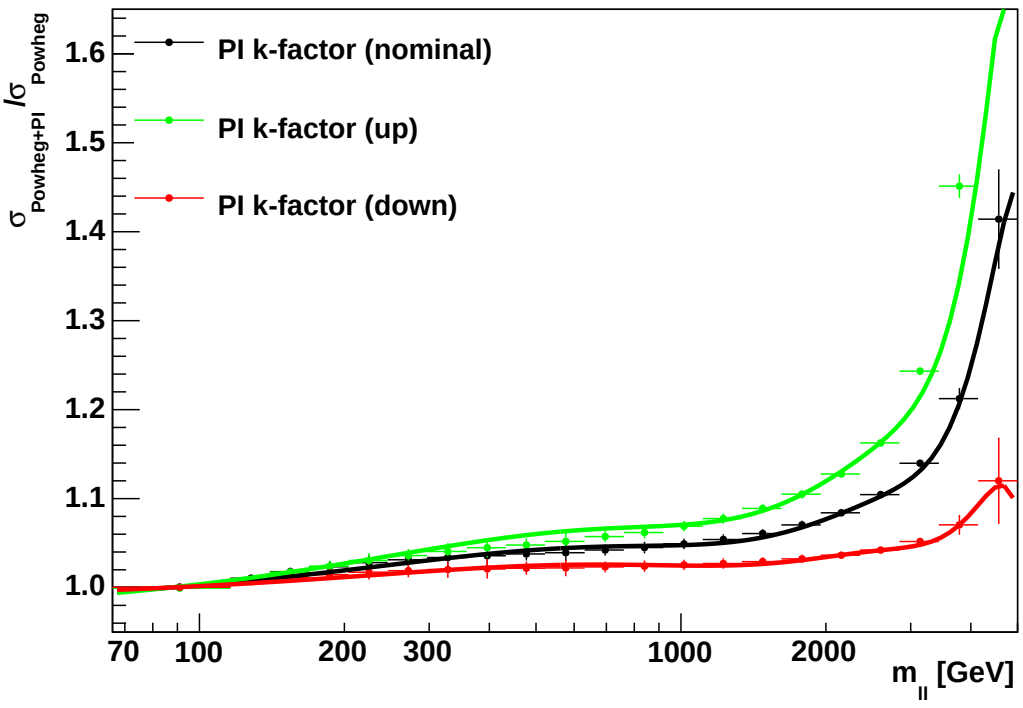

Figure 4.6: Photon-induced background contribution within the fiducial range $|\eta| < 2.5$ and $p_T > 25\,\text{GeV}$ as a k-factor for the nominal POWHEG Drell-Yan sample.

Table 4.4: List of Photon-Induced Monte Carlo samples, listing the generation range, internal MC run identifier, cross-section, number of generated events, filter efficiency and associated Monte Carlo luminosity.

m_{ee}[GeV]	MC Run	$\sigma\times$ Br [pb]	N_{gen} $[1 \times 10^3]$	ϵ_{Filter} [%]	L_{MC} [fb^{-1}]
7 - 20	129650	1.5037×10^2	500	2.343	1.378×10^2
20 - 60	129651	2.6653×10^1	500	32.48	5.751×10^1
60 - 200	129652	2.6976×10^0	500	100	1.814×10^2
200 - 600	129653	1.2184×10^{-1}	200	100	1.634×10^3
600 - 1500	129654	3.4933×10^{-3}	100	100	2.853×10^4
1500 - 2500	129655	5.8593×10^{-5}	100	100	1.698×10^6
2500+	129656	2.2978×10^{-6}	100	100	4.334×10^7

Carlo samples, listed in table 4.4, are generated with the Pythia8 event generator using the MRST2004QED PDF.

The PI k-factor approach is compared to the Monte Carlo samples, as shown in figure 4.7, showing very good agreement for the upper value for the Fewz-calculation. As the k-factor method is only a scaled version of the DY kinematic distribution, the k-factor method will always mirror the kinematic distribution of the DY samples. These deviations from the k-factor method can be seen in several kinematic distributions, chiefly $\Delta\eta$ and ΔR shown in figure 4.8. As the Monte Carlo sample is capable of delivering additional information, the Monte Carlo sample is preferred over the PI k-factor method in this analysis.

The systematic uncertainty on the PI cross-section is taken from the k-factor method, using the uncertainties shown in table 4.3 and shown in figure 4.9.

4.4 Remaining Background Simulations

Two more types of SM backgrounds are modelled using Monte Carlo simulation samples, the top and the diboson background.

The cross-section for $t\bar{t}$ production is significant to this analysis as a background. As $t\bar{t}$ pairs can undergo decay into leptons, they can result in a di-lepton final state. Mc@Nlo [101, 102, 103] is used with CT10 as PDF to generate the relevant event

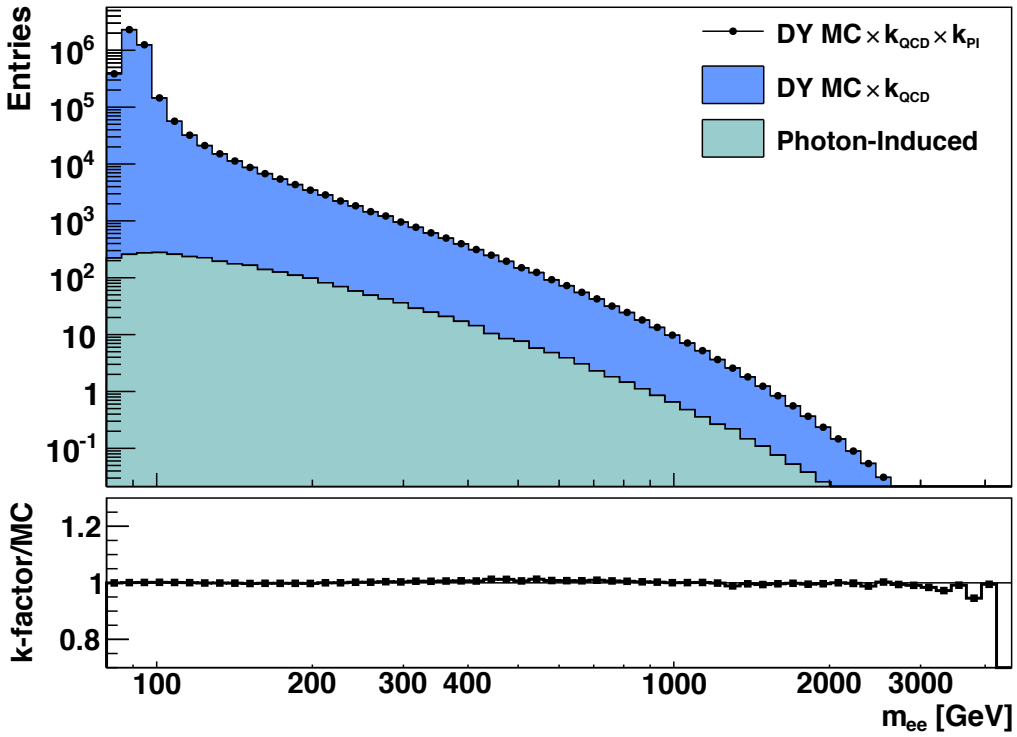

Figure 4.7: Comparison of the generator level invariant mass spectrum m_{ee} of the simulated PI sample (turquoise) in addition to the nominal POWHEG Drell-Yan sample (light blue) and the k-factor approach to PI estimation (circles). Comparison covers the fiducial region $|\eta| < 2.5$ and $p_T > 25\,\text{GeV}$.

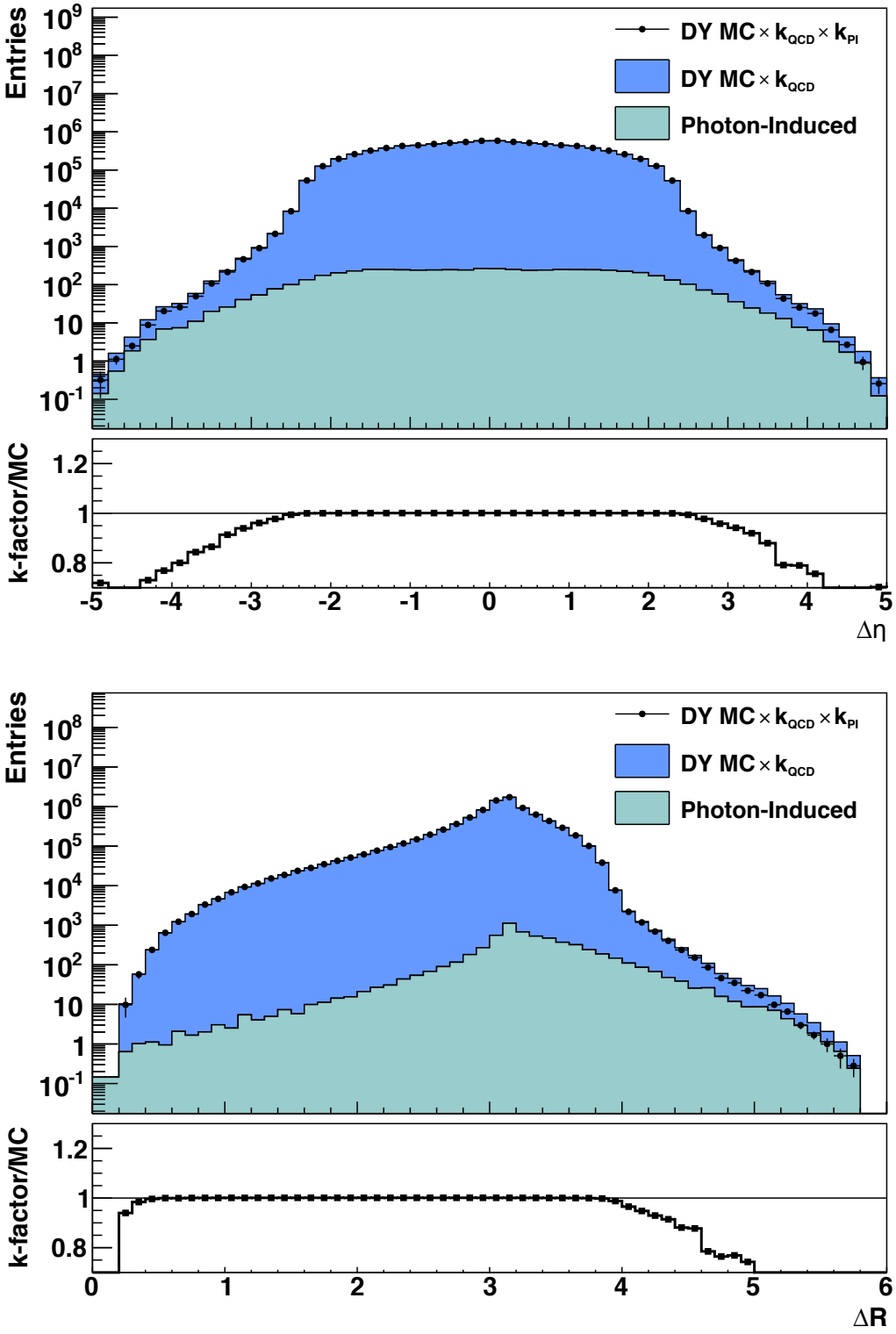

Figure 4.8: Comparison of the generator level spectra for $\Delta\eta$ and ΔR of the simulated PI sample (turquoise) in addition to the nominal POWHEG Drell-Yan sample (light blue) and the k-factor approach to PI estimation (circles). Comparison covers the fiducial region of $|\eta| < 2.5$ and $p_T > 25\,\text{GeV}$.

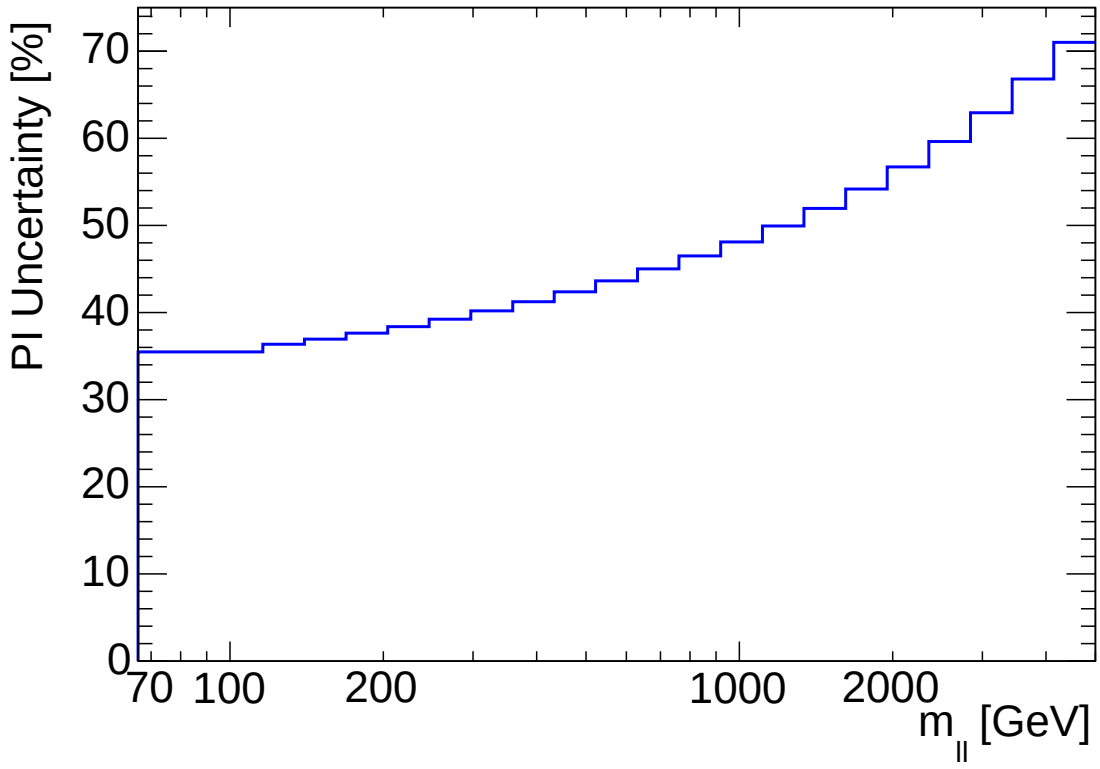

Figure 4.9: Systematic uncertainty on the PI cross-section derived from the PDF parametrisation differences as described in the text.

sample. The cross-section used to calculate the integrated luminosity of the sample is provided by ATLAS at the NNLO level using HATHOR [104] and is predicted to be: $\sigma_{t\bar{t}} = 252.89^{+13.30}_{-14.52}$ pb at $\sqrt{s}$ =8 TeV. For searches, an additional uncertainty is introduced by varying the top mass by ±1GeV, resulting in an additional uncertainty of +7.56 and −7.30pb. As the cross-section uncertainty translates directly to the number of events, this is a total systematic uncertainty of 6%.

The second top-based process contribution is tW production. Here, b-quarks from the hard event convert into t-quarks by radiating a W-boson. The W-boson and the top can both decay leptonically, resulting in a di-lepton configuration. As with the $t\bar{t}$ background, the process is simulated using MC@NLO using the CT10 PDF. The NNLO cross-section provided by ATLAS using HATHOR is $\sigma_{tW} = 22.37$ pb at $\sqrt{s}$ =8 TeV. The associated systematic uncertainty on the cross-section is ±1.52 pb, a total uncertainty of 7%.

The second type of SM background is due to diboson production. Diboson samples simulate the production of two vector bosons, i.e. WW, WZ or ZZ pairs, and their subsequent decay. The samples do not include the production of an additional boson via real W/Z-radiation, as mentioned earlier. Since W- as well as Z-bosons can decay leptonically, both processes contribute to the background. The diboson background samples are generated with HERWIG [105, 106] using CTEQ6L1 [107] as PDF. Each of the three diboson combinations is generated in three binned samples, similar to the Drell-Yan background. The samples are then scaled to NLO cross-sections provided by theory calculations [108] as shown in table 4.5. The systematic uncertainty on the NLO cross-sections (and hence number of events) is 5%.

Table 4.5: List of diboson and top Monte Carlo samples, showing the generation range, the internal MC run identifiers, the cross-sections, number of generated events, filter efficiencies and associated Monte Carlo luminosity.

Process	m_{ee} [GeV]	MC Run	$\sigma\times$ Br [pb] MC	$\sigma\times$ Br [pb] Theory	N_{gen} $[1\times10^3]$	ϵ_{Filter} [%]	L_{MC} [fb^{-1}]
WW	20+	105985	3.2501×10^{1}	5.6829×10^{1}	2500	38.21	1.147×10^{2}
	400 - 1000	180451	3.7892×10^{-1}	6.6255×10^{-1}	10	0.0718	2.094×10^{3}
	1000+	180452	3.7892×10^{-1}	6.6255×10^{-1}	10	0.0010	1.455×10^{5}
ZZ	20+	105986	4.6914×10^{0}	7.3586×10^{0}	250	21.17	1.566×10^{2}
	400 - 1000	180455	3.4574×10^{-1}	5.4229×10^{-1}	10	0.1302	1.146×10^{4}
	1000+	180456	3.4574×10^{-1}	5.4229×10^{-1}	10	0.0029	6.014×10^{5}
WZ	20+	105987	1.2009×10^{1}	2.1478×10^{1}	1000	30.55	1.519×10^{2}
	400 - 1000	180453	4.6442×10^{-1}	8.3060×10^{-1}	10	0.3086	3.882×10^{3}
	1000+	180454	4.6442×10^{-1}	8.3060×10^{-1}	10	0.0114	1.053×10^{5}
$t\bar{t}$		105200	2.0813×10^{2}	2.5289×10^{2}	15000	54.26	8.385×10^{1}
tW		105467	2.067×10^{1}	2.237×10^{-1}	2000	100.0	7.869×10^{1}

Chapter 5

Simulated Signal Processes

As outlined in chapter 4, Monte Carlo samples are used to simulate physics processes. They can not only describe SM processes, but can also make event predictions based on theories for new physics, the Z'_{SSM} in this analysis. This chapter gives a list of the samples used for Z'_{SSM} descriptions (5.1), the reweighting process used to produce additional samples over a wide range of Z'_{SSM} masses (5.2) and the correction factors incorporated into the samples (5.3) mirroring the k-factors used for the SM processes.

5.1 Overview of Signal Samples

The Monte Carlo samples described in chapter 4 only model SM processes. In order to perform a search, it is necessary to know the expected signal as well. This is done using seven Monte Carlo samples. Six of these samples are Z'_{SSM} samples at Z'_{SSM} masses of 0.5, 1.0, 1.5, 2.0, 2.5 and 3.0 TeV, generated using PYTHIA8 using the MSTW2008LO PDF [24]. Additionally, a PYTHIA8 Z/γ^* sample using the MSTW2008LO PDF [24] forms part of the signal-related samples as described in the next section. Table 5.1 describes the Z'_{SSM} and the PYTHIA8 Z/γ^* samples and their parameters.

5.2 Signal Template Generation

This PYTHIA8 Z/γ^* sample is used as a basic template to produce more Z'_{SSM} samples. This is done by effectively replacing the matrix element in equation 1.8 calculated for

Table 5.1: List of PYTHIA8 Monte Carlo Z'_{SSM} signal and Drell-Yan samples used for reweighting.

Process	m_{ee}[GeV]	MC Run	$\sigma\times$ Br [pb]	N_{gen} $[1 \times 10^3]$
NC DY	75 - 120	145963	8.654×10^{2}	300
	120 - 180	145964	7.977×10^{0}	100
	180 - 250	145965	1.265×10^{0}	100
	250 - 400	145966	4.392×10^{-1}	100
	400 - 600	145967	7.257×10^{-2}	100
	600 - 800	145968	1.250×10^{-2}	100
	800 - 1000	145969	3.186×10^{-3}	100
	1000 - 1250	145970	1.120×10^{-3}	100
	1250 - 1500	145971	3.174×10^{-4}	100
	1500 - 1750	145972	1.022×10^{-4}	100
	1750 - 2000	145973	3.552×10^{-5}	100
	2000 - 2250	145974	1.295×10^{-5}	100
	2250 - 2500	145975	4.908×10^{-6}	100
	2500 - 2750	145976	1.906×10^{-6}	100
	2750 - 3000	145977	7.467×10^{-7}	100
	3000+	145978	4.748×10^{-7}	100
$Z'_{SSM}(0.5\,\text{TeV})$	250 - 750	158019	2.854×10^{0}	20
$Z'_{SSM}(1.0\,\text{TeV})$	500 - 1500	158020	1.515×10^{-1}	20
$Z'_{SSM}(1.5\,\text{TeV})$	750 - 2250	158021	1.948×10^{-2}	20
$Z'_{SSM}(2.0\,\text{TeV})$	1000 - 3000	158022	3.410×10^{-3}	20
$Z'_{SSM}(2.5\,\text{TeV})$	1250 - 3750	158023	7.470×10^{-4}	20
$Z'_{SSM}(3.0\,\text{TeV})$	1500 - 4500	158024	1.893×10^{-4}	20

Z/γ^* with the corresponding Z'_{SSM} matrix element,

$$\sigma(pp \to Z\gamma^* \to e^+e^-) \to \sigma(pp \to Z'_{SSM} \to e^+e^-). \tag{5.1}$$

Technically, this is done by reweighting every event according to the ratio of squared amplitudes, based on the incoming quarks and the mass of the Z/γ^* found in the event record of the PYTHIA8 sample:

$$w(m,q) = \frac{\sum_{i,j} |A_{ij}(Z')|^2}{\sum_{i,j} |A_{ij}(Z/\gamma^*)|^2}, \tag{5.2}$$

where the amplitude $A_{ij}(Z/\gamma^*)$ is given by equation 1.10. The Z'_{SSM} amplitude is given by:

$$A(Z') = g^2_{Z'} \frac{g'_{qi} g'_{ej}}{m^2 - M^2_{Z'} - iM_{Z'}\Gamma_{Z'}}, \tag{5.3}$$

where $g_{Z'}$ is the Z' coupling and the charges g' are dependent on the incoming and outgoing fermions. This mirrors the SM amplitude for the DY process structurally but does not include the γ contribution, only the Z contribution, modified to use the properties of the Z'_{SSM} instead of the properties of the Z. For the Z'_{SSM}, it is assumed that it couples to SM fermions the same way as the SM Z boson.

Additionally, the reweighting procedure can be further improved by taking into account the effect of the Drell-Yan process itself by including the amplitude of the neutral current DY process as follows:

$$w(m,q) = \frac{\sum_{i,j} |A_{ij}(Z') + A_{ij}(Z/\gamma^*)|^2}{\sum_{i,j} |A_{ij}(Z/\gamma^*)|^2}, \tag{5.4}$$

which is the weight that is applied to each event, using the quark q and generator mass m of each event.

The reweighting is then compared to the dedicated signal samples to validate the outcome of the procedure as both should result in the same invariant mass spectra. As the dedicated samples are only generated with "truth" masses M_{gen} in the range $0.5M_{Z'} < M_{gen} < 1.5M_{Z'}$, the comparison is only made within that range as shown in figure 5.1, which covers the agreement for the highest and lowest mass dedicated sample. Figure 5.2 shows the comparisons for intermediate Z' masses with a similarly good agreement between the reweighted and the dedicated samples.

Hence, the reweighted sample is used for the rest of the analysis as it delivers results agreeing with the dedicated samples but offers more fine-grained steps than the 500 GeV steps of the dedicated sample. In order to produce an array of reweighted mass points, the reweighting procedure is repeated for the range of 150 GeV–3500 GeV, with one sample every 50 GeV. The invariant mass distributions resulting from this procedure can be seen in figure 5.3, showing the m_{ee} distributions for each target Z'_{SSM} pole mass the sample is reweighted to.

5.3 Higher Order QCD Correction

Finally, the PYTHIA8 sample (and derived Z'_{SSM} templates) are corrected using a k-factor as the PYTHIA8 sample is only at leading order. This is done in the same fashion as the NNLO k-factor for the POWHEG-based Drell-Yan samples in chapter 4.2, using FEWZ calculations with the MSTW2008nnlo PDF together with the Monte Carlo cross-section, using equation 4.4.

Unlike the calculation in 4.2, however, this k-factor only includes QCD-based NNLO corrections, as the EW corrections do not apply in the same form to the Z'_{SSM} boson. The cross-sections used to calculate the k-factor are shown in table 5.2 and the resultant k-factor and fit is shown in figure 5.4. Noteworthy is the generally lower cross-section of PYTHIA8 compared to POWHEG, showing the effect of using a LO MC generator like PYTHIA8 versus a NLO-based generator such as POWHEG. As can be seen in table 4.2 and 5.2, the cross-sections with and without the higher order EW corrections are very similar and the effect of the EW corrections only becomes apparent at high masses.

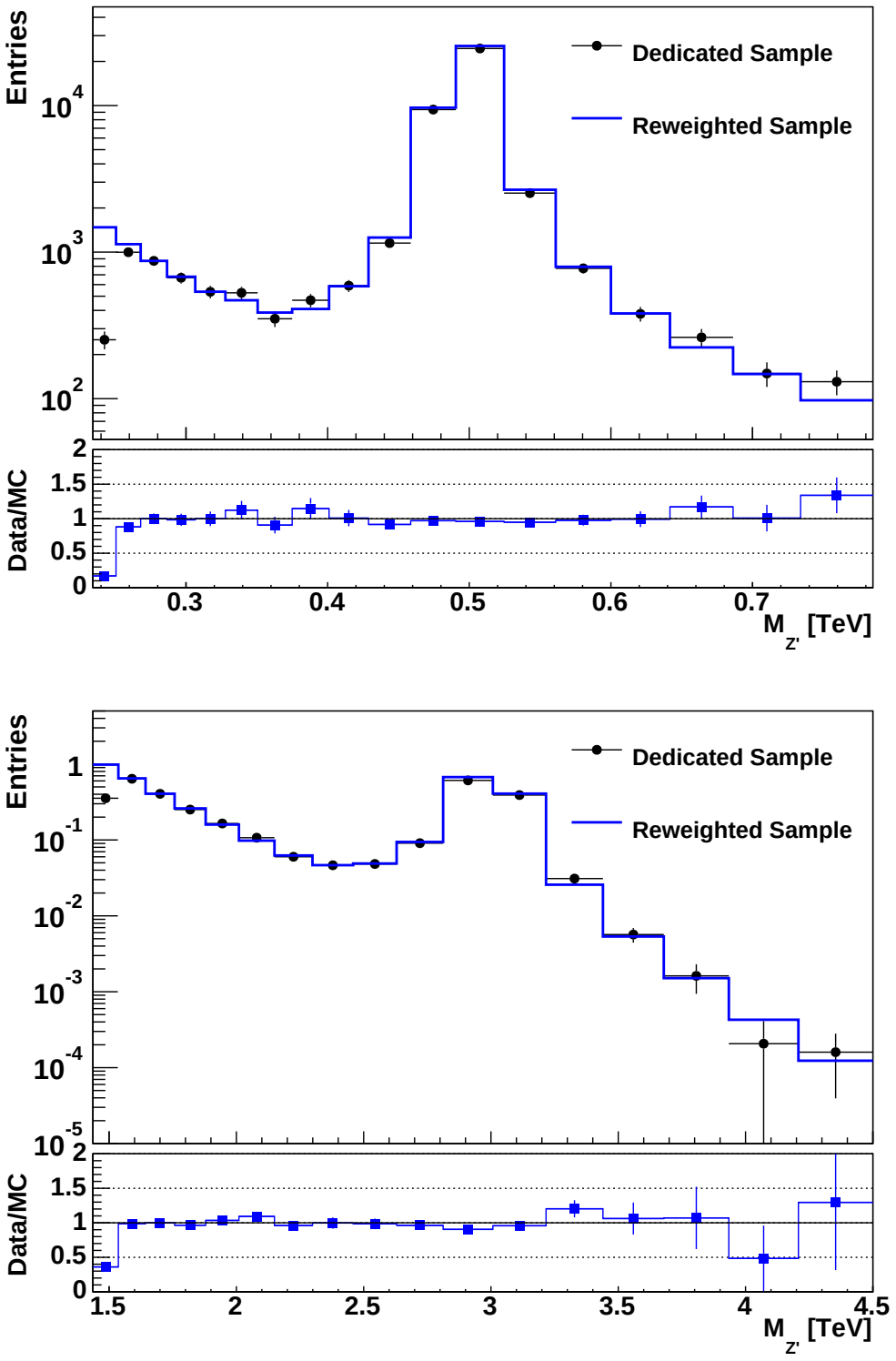

Figure 5.1: *Top:* PYTHIA8 Drell-Yan sample reweighted to a Z'_{SSM} pole mass of 500 GeV. *Bottom:* PYTHIA8 Drell-Yan sample reweighted to a Z'_{SSM} pole mass of 3000 GeV. The reweighted samples are compared to dedicated samples generated with Z'_{SSM} pole masses of 500 GeV and 3000 GeV, respectively. All samples are normalised to the data luminosity of L =20.3 fb^{-1}.

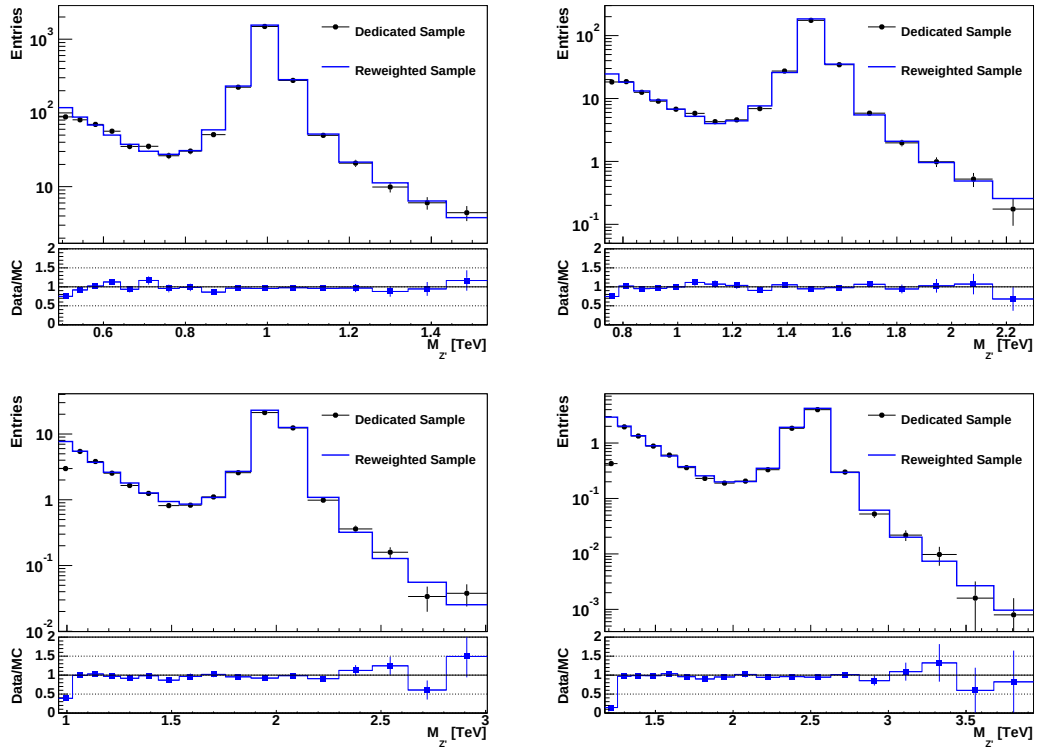

Figure 5.2: PYTHIA8 Drell-Yan samples reweighted to Z'_{SSM} pole masses of 1000 GeV (*top left*), 1500 GeV (*top right*), 2000 GeV (*bottom left*) and 2500 GeV (*bottom right*) and the corresponding dedicated Z'_{SSM} samples. All samples are normalised to the data luminosity of L =20.3 fb^{-1}.

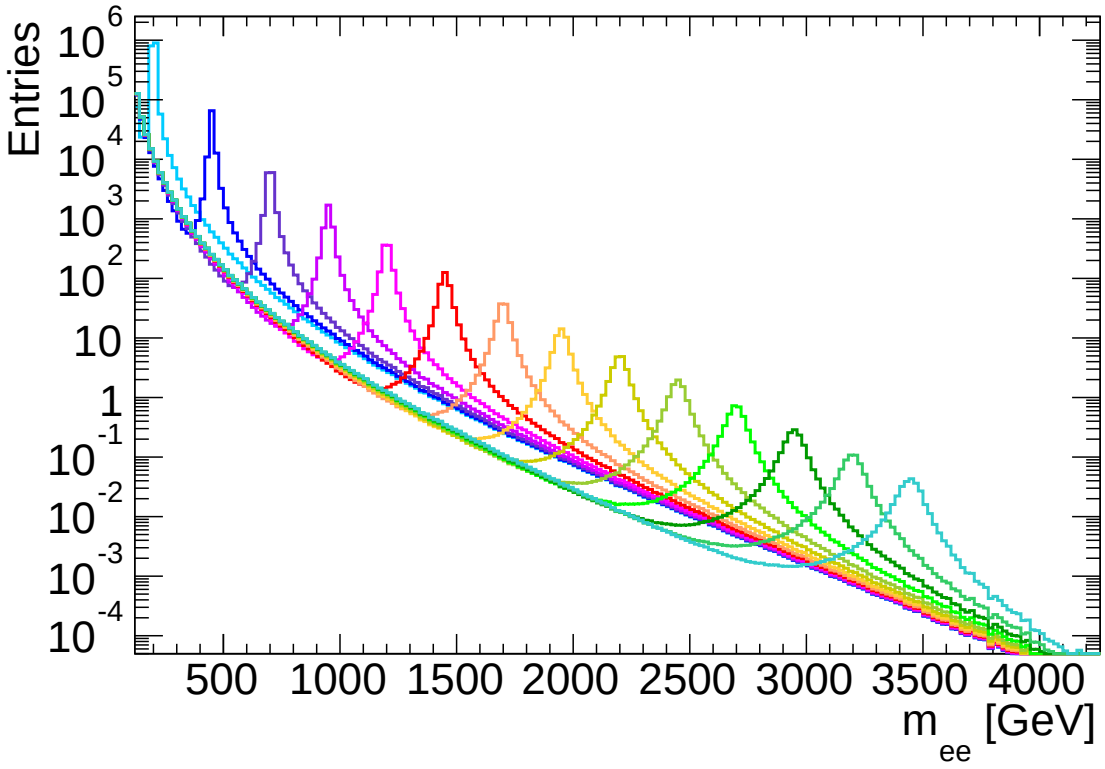

Figure 5.3: Invariant mass spectra for the PYTHIA8 Drell-Yan Sample reweighted to Z'_{SSM} pole masses from 250 GeV–3500 GeV in 250 GeV steps.

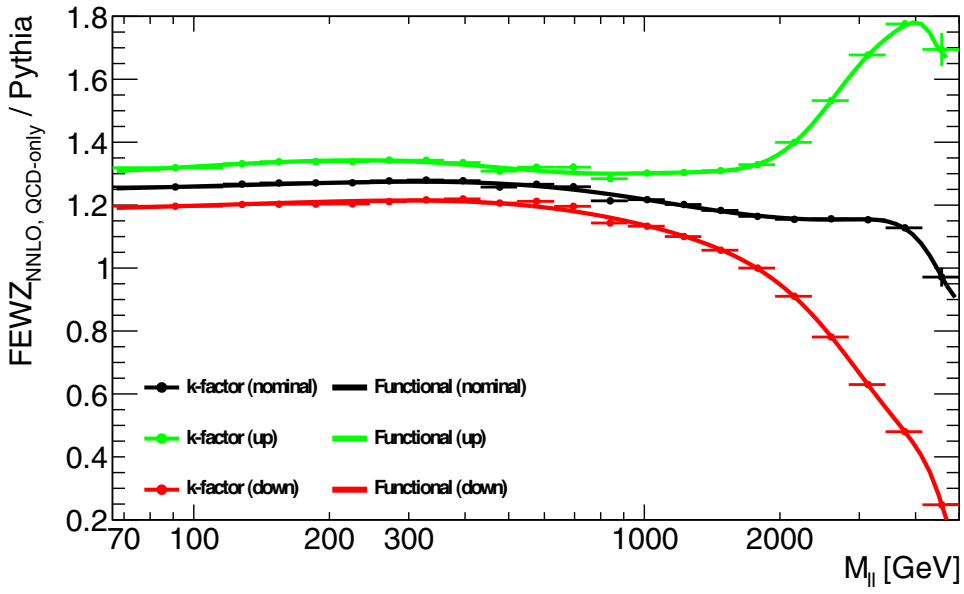

Figure 5.4: QCD-only k-factor derived from the PYTHIA8 sample and FEWZ calculations used to correct the samples to NNLO in QCD as described in the text.

Table 5.2: Cross-sections of the FEWZ NNLO calculations and the PYTHIA8 DY sample and the k-factor derived from the cross-sections.

M_Z [GeV]	$\sigma_{FEWZ,NNLO}$ [pb/GeV]	Stat. Uncert. [%]	σ_{MC} [pb/GeV]	k_{NNLO}
66 - 116	2.235×10^{1}	0.05	1.777×10^{1}	1.2577
116 - 140	3.655×10^{-1}	0.40	2.885×10^{-1}	1.2669
140 - 169	1.111×10^{-1}	0.56	8.745×10^{-2}	1.2704
169 - 204	4.183×10^{-2}	0.59	3.292×10^{-2}	1.2707
204 - 246	1.698×10^{-2}	0.47	1.336×10^{-2}	1.2710
246 - 297	7.070×10^{-3}	0.43	5.536×10^{-3}	1.2771
297 - 359	2.937×10^{-3}	0.56	2.295×10^{-3}	1.2797
359 - 433	1.214×10^{-3}	0.67	9.502×10^{-4}	1.2776
433 - 522	4.964×10^{-4}	0.45	3.948×10^{-4}	1.2573
522 - 631	1.973×10^{-4}	0.64	1.558×10^{-4}	1.2664
631 - 761	7.573×10^{-5}	0.89	6.018×10^{-5}	1.2584
761 - 919	2.795×10^{-5}	0.82	2.303×10^{-5}	1.2136
919 - 1110	9.725×10^{-6}	0.39	7.988×10^{-6}	1.2175
1110 - 1339	3.160×10^{-6}	0.39	2.629×10^{-6}	1.2020
1339 - 1617	9.406×10^{-7}	0.34	7.950×10^{-7}	1.1831
1617 - 1951	2.494×10^{-7}	0.32	2.142×10^{-7}	1.1643
1951 - 2355	5.727×10^{-8}	0.29	4.959×10^{-8}	1.1549
2355 - 2843	1.075×10^{-8}	0.27	9.295×10^{-9}	1.1563
2843 - 3432	1.510×10^{-9}	0.28	1.309×10^{-9}	1.1536
3432 - 4142	1.341×10^{-10}	0.75	1.189×10^{-10}	1.1278
4142 - 5000	5.547×10^{-12}	3.11	5.711×10^{-12}	0.9713

Chapter 6

Event and Electron Selection

The data recorded by ATLAS results from the sum of all processes observed during collisions that trigger the detector. In order to analyse a specific event signature of interest, selection criteria have to be applied. This chapter describes the specific data samples[1] used in this analysis (6.1) and the selection requirements used to find the di-electron events of interest (6.2), followed by the results of the selection (6.3) and corrections to the Monte Carlo samples based on data (6.4, 6.5).

6.1 Data Samples

The data after recording (as described in chapter 3.6) is stored at CERN. The data is stored as RAW data after the event filter in a byte stream representing the output of the detector itself [109]. The data is then processed and events are reconstructed, resulting in Event Summary Data (ESD) which contains all data needed for anything but re-reconstruction. The ESD are further processed into Analysis Object Data (AOD) which contain the data in the form of individual physics objects, such as electrons, muons or jets. As the AOD data sets are still large in size, and it is not feasible to analyse them on local computers, they are further processed into n-tuples containing only events with at least one electron with $p_T > 14\,\text{GeV}$ and one or more additional electrons with $p_T > 9\,\text{GeV}$. Additionally, these n-tuples only contain objects with variables of interest to the analysis, meaning non-electron objects are largely discarded as well as variables not needed for the event selection[2].

[1] From here on, the use of "data" in plots denotes data analysed in the context of this analysis unless noted otherwise.

[2] N-tupling provided by J. Kretzschmar

Using both, GRL and trigger requirements, the total integrated luminosity of the sample is determined to be $20.3\,\mathrm{fb}^{-1}$ with a luminosity uncertainty of $\pm 2.8\%$ [72, 110].

6.2 Electron Candidate Selection

The event selection narrows down the collected events further by removing event candidates that are deemed to be background events. This is done by imposing a set of selection criteria. The requirements are chosen to reject background events and retain events of interest. An analysis using successive requirements in order to reject events is commonly called a "cut-based" analysis with each requirement being a "cut" as it splits the set of candidates into rejected and selected events.

As described above, all events must contain at least two electron candidates. During the selection of individual electrons, all electron candidates not passing the requirements are rejected. An event candidate is rejected in its entirety if there are less than two viable electron candidates left after a selection is applied. Furthermore, the electrons are ordered in transverse momentum p_T, from highest to lowest. The electron highest in p_T is called the "leading electron", the electron with the second-highest p_T is the "subleading electron". Since the analysis concentrates on di-electron events, the leading and subleading electrons are the ones defining the event.

The first half of the event selection primarily focuses on variables applicable to the entire event with the number of events shown in table 6.1. First, as described above, each event must be within a luminosity block valid for analysis as determined by the GRLs[3]. Next, events must pass the trigger (*EF_g35_loose_g25_loose*) requiring at least two energy depositions with a loose photon identification, one with $E_T > 35\,\mathrm{GeV}$ and one with $E_T > 25\,\mathrm{GeV}$. As the electron identification is a subset of the photon identification, all electrons with loose or better identification will also be contained in the loose photon set. Events are also required to contain at least one primary vertex with more than two tracks. Finally, events with noise bursts in either calorimeter are discarded. Notably, the trigger is the main criterion responsible for the selection on a global event level with only 7.12% efficiency while the data quality-based cuts all have an efficiency of over 95%, meaning the requirement for two electron-like objects is the main selection on this level.

[3]Used GRL: Period: data12_8TeV.AllYear, defect: PHYS_CombinedPerf_Egamma_Eg_standard, defect tag: DetStatus-v61-pro14-02.

Table 6.1: Selection criteria applied to event candidates on a global level, showing the total number of events after each applied selection criterion as well as the relative efficiency with respect to the previous selection criterion.

Selection Criterion	Rel. Eff. [%]	Events
Input	—	6.699×10^8
Good Run List	95.64	6.408×10^8
Trigger	7.115	4.560×10^7
Primary Vertices	99.99	4.560×10^7
Noise Burst Cleaning	99.78	4.550×10^7
Combined (event-level)	6.79	—

The second half of the event selection subjects individual electron candidates to selection criteria, sometimes called "object level" selection. The selection criteria and efficiencies are shown in table 6.2. First, the reconstruction algorithm is checked: electrons passing the selection must be reconstructed either from a calorimeter-based cluster seed or a cluster seed in conjunction with a tracker-based track seed[4]. Next, the electron must be within the fiducial region of the detector, meaning electrons passing the selection must have $|\eta| < 2.47$ and must be outside the region $1.37 < |\eta| < 1.52$, the transition region between the barrel and end cap ECAL (see chapter 3.3). Electrons must fulfil an object quality check, discarding all electrons associated with so-called "hot cells" in the calorimeter which are known to have problems at the time of recording. All electrons must have $p_T > 30\,\text{GeV}$ and be identified as *medium* electrons, removing over 75% of all event candidates at this stage. Next, the leading electron must have a $p_T > 40\,\text{GeV}$. Together with the previous requirement of $p_T > 30\,\text{GeV}$, this ensures that the trigger is operating at full efficiency.

The pair of electrons with the highest p_T must fulfil the isolation requirement. Isolation describes the amount of energy deposited within a certain area around the electron cluster in the calorimeter, excluding the cluster itself. This area is described in $\eta - \phi$-space, using a cone of $\Delta R < 0.2$ in size centred on the electron cluster (E_T^{C20}). The transverse energy within this cone must be sufficiently low: $E_T^{\text{C20}} \leq 0.007 E_T + 5$ GeV for the leading and $E_T^{\text{C20}} \leq 0.022 E_T + 6$ GeV for the subleading electron. If this electron pair passes the isolation requirement, it is used to form the invariant mass, m_{ee}. The invariant mass m_{ee} is used for the final selection requirement of $m_{ee} > 80\,\text{GeV}$.

[4]In ATLAS, this criterion is called the "electron author".

Table 6.2: Selection criteria applied to event candidates on an electron object level, showing the total number of events after each applied selection criterion as well as the relative efficiency with respect to the previous selection criterion.

Selection Criterion	Rel. Eff. [%]	Events
Event-level selection	—	4.550×10^7
Reconstruction Algorithm	81.71	3.717×10^7
Kinematic Range	89.92	3.343×10^7
Object Quality	99.49	3.326×10^7
$p_T > 30\,\text{GeV}$	67.69	2.251×10^7
Medium ID	23.57	5.306×10^6
Leading $p_T > 40\,\text{GeV}$	86.17	4.572×10^6
Isolation	99.01	4.527×10^6
$m_{ee} > 80\,\text{GeV}$	97.55	4.416×10^6
Combined (object-level)	9.71	—

On the object level, the main rejection of events stems from the electron identification with a relative efficiency of 23.57%, showing its power in background rejection. Both p_T cuts contribute significantly to the event rejection as well but are of less importance as events of interest will typically have high p_T electrons (due to the high invariant mass for events of interest). Together with the selection efficiencies seen on the event-level, it becomes clear that finding two well-identified electrons is the main selection, while the other requirements have a small impact.

In total, 4 415 785 events pass the full event selection in $20.3\,\text{fb}^{-1}$ of data, giving an average event yield of $217.77 \pm 0.10\,\text{pb}$. Taken run-by-run, as shown in 6.1. In order to verify that the yield is stable over time, a constant was fitted to the yield, resulting in a fitted average yield of $217.75 \pm 0.10\,\text{pb}$ with a $\chi^2/d.o.f. = 1.88$. The fitted yield and the global average show agreement, but the quality of the fit shows a deviation from the assumption that the yield is constant over time which is attributed to a decline in detector performance with overall run time.

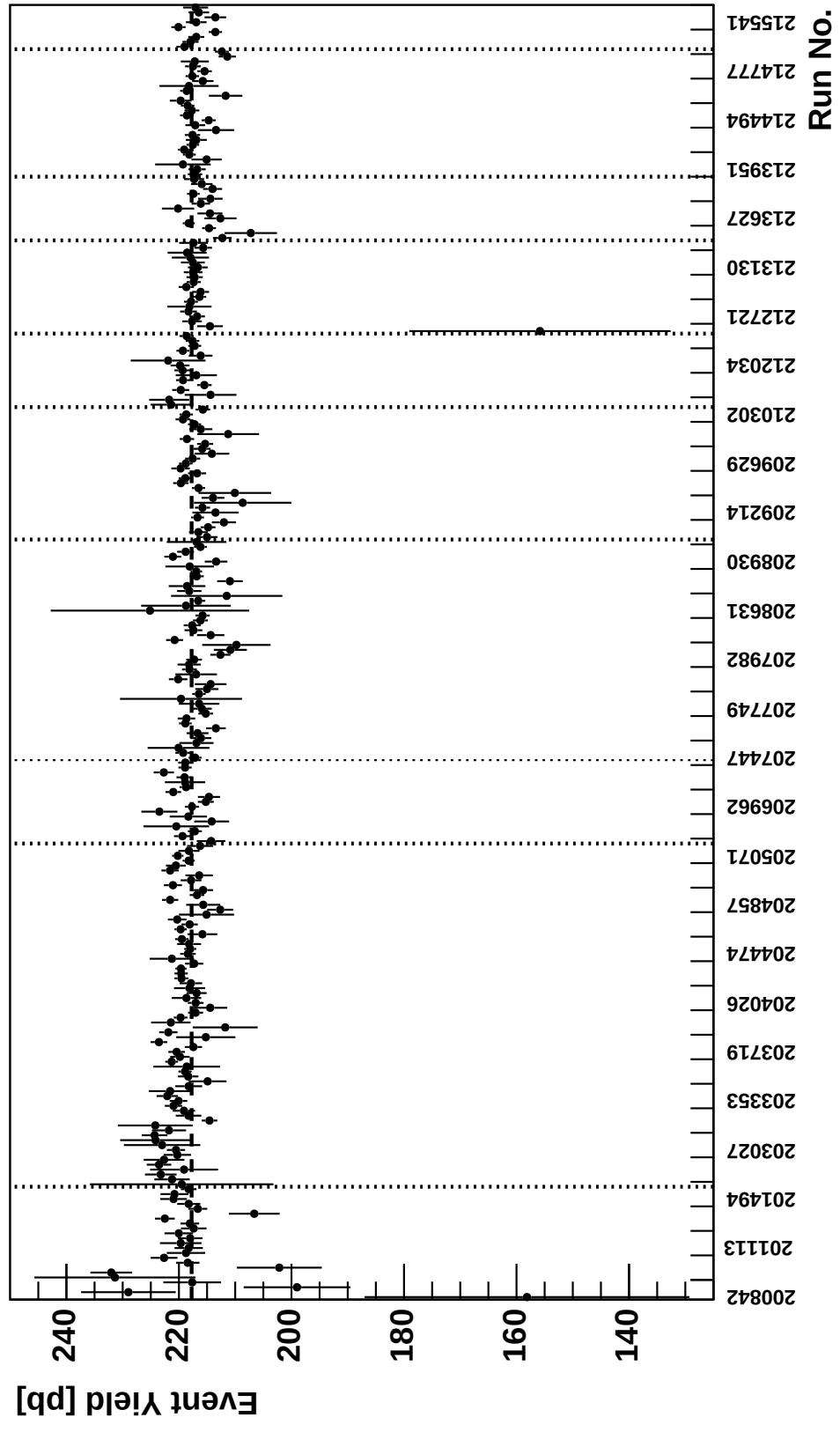

Figure 6.1: Events per unit of integrated luminosity for each individual data taking run. Run numbers are shown for every tenth run, vertical lines indicate the different run periods and the horizontal line corresponds to the fitted average event yield of $217.75 \pm 0.10\,\mathrm{pb}$.

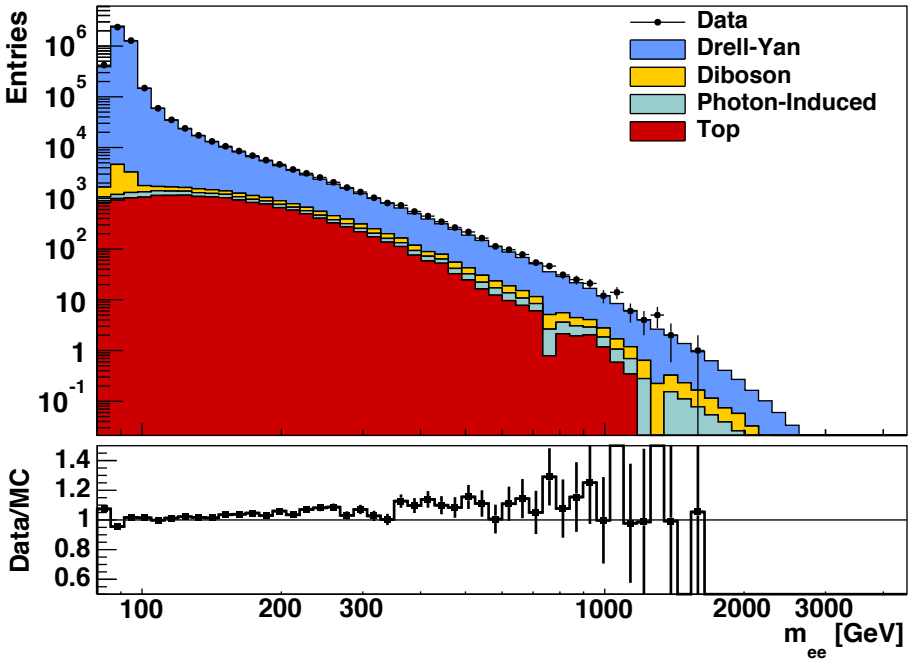

Figure 6.2: Initial Data/MC comparison of the invariant mass spectrum of all electron pairs passing the selection.

6.3 Initial Data-Monte Carlo Comparisons

The event and electron selection above is applied to the full data set and the Monte Carlo samples, resulting in an initial comparison of data and Monte Carlo, as seen in figures 6.2, 6.3, 6.4 and 6.5. It is immediately obvious that the distributions predicted by Monte Carlo and seen in data differ as figure 6.2 and 6.3 show an excess amount of data events slowly increasing with the invariant mass of the candidate event (and the associated increase in p_T of the electron candidates), hinting at an additional contribution. This will be further studied in chapter 7. Figure 6.4 also shows a large mismatch for the modelling of the crack region $1.37 < |\eta| < 1.52$. However, figure 6.5 shows good agreement in ϕ, a spectrum that is expected to be symmetric (as there is no ϕ dependence in the experimental setup) and effectively integrates over all masses here. This suggests that the overall number of events is close to the expected number and that there are no ϕ-dependent effects.

Furthermore, figures 6.6, 6.7 and 6.8 show the kinematic variables $\Delta\eta, \Delta\phi$ and ΔR describing the opening angle between the leading and subleading electron candidates (see chapter 3.1). Unlike the previous plots, which solely characterise individual electron

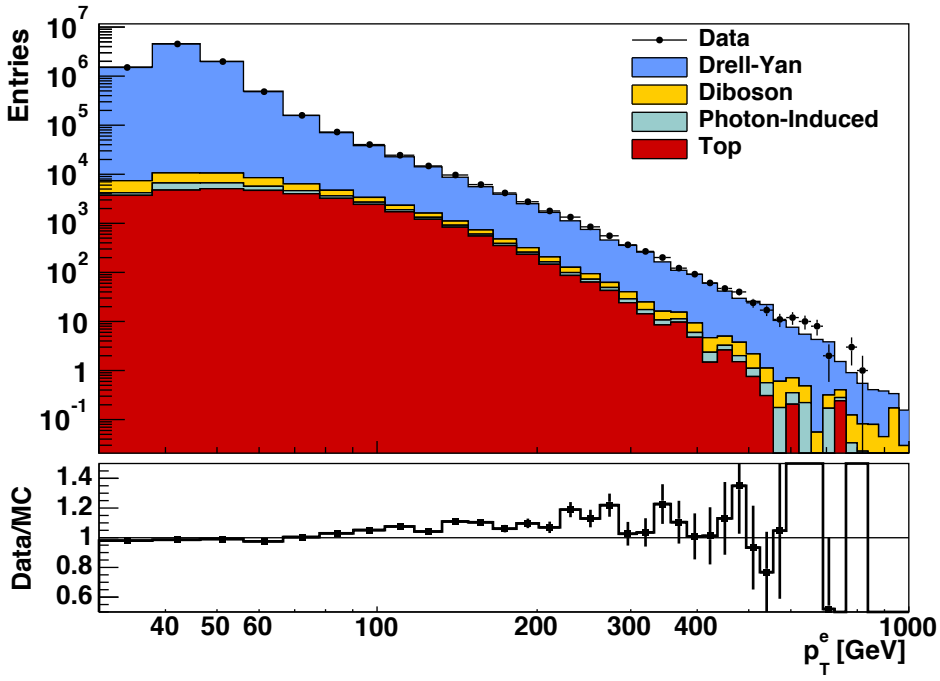

Figure 6.3: Initial Data/MC comparison of the p_T spectrum of all electrons passing the selection.

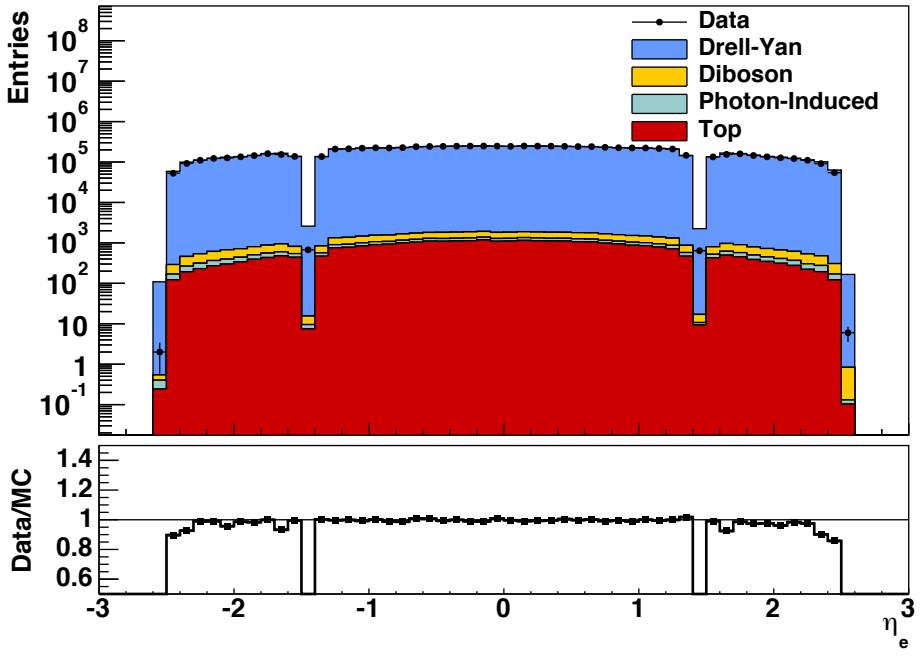

Figure 6.4: Initial Data/MC comparison of the η spectrum of all electrons passing the selection.

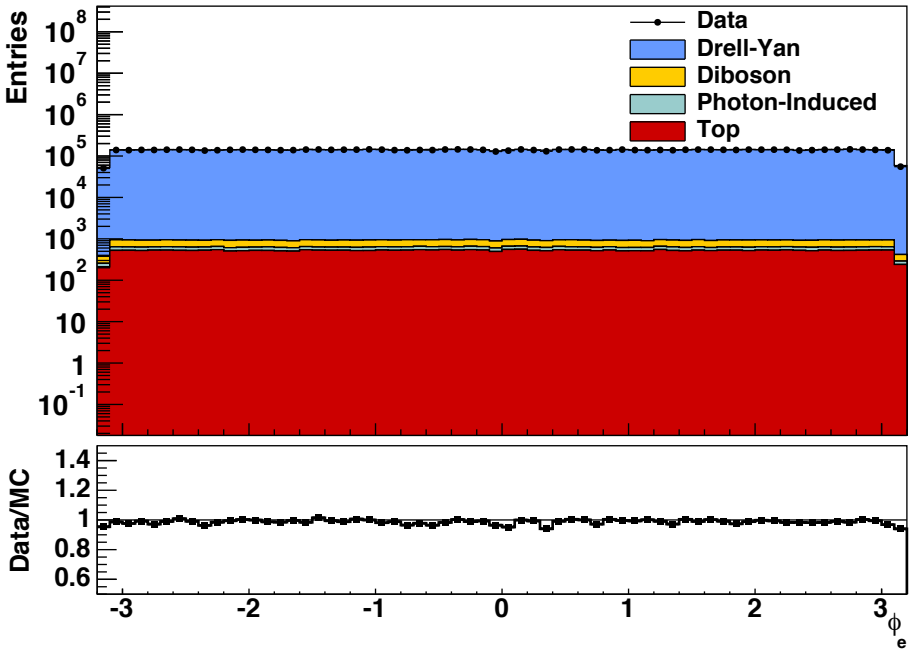

Figure 6.5: Initial Data/MC comparison of the ϕ spectrum of all electrons passing the selection.

candidates, these variables characterise the kinematics of the electron pair and hence the production of the electron pair. Here, $\Delta\eta$, and to a lesser extent ΔR, show shape discrepancies between the Monte Carlo samples and the data. This implies that the Monte Carlo simulation samples alone are not including all types of events producing di-electron pairs. This will be further explored in chapter 7.

6.4 Pile-up Reweighting

Pile-Up Reweighting:[5] The high bunch crossing rate of the LHC and the use of protons in densely packed bunches can lead to multiple proton interactions in a single given bunch crossing. These additional interactions are called "pile-up" and the number of interactions is given as $\langle\mu\rangle$, the average number of interactions per bunch crossing in a luminosity block. Pile-up has a visible effect in the data as the extra interactions in a given bunch crossing can produce particles leaving tracks and depositing energy (in-time pile-up). Additionally, pile-up events can cause energy deposition in the calorimeters that cannot be associated with a particular bunch crossing, as the time resolution of the calorimetry is lower than the bunch crossing rate (out-of-time pile-up). The Monte

[5]Using PileupReweighting-00-02-11.

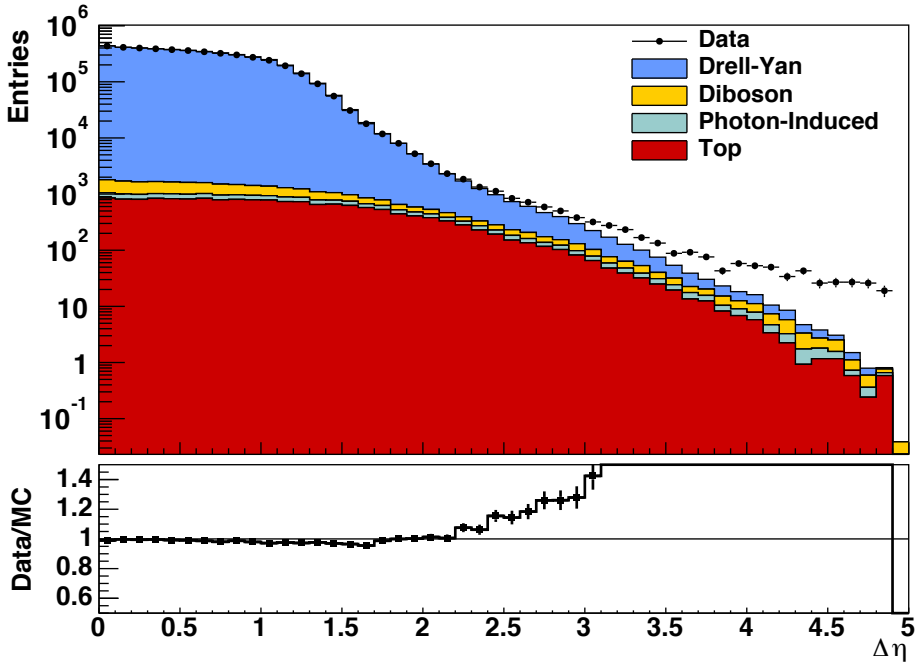

Figure 6.6: Initial Data/MC comparison of the $\Delta\eta$ between the electron pair forming the candidate event.

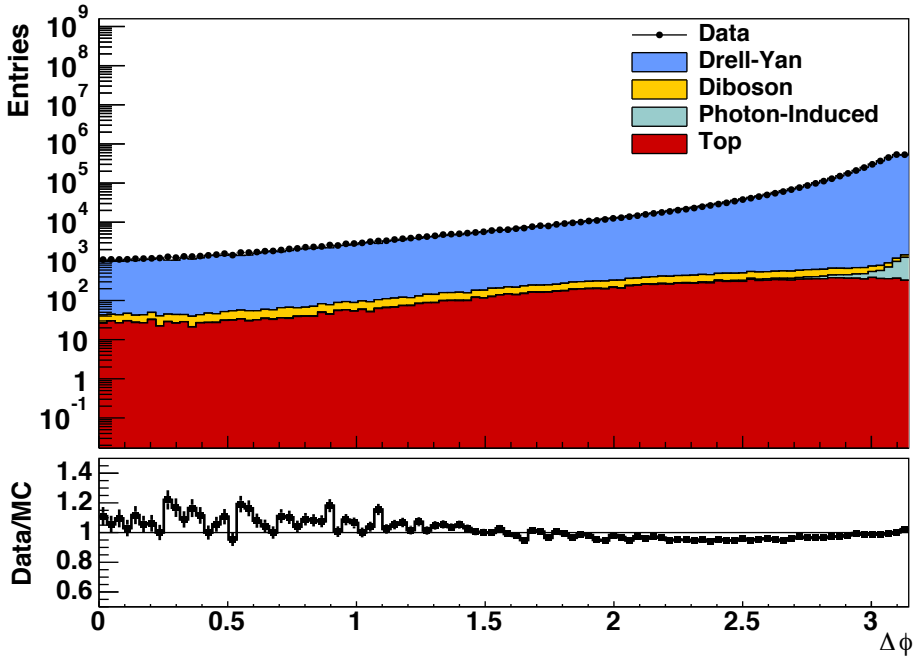

Figure 6.7: Initial Data/MC comparison of the $\Delta\phi$ between the electron pair forming the candidate event.

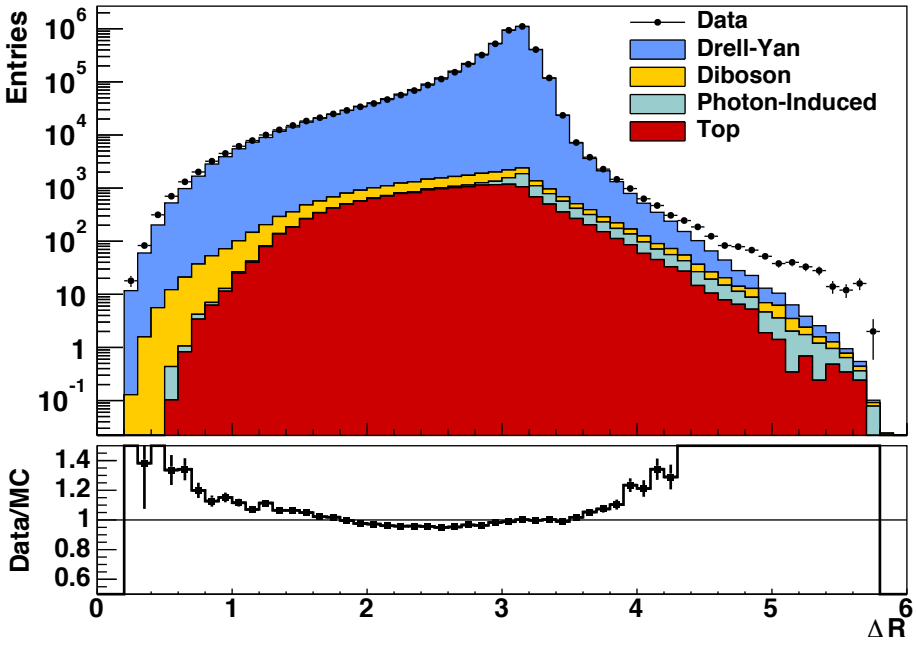

Figure 6.8: Initial Data/MC comparison of the ΔR between the electron pair forming the candidate event.

Carlo samples are enriched with pile-up events with a flat distribution of $\langle\mu\rangle$ around the expected $\langle\mu\rangle$ values in order to simulate this effect [111]. The $\langle\mu\rangle$ distribution in the Monte Carlo does not match the $\langle\mu\rangle$ distribution in data, as the actual distribution in data can only be measured during data taking. The pile-up reweighting (PRW) corrects the flat generic $\langle\mu\rangle$ distribution in the Monte Carlo to the real distribution measured in data. Figure 6.9 shows the flat $\langle\mu\rangle$ distribution in the Monte Carlo sample after the full event selection and the data distribution peaking between 15 and 20 and the result of the applied reweighting, leading to a better $\langle\mu\rangle$ description in the Monte Carlo, especially in the region between 15 and 30 where the majority of events lie.

6.5 Data-based Monte Carlo Corrections

The Monte Carlo samples do not take into account all effects present in data, especially those dependent on the running and beam conditions as these can only be determined during data-taking. Similarly, effects due to detector damage, inadequate modelling of the detector in the Monte Carlo and other problems causing discrepancies are not included. In order to compensate for the differences between the assumptions in the

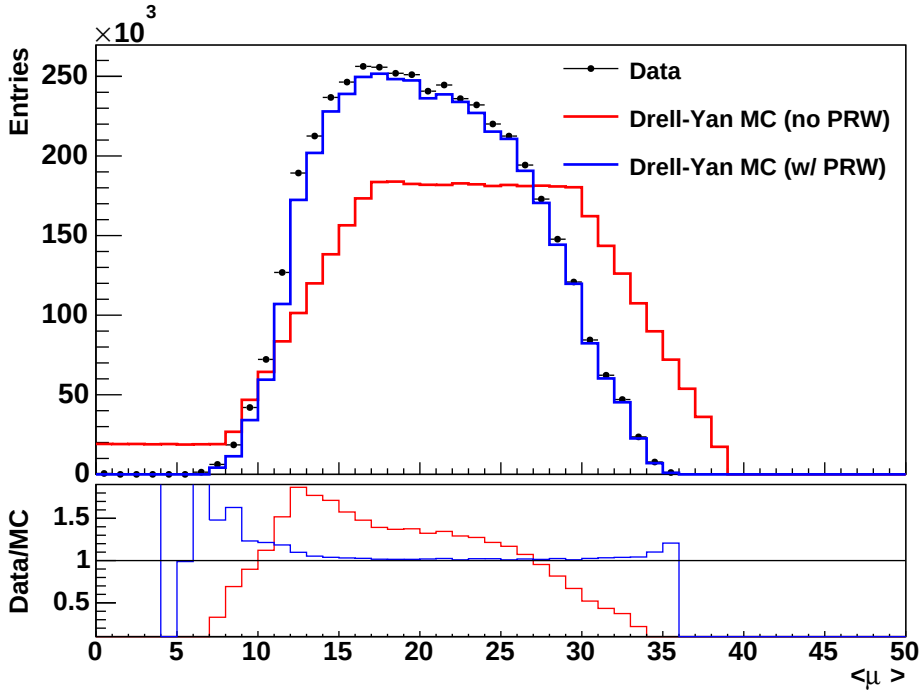

Figure 6.9: $\langle\mu\rangle$ distribution in data and the Drell-Yan Monte Carlo after the full event selection, showing the different $\langle\mu\rangle$ distribution in the unreweighted Monte Carlo and data and the effect of the pileup reweighting procedure.

Monte Carlo generation and the actual data distributions, several corrections are applied to the Monte Carlo:

Electron Energy Calibration:[6] The energy calibration in the detector is derived by the ATLAS electron performance group using Z candidates, as the resonance provides a fixed point to calibrate against. The calibration yields a scaling factor dependent on the η-location in the calorimeter. As this is a calibration of the data, the energy scaling is applied to the electron candidates found in the recorded data. The systematic uncertainty on the calibration, however, is obtained by varying the Monte Carlo energy scale, resulting in the systematic uncertainty in figure 6.10.

Electron Energy Resolution:[7] Resolution and detector effects result in a smearing effect of the recorded electron energy compared to the actual energy of the electron. The energy resolution is determined by the electron performance group during the run, using the width of the Z peak found in the data and the Monte Carlo. As the Monte Carlo is generated with minimal resolution effects, resolution effects can be added afterwards by smearing the electron energy randomly as determined by a Gaussian describing the

[6] Using egammaAnalysisUtils-00-04-58.
[7] Using egammaAnalysisUtils-00-04-58.

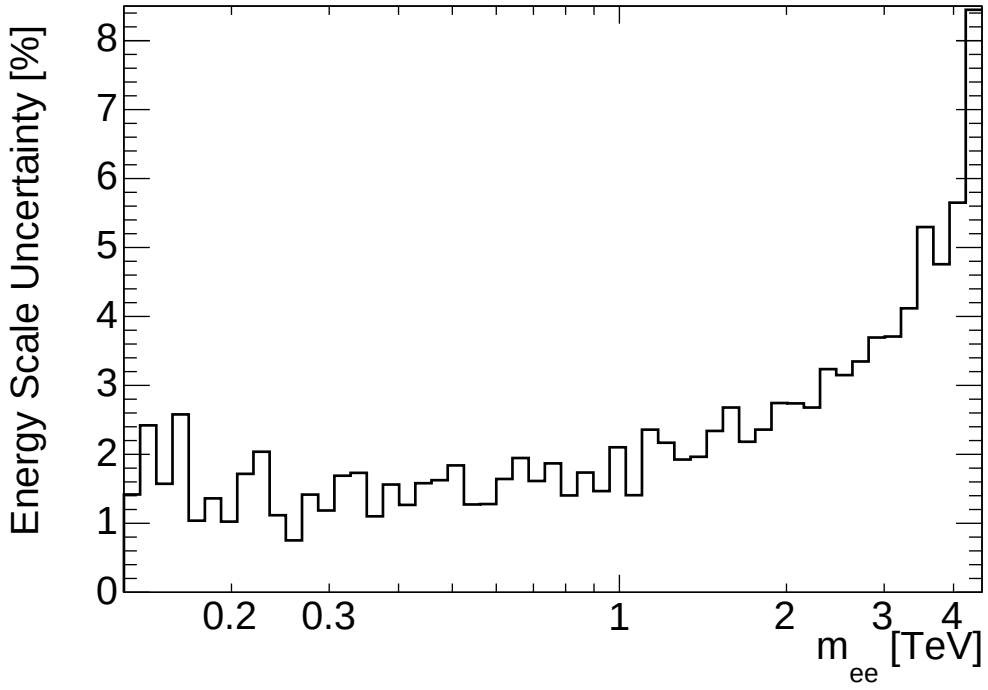

Figure 6.10: Systematic uncertainty on the di-electron mass due to the energy scale uncertainty in percent.

resolution. The resolution smearing also introduces a systematic uncertainty which is determined by varying the smearing effect by $\pm 1\sigma$ in size, resulting in the uncertainty shown in figure 6.11.

Efficiency Corrections:[8] The electron identification and reconstruction efficiency as simulated in the Monte Carlo samples differs from the efficiencies determined in data using tag-and-probe methods as detailed in [81] and shown in figure 3.10 and 3.11. This is due to the imperfect detector description in the Monte Carlo. In order to correct this, the efficiencies in data and Monte Carlo are compared by using the tag-and-probe method in both cases. The ratio of data to Monte Carlo is then used to derive scale factors binned in E_T and η which are then applied to the Monte Carlo samples. Additionally, the identification and reconstruction scale factors also provide a systematic uncertainty. The uncertainty for both scale factors added in quadrature is plotted in figure 6.12, which shows that even the combined uncertainty is small ($< 3\%$).

Reweighting of the z-vertex Position:[9] The primary vertex of the event is distributed in a Gaussian shape around $z = 0\,\text{mm}$. Since the exact position of the

[8] Using ElectronEfficiencyCorrection-00-00-34.
[9] Using egammaAnalysisUtils-00-04-58

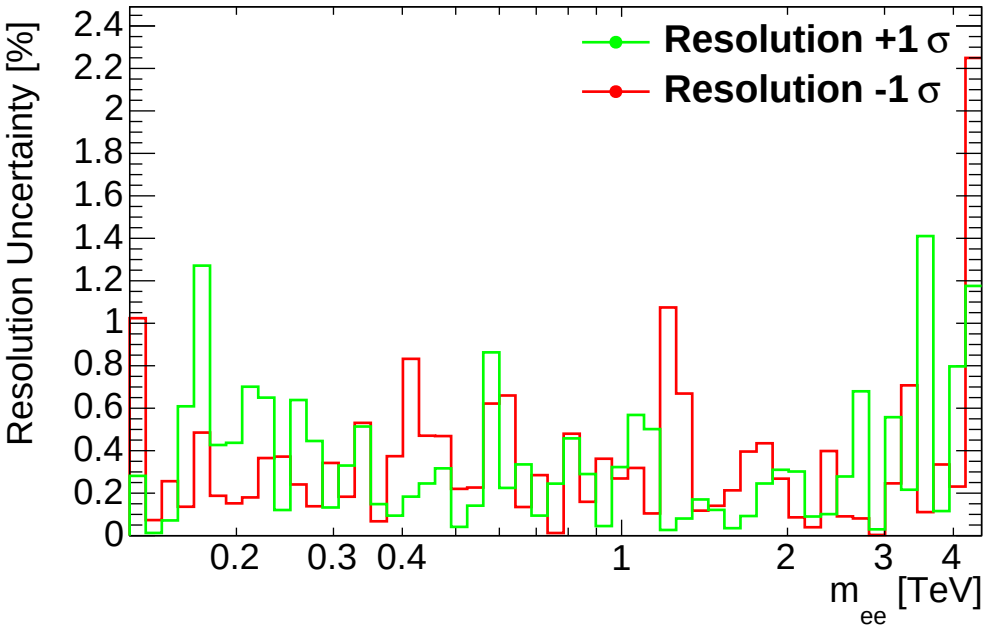

Figure 6.11: Systematic uncertainty on m_{ee} associated with the calorimeter energy resolution obtained by varying the smearing effect by $\pm 1\sigma$ (indicated in red and green, respectively).

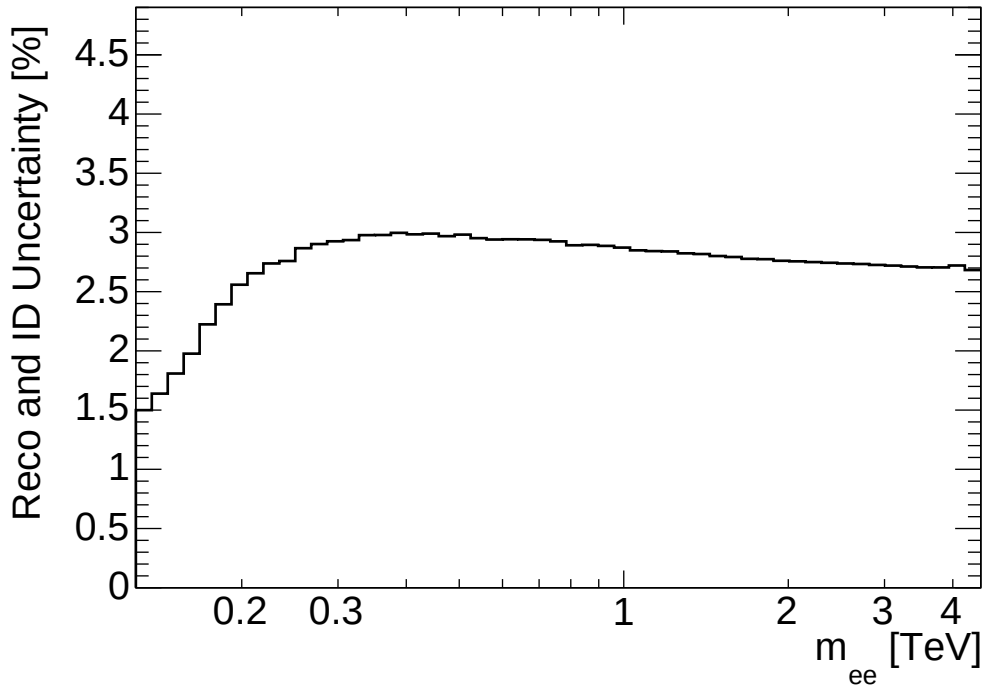

Figure 6.12: Combined systematic uncertainty of the *medium* identification and reconstruction scale factors in percent.

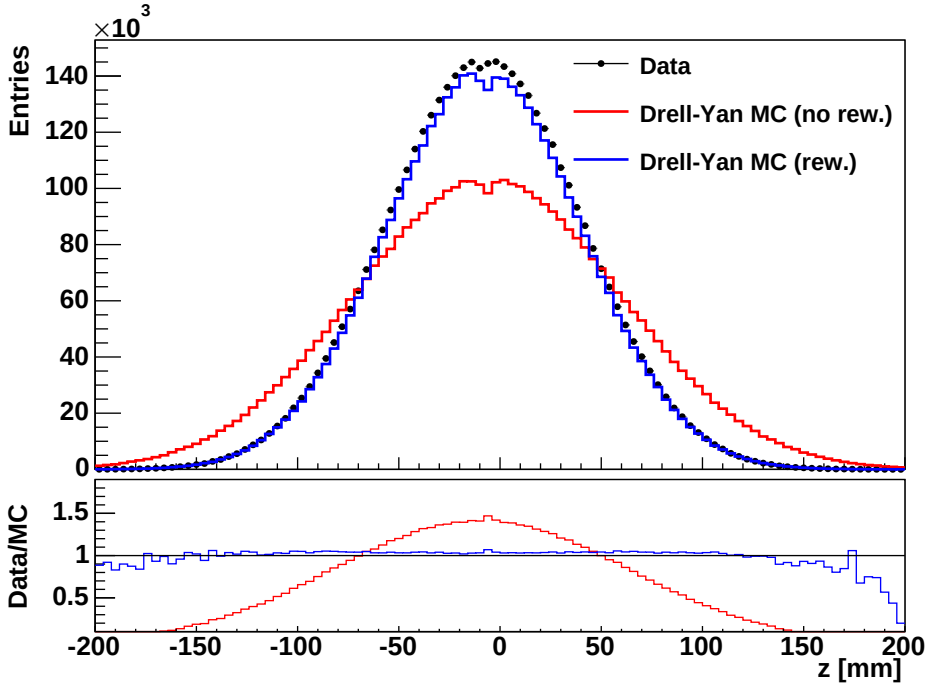

Figure 6.13: Distribution of vertex positions pn the z-axis, showing the width difference between the POWHEG Drell-Yan Monte Carlo and data after the full event selection with and without the z-vertex reweighing procedure.

primary vertex depends on the point where the beams cross, this is dependent on the running conditions. In the Monte Carlo, the width of the distribution is an input for the simulation, leading to a discrepancy between the simulation and the observed z-vertex distribution width. The z-vertex reweighting corrects the discrepancy and yields the expected distribution, as shown in figure 6.13, with the wider distribution in the uncorrected Monte Carlo sample (65 mm) and the narrower vertex distribution in the data and corrected Monte Carlo sample (48 mm).

Isolation Shift: The E_T^{C20} spectrum of Monte Carlo and data differs in the position of the peak. By measuring the average of the E_T^{C20} distribution in Monte Carlo and data, an offset is derived that is then applied to the Monte Carlo to correct for the different isolation. The offset was determined to be 385 MeV for the leading electron and 362 MeV for the sub-leading electron and is applied as a correction to the Monte Carlo as shown in figure 6.14.

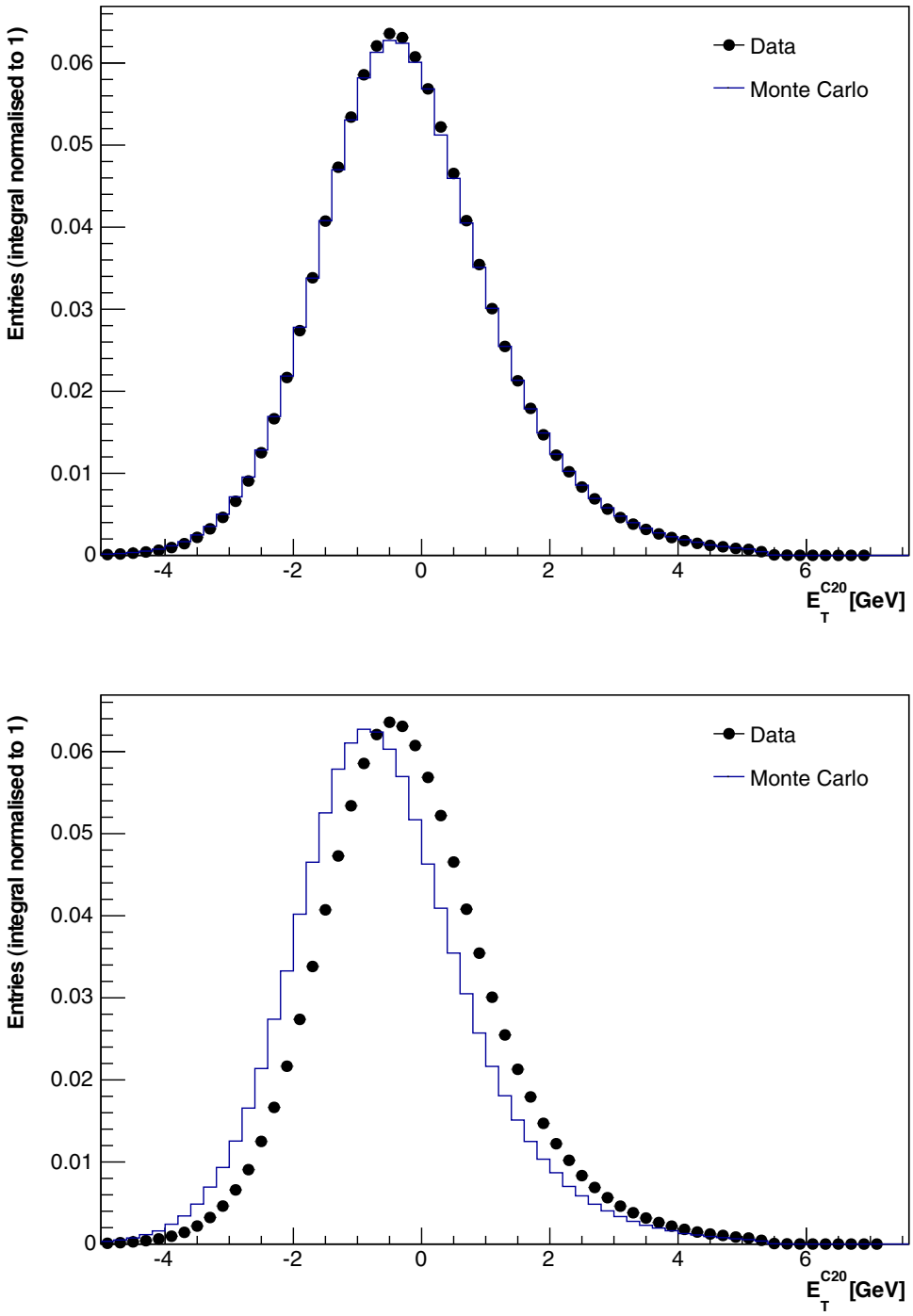

Figure 6.14: *Top*: Data and Monte Carlo in the E_T^{C20} spectrum for the leading electron with offset correction. *Bottom*: Data and Monte Carlo for the leading electron in the E_T^{C20} spectrum without offset correction.

Chapter 7

Fake Electron Background

The search for new physics requires a thorough understanding of Standard Model processes. Monte Carlo samples are used to model Standard Model di-electron production processes as described in chapter 4. In addition, QCD processes can mimic the event topology of di-electron production, allowing the events to pass selection and become event candidates. This chapter describes the data-driven "ABCD" method used to quantify the impact of such events faking isolated electrons (7.1), the shape estimation process (7.2), subsequent normalisation (7.3) and determination of the systematic uncertainties associated with the background (7.4).

7.1 Data-Driven Background Estimation

"Fake electrons" are jets misidentified and reconstructed as electrons. Since multi-jet processes can produce jets in conjunction with isolated electrons, it is possible for multi-jet events to pass the event selection. Using a PYTHIA8 Monte Carlo sample modelling multi-jet events, it was found that out of about 30 million generated events, 15 passed the full di-electron selection. This low efficiency makes it impractical to describe the multi-jet background using Monte Carlo samples. As shown in figure 7.1, the jet cross-section is several orders of magnitude higher than the cross-section for the signal considered here, to which Standard Model processes such as diboson, Drell-Yan, photon-induced contribution and top production can be a significant contribution. Hence, multi-jet background must be estimated using data-driven techniques. This is done using the "ABCD" method, also called the two-dimensional sideband method, by using two independent selection criteria to split the data set into four distinct regions. The background shape is then extracted

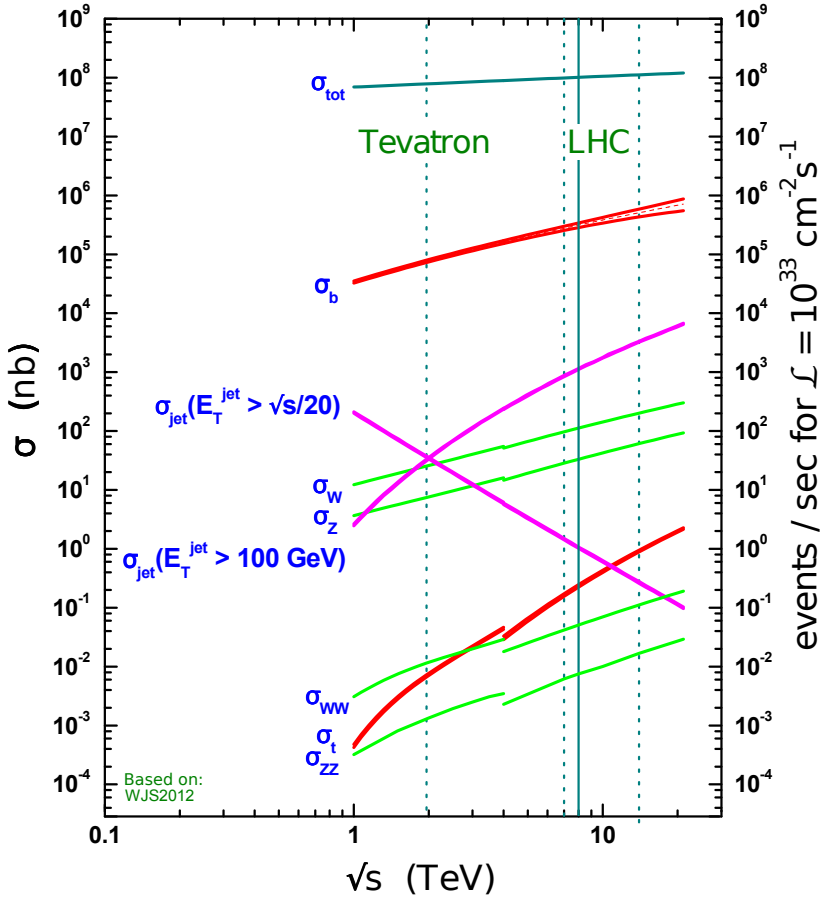

Figure 7.1: Proton-(anti)proton cross-section dependent on collider centre-of-mass. Of interest are the cross-sections σ_Z, σ_{WW}, σ_{ZZ}, and σ_t (Monte Carlo samples) compared to the σ_{jet} cross-section, which measured with a data-driven method at $\sqrt{s} = 8\,\text{TeV}$. The discontinuity at $\sqrt{s} = 4\,\text{TeV}$ is due to the switch from $p\bar{p}$ (TeVatron) to pp cross-section (LHC). Plot adapted from [112].

from one region and the other two regions are used to normalise the background shape to the expected number of events in the region of interest.

7.2 Background Shape Estimation

The background shape is determined by partially inverting the *isEM* identification criterion. Three variations of the selection inversion were tested: rejection of all *loose* or better electron candidates; rejection of electron candidates identified as *medium* or better; and rejection of electron candidates with *medium* or better identification, but requiring

loose identification (i.e. all electron candidates exactly *loose*). The three variations were tested using the E_T^{C20} spectrum for event candidates with an invariant mass of $m_{ee} \geq 200$ GeV, avoiding the mass region dominated by the Z pole. This spectrum shows the transverse energy deposited in a $\Delta R < 0.2$ cone around the electron cluster (see section 6.2) which is sensitive to jet production. The comparison was done by scaling all Monte Carlo samples to the data luminosity. This displays a deficit in Monte Carlo events for the range $E_T^{\mathrm{C20}} \gtrsim 1$ GeV. All three background shape variations were then scaled to the size of the deficit between data and Monte Carlo and compared. It was found that the third variation (exactly *loose*) gave the best shape description, as shown in figure 7.2.

To avoid possible double counting of events, two further modifications were made to the background shape estimation procedure. First, a same charge requirement was imposed on the electron pair. Neutral current Drell-Yan events, the main SM process, contain electrons with an opposite charge, since the electrons are decay products of the Z/γ^*. By charge conservation, the overall charge of the decay products must be neutral. In contrast to this, fake electrons from QCD multi-jet events have no preferred charge configuration. Additionally, the partially inverted identification and same charge selection is also applied to the Monte Carlo samples and then subtracted from the background shape derived from data. Doing so prevents possible double-counting of processes already modelled by the Monte Carlo.

7.3 Background Normalisation

The second step of the background estimation is normalising the shape determined in the previous section to the number of background events expected in the full selection. This is done by inverting another selection criterion, splitting the data set into four distinct regions, which are usually labelled A, B, C and D and give the method the name “ABCD" method.

The first inverted selection criterion is the partially inverted identification, carried over from the shape determination. The second inverted selection is the electron isolation. The electron identification uses track data and the shower shape within a 5×7 cell cluster of the calorimeter, where *loose* and *medium* identifications differ in the stringency of the shower shape requirements. The electron isolation excludes the central 5×7 cell cluster used for identification and uses the total transverse energy deposition within a

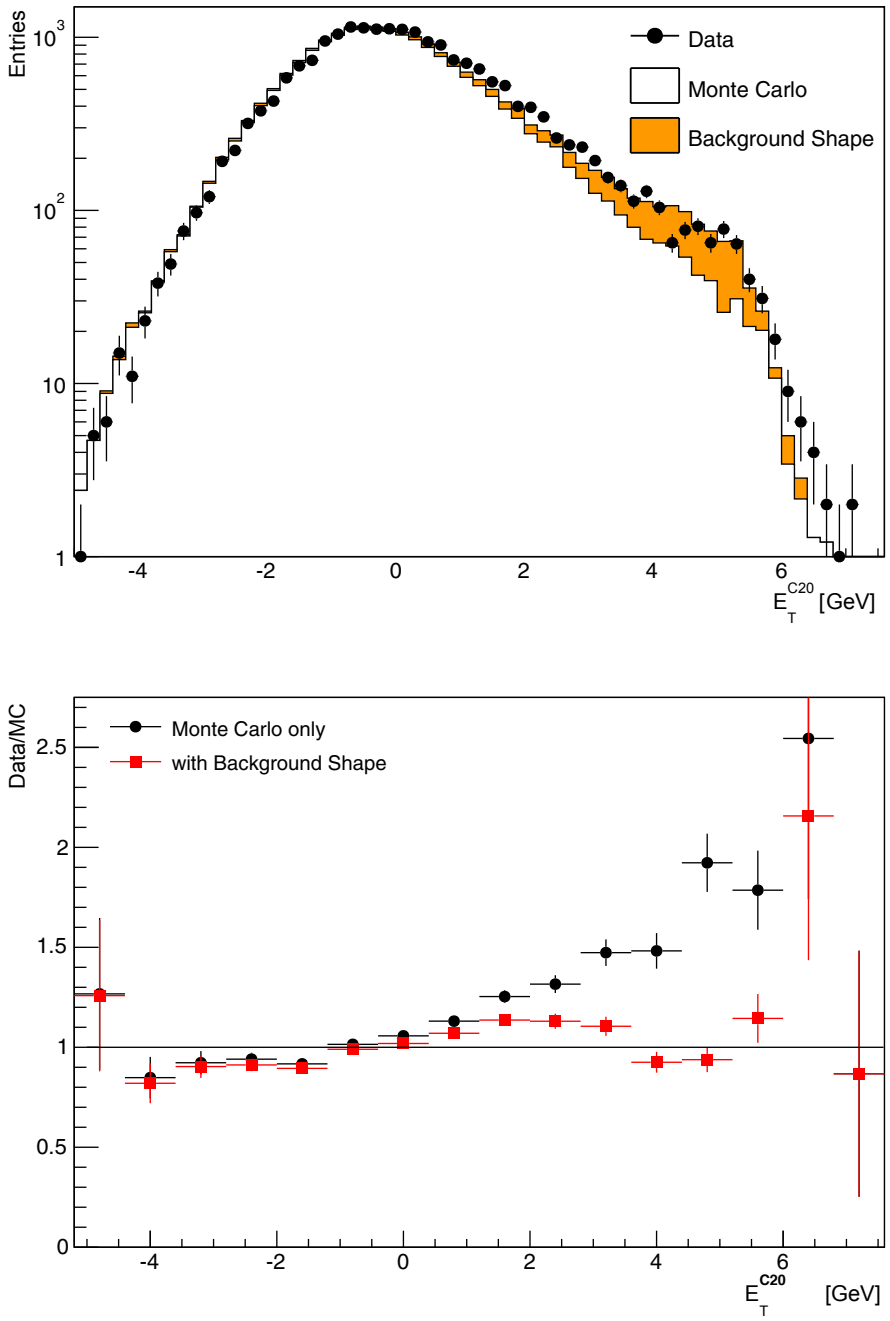

Figure 7.2: E_T^{C20} shape comparison for data, Monte Carlo and background shape for events with $m_{ee} \geq 200$ GeV. Monte Carlo is scaled to the data luminosity. Background shape is scaled to the discrepancy between the data and Monte Carlo integral.

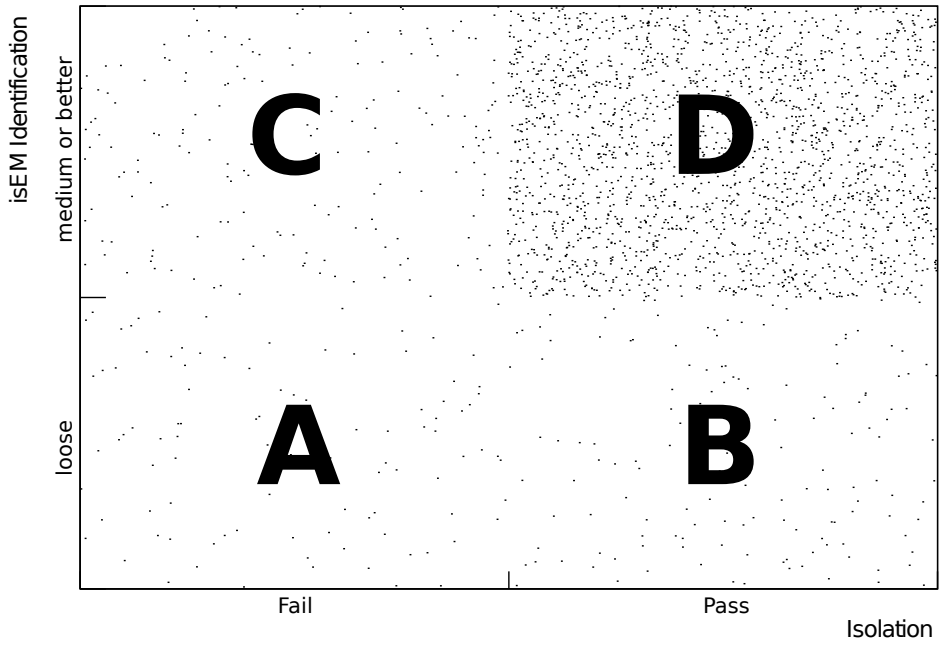

Figure 7.3: ABCD regions formed by the selection requirements. On the x-axis, the sample is split into events that either fail or pass the isolation requirement, while the y-axis is split into identification criteria *loose* and *medium* or better. The region requirements are exclusive, so there is no overlap in events for the different regions. The fill density is proportional to the number of event candidates found in each region.

cone around the electron cluster (see chapter 6: $E_T^{\mathrm{C20}} \leq 0.007E_T + 5$ GeV for the leading and $E_T^{\mathrm{C20}} \leq 0.022E_T + 6$ GeV for the subleading electron).

This pair of inverted selection criteria spans a plane as shown in figure 7.3. Region A contains all events with a pair of same charge *loose* electrons with at least one failing isolation. Region B consists of all pairs of same charge *loose* electrons passing the isolation requirement and corresponds to the region from which the background shape is extracted. Region C contains *medium* or better electron pairs with at least one failing isolation. Region D corresponds to the nominal data selection, namely all pairs of *medium* or better electrons passing the isolation requirement, and is dominated by neutral current Drell-Yan events (as the selection was optimised to select for such events). As with the shape estimation, the Monte Carlo contribution is subtracted to avoid double-counting effects.

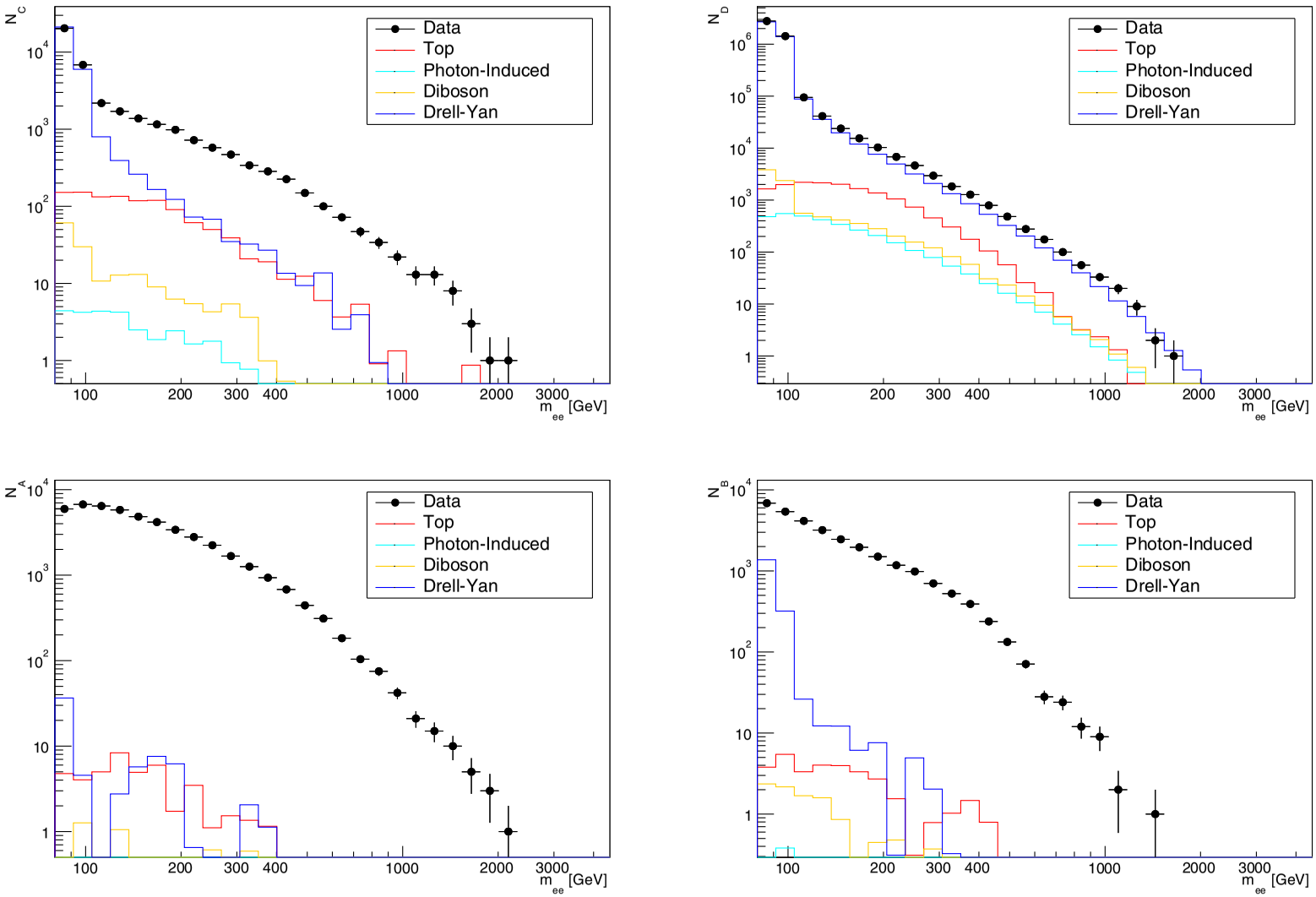

Figure 7.4: Distribution of event candidates found in data for each ABCD region before Monte Carlo subtraction. Monte Carlo distributions are overlaid for comparison. *Top left*: region C, *top right*: region D, *bottom left*: region A, *bottom right*: region B.

In order to normalise the amount of fake electron background events, the regions A, B and C must be used to infer the number of events within D. Since the selection criteria used to span the regions are independent, the ratio of events in region D to region B must be the same as the ratio of events in region C to region A, i.e. $N_D/N_B = N_C/N_A$. Therefore the number of background events in region D is $N_D = N_C/N_A * N_B$, where N_B corresponds to the background shape, as shown in table 7.1. Using this background estimate and the number of events found in each invariant mass bin for the background shape, a background scaling factor is derived.

The background scaling factor is then fitted over the invariant mass range with a polynomial, parametrising the background scaling factor in the form

$$s_{bkg} = p_0 + p_1 \log m_{ee} + p_2(\log m_{ee})^2 + p_3(\log m_{ee})^3. \tag{7.1}$$

To avoid influences from the Z peak region, the fit is performed in the region of 100 GeV $\leq m_{ee} \leq$ 5000 GeV, as seen in figure 7.5, showing the mass bins, the associated scaling factor as well as the polynomial fit with fit parameters $p_0 = -2.101 \pm 0.018$, $p_1 = 1.408 \pm 0.005$, $p_2 = -0.288 \pm 0.001$, $p_3 = 0.0200 \pm 0.000$ and a goodness of fit of $\chi/N_{d.o.f.} = 6.945/6 = 1.16$.

The background scaling factor s_{bkg} is then applied to the background shape to produce the full data-driven estimate of the background.

7.4 Systematic Uncertainty

The first systematic uncertainty stems from the application of the fitted scaling factor to the background shape. The background shape with the scaling factor applied was taken as the nominal value and was then compared to the values derived from the background normalisation. The difference between those was taken as the systematic uncertainty due to the scaling factor application, as shown in table 7.2. The second systematic uncertainty of the fake electron background is dependent on the requirements used to derive the background normalisation. This uncertainty is estimated by studying the difference between the data and the Monte Carlo distribution of the E_T^{C20} spectra, as data and Monte Carlo exhibit a distinct offset in the peak position. As shown in figure 6.14, the offset is usually corrected by shifting the peak position. By repeating the background normalisation procedure without the correction to the peak position, the

Table 7.1: Monte Carlo-subtracted number of events in the regions A, B and C and background estimate derived as described in the text.

ABCD Region	Invariant Mass m_{ee} [GeV]									
	100-110	110-130	130-150	150-200	200-250	250-300	300-400	400-800	800-1200	1200-5000
Region A	3353 ± 58	5223 ± 72	3603 ± 60	5638 ± 76	2892 ± 54	1569 ± 40	1535 ± 39	1040 ± 32	54.90 ± 7.42	8.000 ± 2.828
Region B	3210 ± 58	4564 ± 68	2843 ± 54	3902 ± 63	1961 ± 45	1028 ± 33	1006 ± 32	501.2 ± 22.4	22.00 ± 4.69	0.999 ± 1.000
Region C	709.9 ± 48.2	1138 ± 35	857.8 ± 18.9	1276 ± 20	695.9 ± 13.2	424.2 ± 7.1	412.2 ± 9.5	353.4 ± 8.6	30.95 ± 0.86	7.242 ± 0.433
Bkg Est	679.8 ± 49.2	994.8 ±37.2	676.7 ± 22.7	882.9 ± 18.7	471.8 ± 16.5	278.1 ± 12.2	270.0 ± 12.6	170.3 ± 10.2	12.40 ± 3.15	0.905 ± 0.962

Table 7.2: Estimated number of background events using the ABCD method across the studied mass range. Numbers are shown with statistical, scaling factor, isolation and total uncertainties.

Uncertainty	Invariant Mass m_{ee} [GeV]							
	80-110	110-150	150-200	200-300	300-400	400-800	800-1200	1200-3000
Statistical	2961 ± 210	1654 ±43	904.6 ±19.2	737.3 ±20.2	273.2 ± 12.8	156.9 ±9.4	9.71 ±2.47	0.590 ± 0.627
Scaling Factor	2961 ± 386	1654 ±18	904.6 ±21.7	737.3 ±12.6	273.2 ± 3.2	156.9 ±13.4	9.71 ±2.69	0.590 ± 0.315
Isolation	2961 ±1177	1654 ±86	904.6 ±74.1	737.3 ±89.5	273.2 ± 34.4	156.9 ±10.7	9.71 ±1.93	0.590 ± 0.023
Combined	2961 ±1257	1654 ±98	904.6 ±79.5	737.3 ±92.6	270.0 ± 36.8	156.9 ±19.5	9.71 ±4.13	0.590 ± 0.702

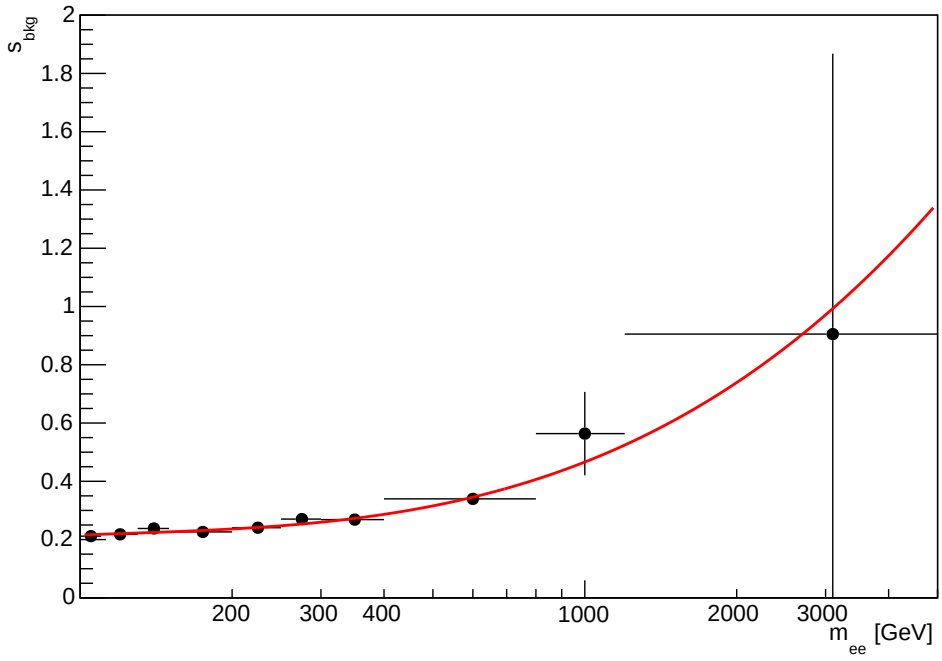

Figure 7.5: Background scale factor for $m_{ee} > 100$ GeV, showing mass-binned scaling factors and the derived fit, see text for the fitted function.

isolation uncertainty of the background estimate is determined, using the difference in the background estimate with and without the isolation correction, giving the results in table 7.2.

Finally, table 7.2 shows the combined uncertainties, obtained by adding the statistical and the systematic uncertainties in quadrature. Figure 7.6 shows a comparison of the size of the uncertainties, with the isolation uncertainty dominating the lower mass region and the statistical uncertainty the high mass region.

7.5 Background Extrapolation for Limit Setting

The fake electron background runs out of event candidates around 1 TeV, at around the same range as the data itself as it is a data-driven method. While sufficient for comparisons of data to Monte Carlo as will be shown in chapter 8, this statistical limitation becomes problematic later on for the limit setting procedure as the systematic uncertainties of the fake electron background grow large at high masses. To compensate for the lack of events, the fake electron background is extrapolated to higher masses

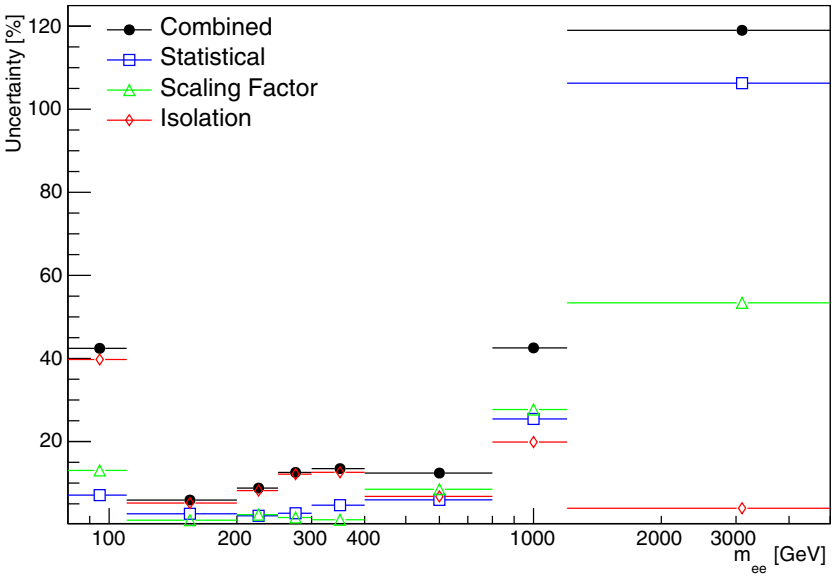

Figure 7.6: Comparison of the statistical, scaling factor and isolation uncertainties.

using an analytical function:

$$f_{di-jet}(x) = p_0 x^{p_1} x^{p_2 log(x)}, \tag{7.2}$$

which is a modified version of the *di-jet function* modelling di-jet events [113, 114] which was successfully used in previous versions of the Z' search [115] for extrapolating similar backgrounds. The di-jet function is fitted to the fake electron background in the range 0.2 TeV–0.5 TeV, resulting in the fit shown in figure 7.7. The parameters are $p_0 = 1.280 \pm 0.325$, $p_1 = -4.829 \pm 0.414$, $p_2 = -1.124 \pm 0.163$ with a goodness of fit of $\chi^2/n.d.f. = 15.75/14 = 1.125$. As seen in chapter 8, the fake electron background estimate works well especially before the systematic uncertainty becomes the dominant uncertainty (also see table 7.2), hence the extrapolation is only used for masses $m_{ee} >$ 0.4 TeV, allowing for overlap with the fit range. The statistical uncertainty on the extrapolated range is derived using the uncertainty of the fit and can be seen in figure 7.8.

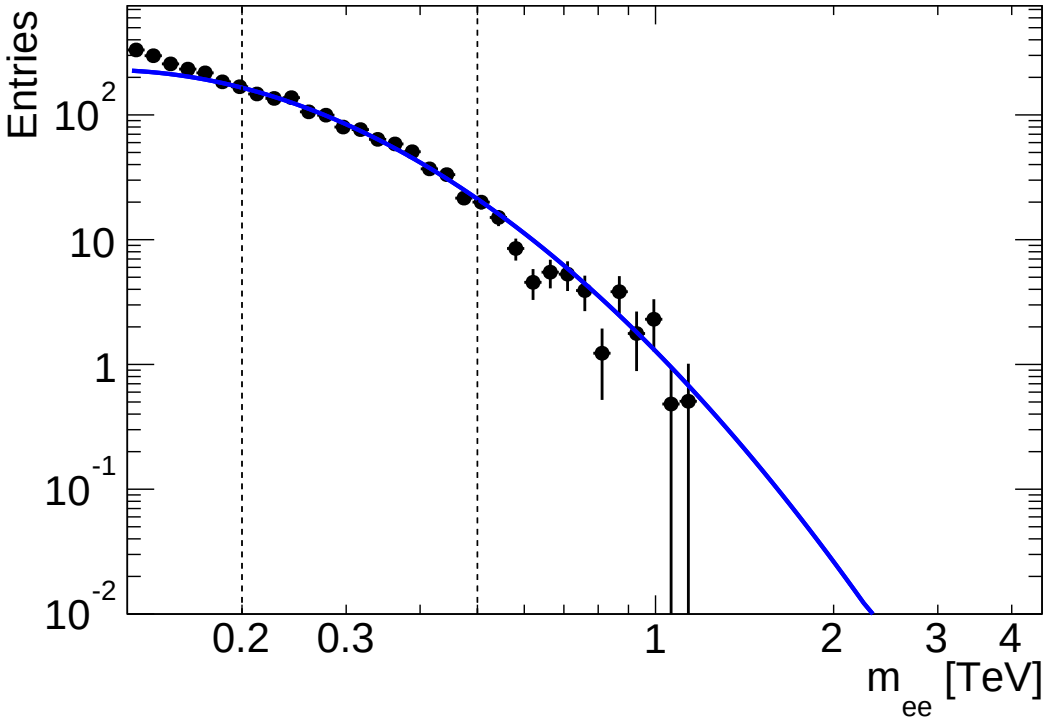

Figure 7.7: Di-jet fit to the fake electron background with the vertical dashed lines indicating the fit range.

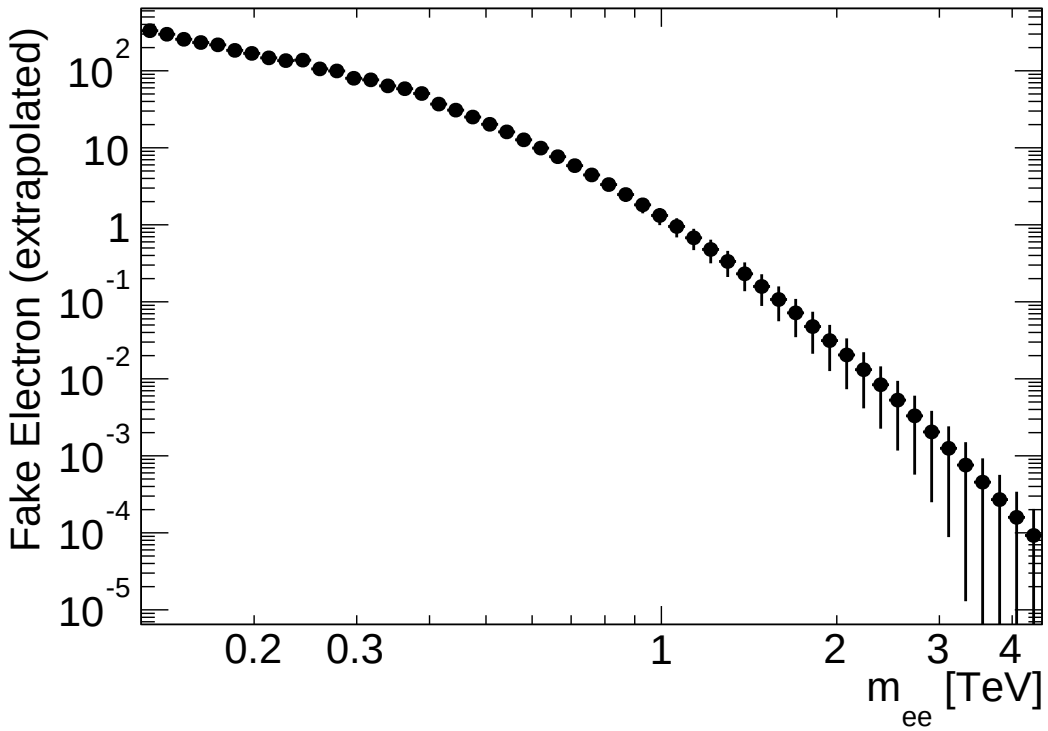

Figure 7.8: High mass extrapolation of the fake electron estimate in m_{ee}.

Chapter 8

Data-Monte Carlo Comparisons

In this chapter, the results of the previous chapters are combined into an overall comparison between the experimental data and the SM expectation. The plots compare event candidates found in data after the full selection (see section 6.2) with the event candidates found in the Monte Carlo samples after full reconstruction and selection (see chapter 4), including all Monte Carlo corrections (see section 6.4 and 6.5), as well as the data-driven fake electron background estimation (see chapter 7). The comparisons are done for the entire mass range (section 8.1) and at high mass for event candidates with an invariant mass of $m_{ee} > 200\,\text{GeV}$ (section 8.2).

8.1 Comparisons for $m_{ee} > 70\,\text{GeV}$

First, a comparison of the full mass range is made. This includes all event candidates passing the selection as in section 6.2. Figures 8.1, 8.2, 8.3, 8.4 are similar to the initial comparisons between data and Monte Carlo in section 6.3. Unlike figures 6.2, 6.3, 6.4, and 6.5, however, the comparisons here take all Monte Carlo corrections into account as well as the fake electron background. Comparing figure 6.2 and figure 8.1, it becomes apparent that the broad excess in the region 100 GeV–1000 GeV is now accounted for by the fake electron background, bringing the Data/MC ratio much closer to 1.

The event candidates contributed by the SM processes are also listed in broad bins in table 8.1, giving an overview of the overall contribution of the individual sources. As can also be seen in figure 8.1, the Drell-Yan contribution is the largest source of event candidates across the entire mass range. The second highest contribution is from the

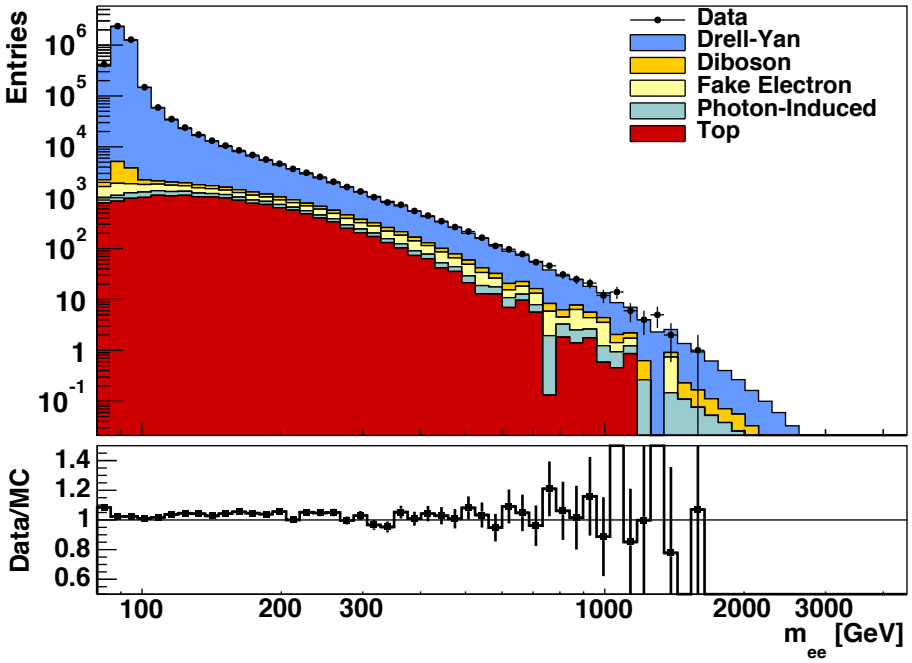

Figure 8.1: Data/MC comparison of the invariant mass spectrum of all event candidates passing all selection criteria.

diboson background in the Z peak bin (80 GeV–110 GeV), while the top background becomes the second highest contribution in the mass range 110 GeV–800 GeV.

Apart from the invariant mass, the previously compared variables are all associated with individual electron candidates. In order to describe each event candidate, it is necessary to use variables correlating the electron pair making up the event. In order to do so, three additional variables are compared, $\Delta\eta$, $\Delta\phi$ and ΔR, all three describing the opening angle between the electron pair in $\eta - \phi$ space (see equation 3.2 in section 3.1). Using these variables to characterise each event, the differences between the SM contributions become apparent, with the fake electron background contributing a large number of candidates in the high $\Delta\eta$-range, as shown in figure 8.5, and in the ΔR-distribution, as seen in figure 8.7. Similarly, the differences between the Drell-Yan and PI contributions described in section 4.3 become visible again in the same distributions, where the PI contribution exhibits a flat shape in $\Delta\eta$ and ΔR, whereas the Drell-Yan contribution tapers off rapidly in both distributions.

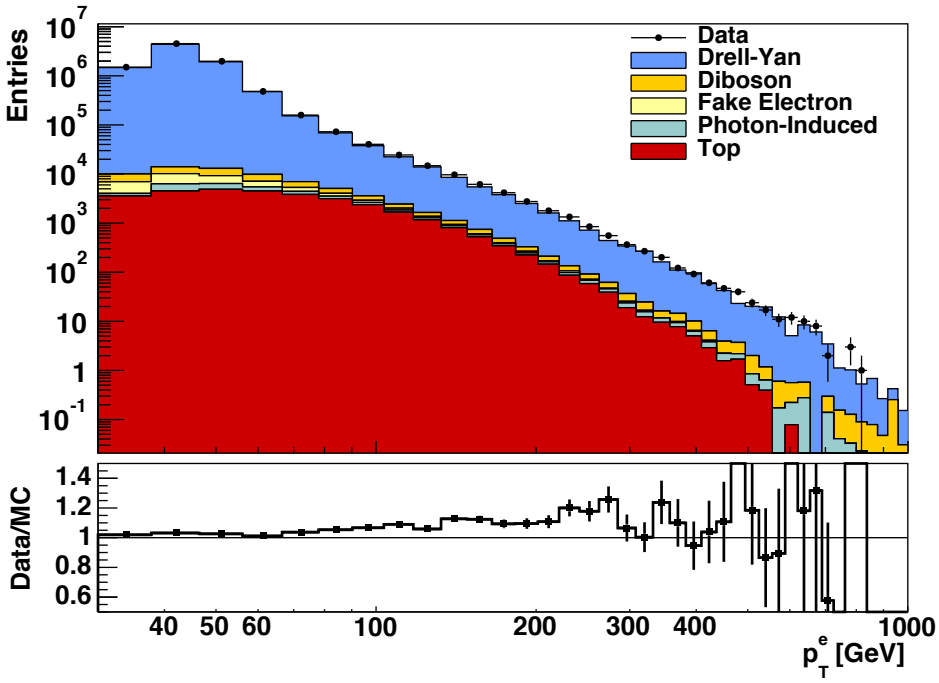

Figure 8.2: Data/MC comparison of the transverse momentum p_T spectrum of all electron candidates passing all selection criteria.

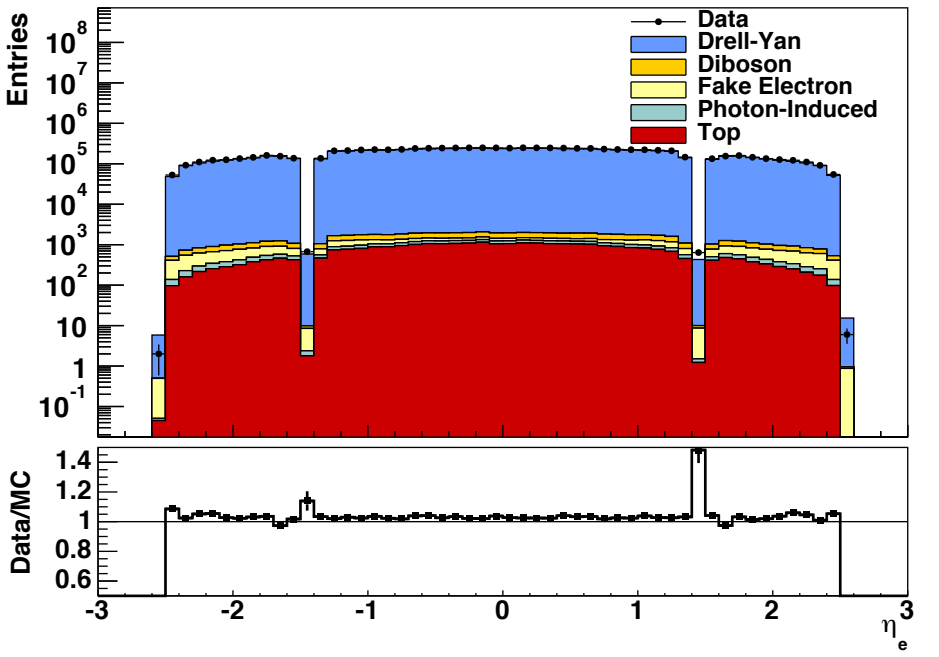

Figure 8.3: Data/MC comparison of the η spectrum of all electron candidates passing all selection criteria.

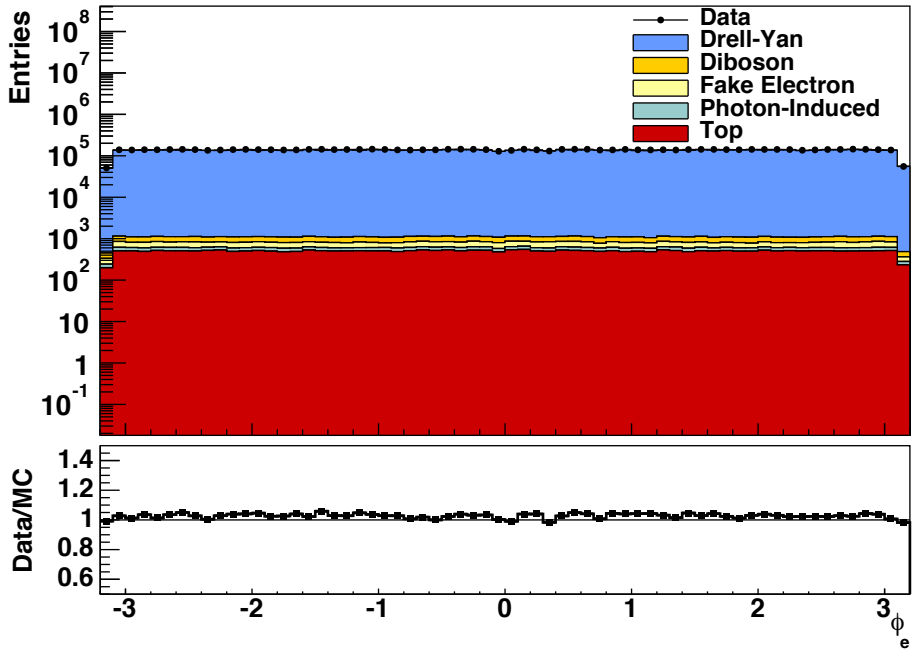

Figure 8.4: Data/MC comparison of the ϕ spectrum of all electron candidates passing all selection criteria.

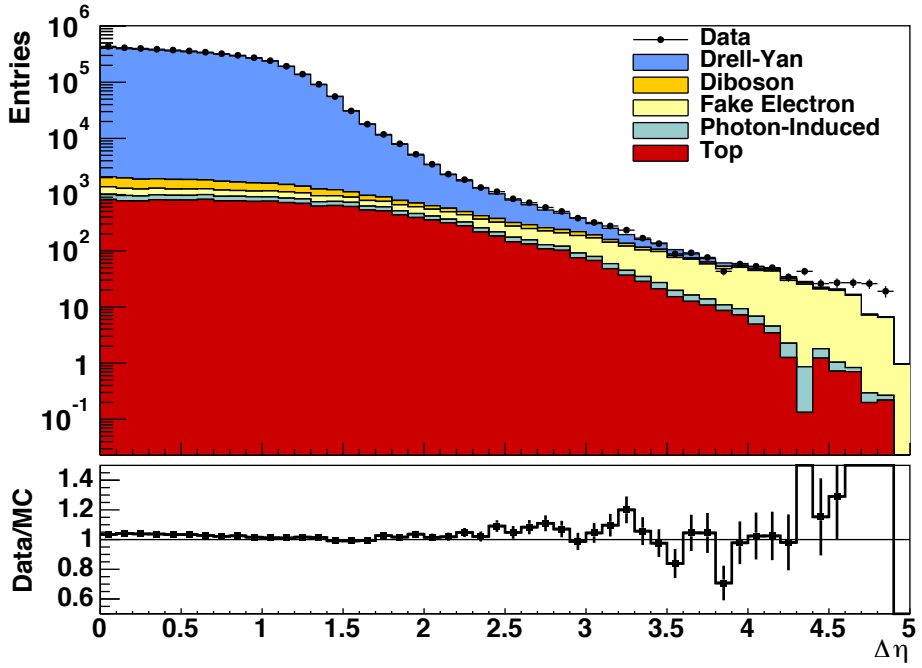

Figure 8.5: Data/MC comparison of the opening angle between the electron candidate pair in the η plane.

Table 8.1: Candidate events from all SM sources and comparison to data. All uncertainties indicated are statistical uncertainties.

Source	Invariant Mass m_{ee} [GeV]						
	80-110	110-200	200-400	400-800	800-1200	1200-3000	3000-5000
Drell-Yan	4127960 ± 3600	117330 ± 410	13523 ± 67	1271 ± 6	66.71 ± 0.25	9.459 ± 0.035	0.007147 ± 0.000032
Diboson	6423 ± 34	1828 ± 20	660.89 ± 12.08	84.28 ± 0.93	5.859 ± 0.206	1.030 ± 0.025	0.0003121 ± 0.000268
Fake Electrons	2961 ± 25	2558 ± 24	1010 ± 16	156.9 ± 7.0	9.714 ± 2.074	0.5895 ± 0.5896	0 ± 0
Photon-Induced	1221 ± 13	1501 ± 140	461.2 ± 2.8	63.67 ± 0.89	4.516 ± 0.062	0.8939 ± 0.0231	0.001975 ± 0.000034
Top	4446 ± 42	8380 ± 57	2924 ± 33	212.7 ± 9.4	6.553 ± 1.822	-0.5473 ± 0.5473	0 ± 0
Data	4258620 ± 2060	136201 ± 369	18994 ± 138	1862 ± 43	99 ± 10	9 ± 3	0 ± 0

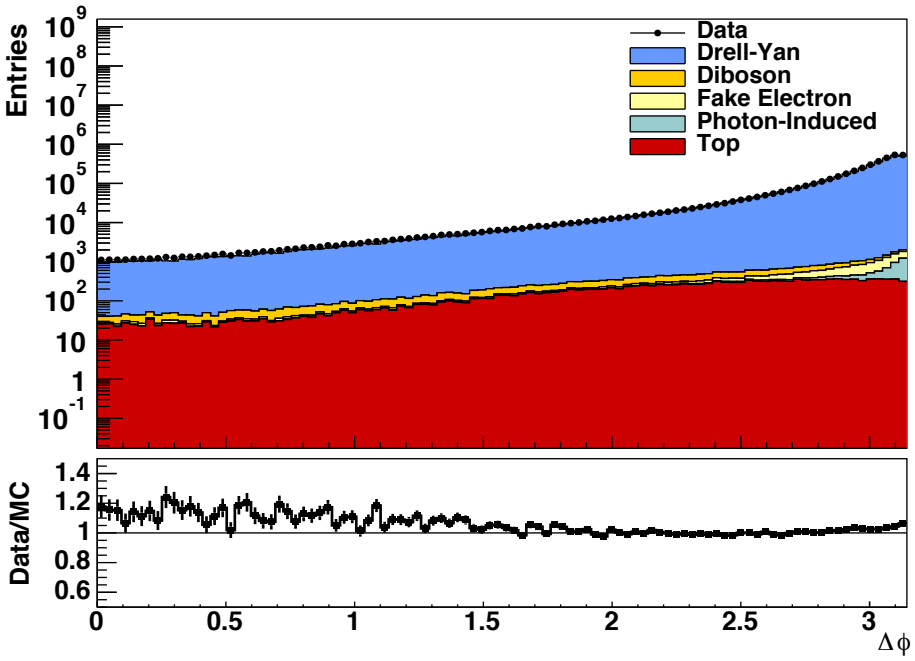

Figure 8.6: Data/MC comparison of the opening angle between the electron candidate pair in the ϕ plane.

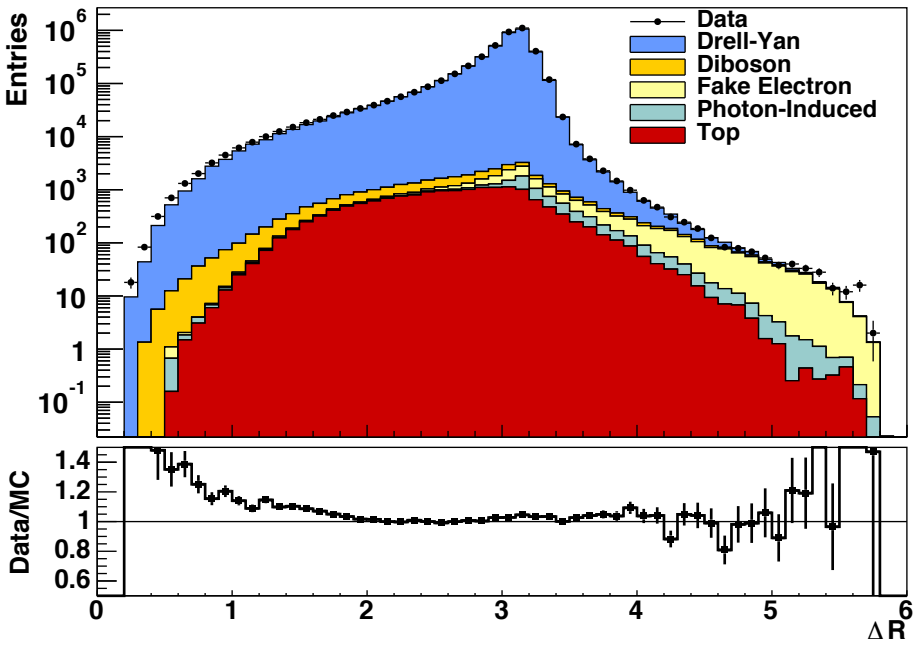

Figure 8.7: Data/MC comparison of the opening angle ΔR between the electron candidate pair.

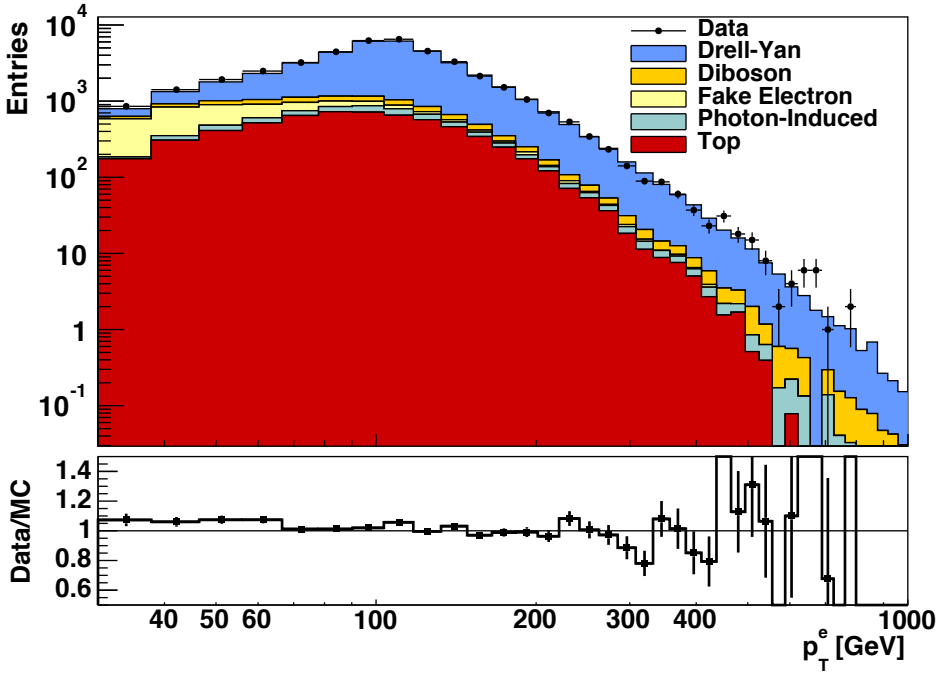

Figure 8.8: Data/MC comparison of the transverse momentum p_T spectrum of all electron candidates passing all selection criteria and $m_{ee} > 200\,\text{GeV}$.

8.2 Comparisons for $m_{ee} > 200\,\text{GeV}$

As this analysis spans a large mass range, but is primarily concerned with the behaviour at high m_{ee}, it is useful to make comparisons of specific mass ranges. Comparisons between the data and the SM expectation using the full mass range suffer from the high overall production cross-section at the Z peak, making it harder to see more subtle effects in the spectra at higher masses. By imposing a requirement of $m_{ee} > 200\,\text{GeV}$ on the following comparisons, the influence of the Z peak is removed. The high mass spectra for p_T, η and ϕ are shown in figures 8.8, 8.9 and 8.10 and are similar to the distributions observed across the full mass range, apart from the decrease in statistical precision due to the lower number of events.

The plots for the event kinematics, $\Delta\eta$, $\Delta\phi$ and ΔR, show changes at higher m_{ee} compared to the full mass range comparisons. Figures 8.11 and 8.13 show the increasing contribution of the fake electron background at high $\Delta\eta$ and ΔR.The shape of the Drell-Yan contribution changes as well, with its contribution becoming flatter in $\Delta\eta$ in the region $\Delta\eta < 2$, compared to figure 8.5, which shows a "plateau" of Drell-Yan events two orders of magnitude above the next contribution for $\Delta\eta \lesssim 1.5$. This is also

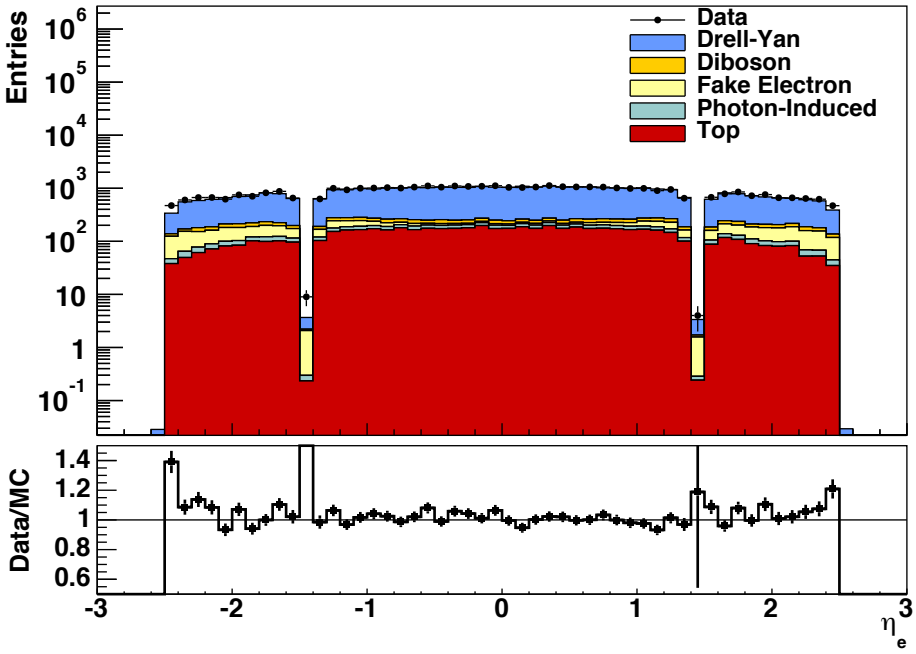

Figure 8.9: Data/MC comparison of the η spectrum of all electron candidates passing all selection criteria and $m_{ee} > 200\,\text{GeV}$.

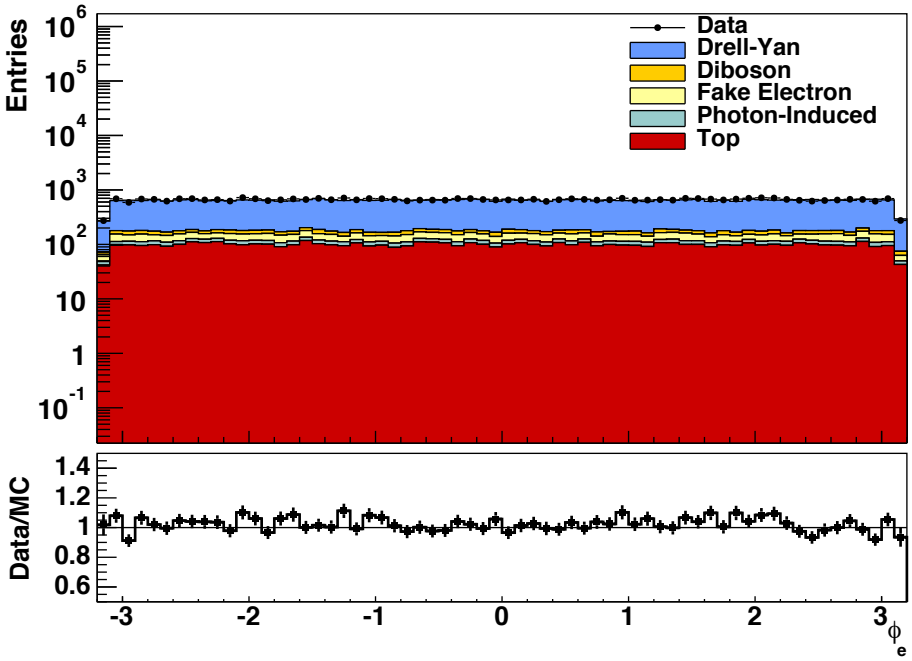

Figure 8.10: Data/MC comparison of the ϕ spectrum of all electron candidates passing all selection criteria and $m_{ee} > 200\,\text{GeV}$.

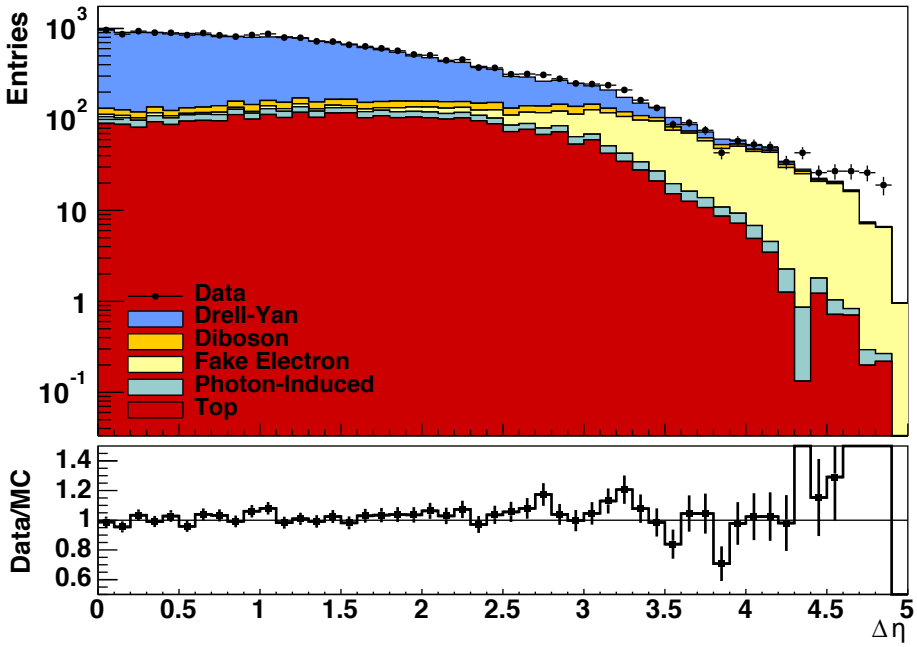

Figure 8.11: Data/MC comparison of the opening angle between the electron candidate pairs with $m_{ee} > 200\,\text{GeV}$ in the η plane.

mirrored in the ΔR distribution, where all contributions with a $\Delta R < 3$ reduce, especially Drell-Yan. This also shows that high mass events have a higher ΔR in general, which corresponds to a larger opening angle between the electron pair. This is expected as events at higher masses become more central.

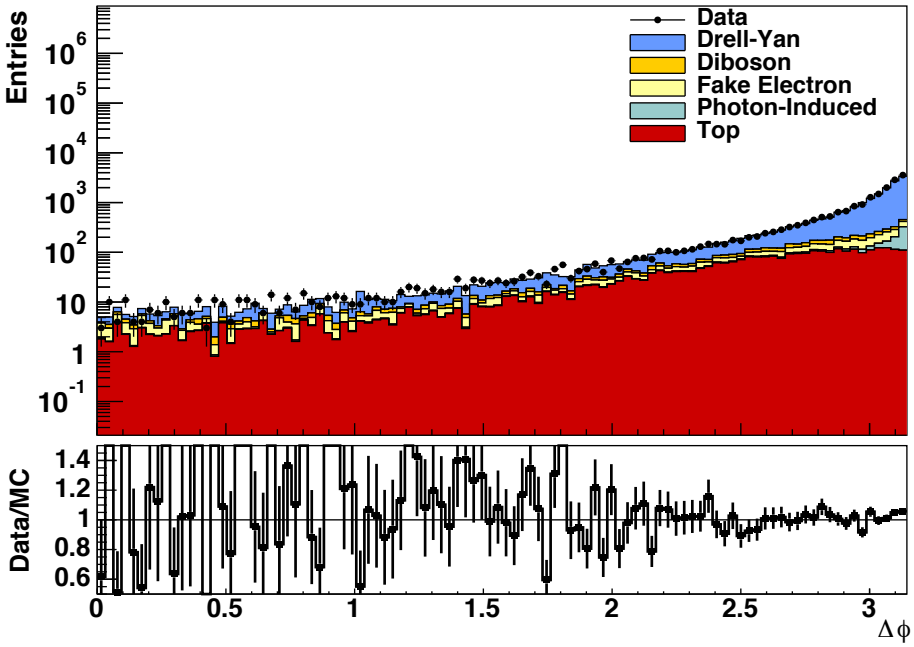

Figure 8.12: Data/MC comparison of the opening angle between the electron candidate pairs with $m_{ee} > 200\,\text{GeV}$ in the ϕ plane.

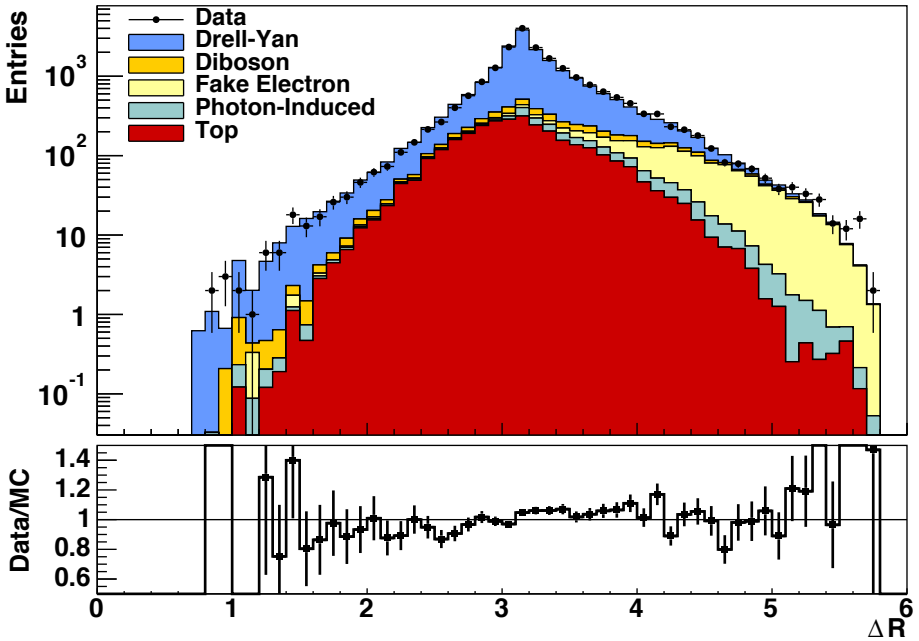

Figure 8.13: Data/MC comparison of the opening angle ΔR between the electron candidate pairs with $m_{ee} > 200\,\text{GeV}$.

Chapter 9

Systematic Uncertainties

The statistical treatment of the results, especially in the context of setting cross-section limits, not only requires a comparison of data with theory, but also requires an understanding of the systematic uncertainties involved. The following sections give an overview of the systematic errors established in previous sections (9.1) as well as a description of the additional systematic errors included (section 9.2).

9.1 Experimental Uncertainties

The experimental uncertainties are mainly due to the electron energy calibration, electron efficiencies and electron energy resolution (see section 6.5 for the determination of the uncertainties). Further experimental uncertainties are introduced through the LHC proton beam measurements themselves, resulting in a 2.8% luminosity uncertainty (see section 6.1) and proton beam energy uncertainty which is treated separately (see below). The experimental uncertainties are listed in table 9.1 for selected mass points, ordered in magnitude of the effect at 3 TeV.

9.2 Model-based Uncertainties

Additional systematic uncertainties are introduced through the modelling of the SM expectation. The dominant model-based uncertainties are due to PDF-related uncertainties as characterised in section 4.2 through the k-factor, combining the uncertainties due to the inherent PDF uncertainty, the PDF choice and the value of α_S. The next large systematic

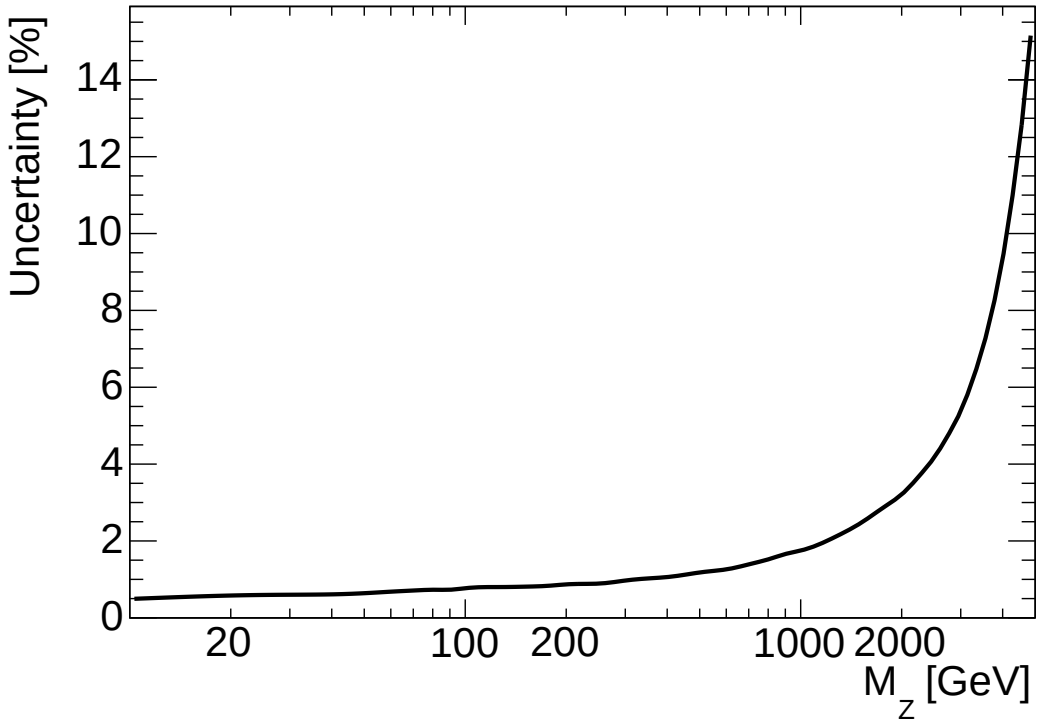

Figure 9.1: Systematic uncertainty on the NC DY production cross-section due to the beam energy uncertainty.

uncertainty contributing is the systematic uncertainty in the fake electron background, as described in section 7.4. A further large systematic uncertainty is associated the photon-induced background as described in chapter 4.3.

In addition, the beam energy uncertainty, while experimental in nature, is treated as a model-based uncertainty here: As noted in chapter 2, the proton beams delivered by the LHC during the 2012 run are not at exactly 4 TeV but rather at 3988 ± 26 GeV [55]. As the cross-section times branching ratio of processes is dependent on the centre-of-mass energy, this uncertainty is calculated by using VRAP to determine the cross-section uncertainty for the NC DY contribution. The symmetrised uncertainty is plotted in figure 9.1 and shows that the uncertainty stays below 1% up to 500 GeV and then exponentially increases until it reaches over 14% at 5000 GeV.

The systematic uncertainty due to the top and the diboson contributions is negligible, with the systematic uncertainty of both contributions being in the region of 5%-6%. However, as their contribution to the overall SM expectation is small (see section 8.1), the contribution to the overall uncertainty is below 1%. The model-based uncertainties are also listed in table 9.1, ordered by the magnitude of the effect at 3 TeV.

Electroweak Uncertainty: The k-factor correction to the NC DY sample in section 4.2 only includes PDF-based uncertainties in the lower and upper bound of the NNLO k-factor. However, the electroweak correction included in the k-factor introduces an additional uncertainty as there are two possible approaches to including the electroweak effects, the additive approach and the factorised approach (see [90]). The term $\sigma_{FEWZ,QCD_{NNLO}+EW_{NLO}}$ from equation 4.4 can either be described as:

$$\sigma_{FEWZ,QCD_{NNLO}+EW_{NLO}} = k_{QCD} \times k_{EW\times\sigma_{LO,QCD}}, \tag{9.1}$$

where the EW correction enters the NNLO cross-section as an extra factor independent of the order in QCD, or as:

$$\sigma_{FEWZ,QCD_{NNLO}+EW_{NLO}} = \sigma_{NNLO,QCD} + \Delta\sigma_{LO,QCD+NLO,EW}, \tag{9.2}$$

where the EW correction is not an overall factor, but an extra additive term to the cross-section. As an additive term, the EW correction becomes dependent on the order in QCD, whereas it is independent in the factorisation approach. In the FEWZ calculations in section 4.2, the additive approach of equation 9.2 is assumed. In order to quantify the uncertainty due to the difference, δ_{miss} is introduced, defined as:

$$\delta_{miss} = \frac{\sigma_{QCD,NLOEW} - \sigma QCD}{\sigma_{QCD}}. \tag{9.3}$$

By calculating δ_{miss} with different orders in QCD, while keeping the electroweak correction at NLO, it is possible to estimate the impact of the two approaches. These calculations are done for FEWZ, resulting in a $\delta_{miss}(QCD, LO)$ and $\delta_{miss}(QCD, NNLO)$ using MSTW as PDF. Additionally, $\delta_{miss}(QCD, NNLO)$ is calculated using MSTWnnlo and CT10nnlo, with the difference giving the effect due to the PDF choice. By adding both in quadrature, the overall systematic uncertainty on the electroweak correction is estimated. This systematic error is fitted over the mass range 66 GeV–5000 GeV, as shown in figure 9.2. It can be seen that the is small overall, staying below 1% up to 1000 GeV and only becoming significant at about 2000 GeV, where it reaches 3% and increases up to 10% around 4500 GeV.

Table 9.1: Overview of all the systematic uncertainties relative to the total SM expectation in the mass range 1 TeV–3 TeV.

	Uncertainty [%]		
Source	m_{ee} =1 TeV	m_{ee} =2 TeV	m_{ee} =3 TeV
Energy Scale	2.1	2.7	3.7
Luminosity	2.8	2.8	2.8
Reconstruction and Identification	2.9	2.8	2.7
Energy Resolution	<1.0	<1.0	<1.0
PDF + α_S+ PDF Choice	6.4	16.7	40.3
Fake Electron	4.4	10.6	18.4
Photon-Induced	2.3	5.4	9.5
Beam Energy	1.2	2.5	3.8
Electroweak	0.8	2.0	3.1
Top	<1.0	<1.0	<1.0
Diboson	<1.0	<1.0	<1.0
Total Experimental	4.6	4.8	5.4
Total Model-Based	8.2	20.8	45.6
Total	9.4	21.3	45.9

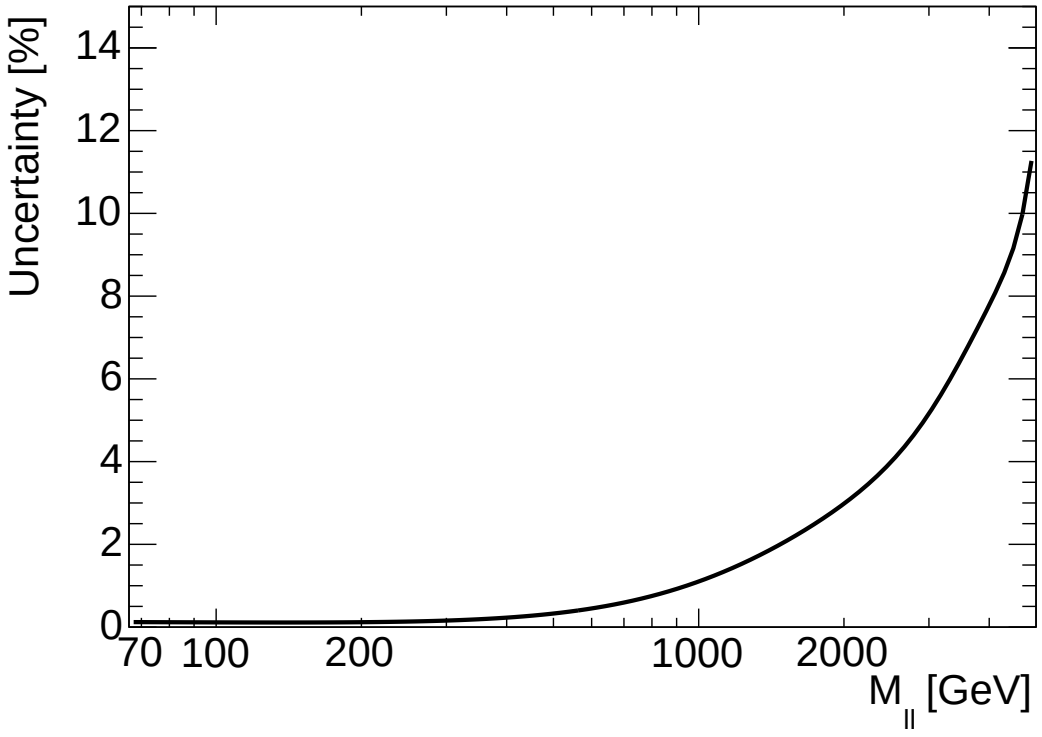

Figure 9.2: Systematic uncertainty due to choice of approach for higher-order electroweak corrections except QED FSR.

Chapter 10

Statistical Test of Signal Hypotheses

The comparison of data to the SM expectation in chapter 8 has shown good agreement with no obvious excesses or deviations, indicating that the Standard Model alone is sufficient to explain the observed spectra. In order to verify this, statistical techniques are used to quantify the significance of the results and to place limits on the cross-section for the Z'_{SSM} signal. For the purpose of this search, the Standard Model expectation is generally described as "Standard Model background". In this chapter, the methodology will be outlined first (section 10.1), followed by a brief determination of the acceptance (section 10.2). At the end of the chapter, the extracted p-values and signal cross-section limits will be presented and discussed (sections 10.3 and 10.4).

10.1 Methodology

Searching for a signal requires statistical techniques to decide whether an observation is consistent with a given hypothesis, in this case either the null or background hypothesis (the Standard Model background) or a signal hypothesis. As the analysis deals with discrete events, it is possible to describe the experimental outcome using Poisson statistics. Given a number of observed events and an expectation, the likelihood $\mathcal{L}$ is described as:

$$\mathcal{L}(N|\mu) = \frac{\mu^N e^{-\mu}}{N!} \tag{10.1}$$

for exactly N events for an expected value of μ, where $N = N_{data}$ and μ can be decomposed into:

$$\mu = \sum_i N_{prediction} = N_{signal} + N_{SM} = N_{signal} + \sum N_{MC} + N_{QCD} \tag{10.2}$$

with N_{MC} corresponding to the Monte Carlo prediction from chapter 4 and N_{QCD} corresponding to the fake electron background estimated in chapter 7. As the data is described with a binned invariant mass spectrum in this analysis, every bin in the spectrum has its own likelihood which is then multiplied to find the overall likelihood:

$$\mathcal{L}(N|\mu) = \prod_{j=1}^{n_{bins}} \frac{\mu^{N_j} e^{-\mu_j}}{N_j!}. \tag{10.3}$$

Following a Bayesian treatment of systematic uncertainties, every μ can vary around a central value as determined by a nuisance parameter θ_k:

$$\mu_j \to \mu'_j = \mu_j(1 + \sum_{k=1}^{n_{syst}} \theta_k \epsilon_{kj}), \tag{10.4}$$

where ϵ_{kj} is the size of the systematic effect for uncertainty k in bin j. Assuming a Gaussian prior G for the nuisance parameter, equations 10.3 and 10.4 can be combined:

$$\mathcal{L}(N|\mu,\theta) = \prod_{j=1}^{n_{bins}} \frac{\mu^{N'_j} e^{-\mu'_j}}{N_j!} \prod_{k}^{n_{syst}} (1 + G(\theta_k, 0, 1)). \tag{10.5}$$

In order to calculate a likelihood that is only a function of N_{signal}, it is necessary to integrate over the probability functions of all nuisance parameters resulting in the marginalised likelihood:

$$\mathcal{L}'(n|\sigma_{Z'}B) = \int \mathcal{L}(n|\sigma_{Z'}B,\theta,\epsilon) \prod_{k=1}^{n_{syst}} d\theta_k. \tag{10.6}$$

Global *p*-value: The significance of an outcome is quantified using a p-value, which is defined as a one-sided integral of a Gaussian distribution of unit width and describes the probability that the null hypothesis can describe the seen outcome. The width is given in units of standard deviations, σ. Evidence of a signal can be claimed at $+3\sigma$, which corresponds to $p < 1.35 \times 10^{-3}$, meaning a 0.14% chance that the null hypothesis

(in this context, the Standard Model-only hypothesis) would result in this outcome. Discovery is usually claimed at $+5\sigma$ or $p < 2.87 \times 10^{-7}$.

The two possible hypotheses are compared using the log-likelihood ratio LLR, following the Neyman-Pearson lemma [116] which states that the LLR is the statistically most powerful test to distinguish between two hypotheses:

$$LLR = -2 \ln \frac{\mathcal{L}(N|\mu_{signal}, \theta', \epsilon)}{\mathcal{L}(N|\mu_{SM}, \theta'', \epsilon)} \tag{10.7}$$

where μ_{signal} and θ' are the best-fit values for a given model and μ_{SM} and θ'' are the best fit values for the Standard mModel-only hypothesis.

It is then possible to define the global p-value as follows:

$$p = p(LLR \leq LLR_{observed}|H_0). \tag{10.8}$$

Signal Cross-section Limit: In order to actually set a limit on the production of Z'_{SSM} bosons, the likelihood $\mathcal{L}(n|\mu, \theta)$ is used. In order to generalise the number of expected signal events μ to a limit on the cross-section, a modified version of equation 2.1 is used:

$$N = A \times \epsilon_{eff} \sigma B L, \tag{10.9}$$

where L is the total integrated luminosity and σB is the process cross-section times the branching ratio. The branching ratio B is the fraction of decays that produce the e^+e^- signal in an individual decay channel out of all possible decays. In this case, $B(Z'_{SSM} \rightarrow e^+e^-)$ describes how many of all produced Z'_{SSM} bosons decay in the di-electron channel. $A \times \epsilon_{eff}$ describes the acceptance times the overall detector efficiency, meaning it measures the ratio of total events to the number of events recorded by the detector (also see sections 4.1 and 10.2).

However, for a search, the interest not only lies in comparing the agreement of an observed result with a particularhypothesis but also in determining the credibility of a theory given the data. The Bayesian approach allows the assignment of credibility intervals to parameters, in this case the mass of a new resonance. Bayes' theorem states:

$$P(theory|data) = \frac{P(data|theory)\pi(theory)}{\pi(data)}. \tag{10.10}$$

That is, it gives the posterior probability $P(data|theory)$ given the prior probabilities $\pi(theory)$ and $\pi(data)$. Applying equation 10.10 to equation 10.6 yields:

$$\mathcal{L}'(\sigma_{Z'}B|n) = \frac{\mathcal{L}'(n|\sigma_{Z'}B)\pi(\sigma_{Z'}B)}{\pi(n)}. \tag{10.11}$$

The prior for the observed data $\pi(n)$ is independent of theory predictions and is taken as constant and non-zero here. $\pi(\sigma_{Z'}B)$ is chosen to be a flat prior so that $\pi(\sigma_{Z'}B) = 1$. In order to place a 95% confidence limit, the posterior probability is integrated up to the value $(\sigma_{Z'}B)_{95}$ suchh that

$$0.95 = \frac{\int_0^{(\sigma_{Z'}B)_{95}} \mathcal{L}'(\sigma_{Z'}B|N)d(\sigma_{Z'}B)}{\int_0^{\infty} \mathcal{L}'(\sigma_{Z'}B|N)d(\sigma_{Z'}B)}. \tag{10.12}$$

10.2 Signal Acceptance

The reweighted sample (see section 5.2) is also used to derive the $A \times \epsilon$ for the Z'_{SSM} signal. This is done by reweighting the PYTHIA8 sample to each Z'_{SSM} pole mass in the range of 150 GeV–4500 GeV in steps of 50 GeV but without the SM contribution to the template (as the neutral current DY production would overwhelm the Z'_{SSM} signal of interest), using equation 5.2 for every event. In order to calculate $A \times \epsilon$, the ratio of all events passing reconstruction over all generator level events with a Z'_{SSM} with a mass of 75 GeV or greater is taken and plotted against the Z'_{SSM} pole mass used for the reweighting, resulting in figure 10.1.

This curve is then fitted with a polynomial of the form $A \times \epsilon = p_0 + p_1 x + p_2 x^2 + p_3 x^3 + p_4 x^5 + p_5 x^5 + p_6 x^6$ with x being the pole mass in TeV. This results in a fit with a $\chi^2/d.o.f. = 82.657/74 = 1.117$ and the parameters $p_0 = 0.2244$, $p_1 = 1.263$, $p_2 = -1.374$, $p_3 = 0.7915$, $p_4 = -0.2501$, $p_5 = 0.04004$ and $p_6 = -0.002526$. It can be seen that the acceptance rises with Z'_{SSM} pole mass up to about 71% in the region of 1500 GeV–2000 GeV and slowly falls to about 60% at 3500 GeV (the highest mass used for the limit setting described in section 10.3). The rise is due to the increased mass of the Z'_{SSM} causing electrons to be produced more centrally and with higher p_T, falling into the acceptance of the detector. The decrease in $A \times \epsilon$ at very high masses occurs as the parton luminosity decreases rapidly for high Bjorken-x, meaning off-shell production increases and "broadens" the mass peak.

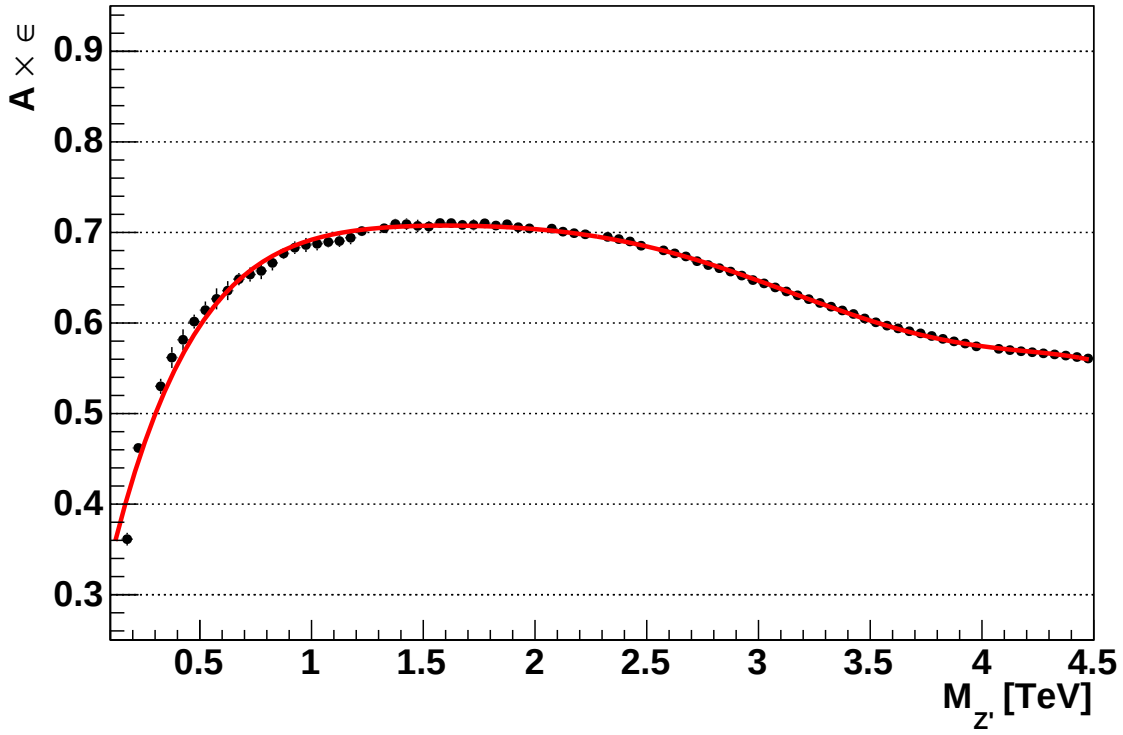

Figure 10.1: $A \times \epsilon$ for Z'_{SSM} pole masses of 150 GeV–4500 GeV based on the reweighted PYTHIA8 sample. Every point corresponds to the acceptance of a particular Z'_{SSM} pole mass. See text for the fitted function.

10.3 Results

The Bayesian Analysis Toolkit [117] is used to perform all limit calculations in this analysis, based upon the procedure established in previous Z' searches [118, 115]. The input for BAT consists of histograms describing the data and Standard Model background distributions (see chapters 4, 6 and 7) together with histograms describing the relative size of the associated systematic uncertainties, described in chapter 9. The experimental systematic uncertainties for the electron energy scale and the reconstruction and identification scale factors are both electron-based and are treated as fully correlated in signal and background and are hence not included. The energy resolution uncertainty is <1% and is hence ignored, leaving the luminosity uncertainty as the only included experimental error as it influences the normalisation of the signal cross-section. The model-based uncertainties include all those listed in table 9.1, except the uncertainty due to the top and the diboson background, as both are negligible (treating the beam energy uncertainty as "model-based").

The size of the systematic uncertainty is used in their modelling as nuisance parameters. For comparison to the signal hypothesis, an array of signal templates is provided, describing the shape of the Z'_{SSM} poles (see chapter 5) in the range 150 GeV–3500 GeV. An overview of the input histograms can be found in appendix B.

Global *p*-value: The first part of the calculation, the determinator of the global p-value, is done by using the LLR as described above. In order to compare the result to the outcome, toy experiments or pseudo-experiments (PEs) are done. These pseudo-experiments are generated using the SM-only hypothesis as characterised by the Monte Carlo and QCD background templates, varied within the statistical and systematic uncertainties associated with the background templates. The LLR is then sampled over the entire range of Z'_{SSM} pole masses, shown in figure 10.2, indicating the point with the most signal-like LLR at $M_{Z'_{SSM}} = 950\,\text{GeV}$. The distribution of PEs at that point is shown in figure 10.3, where the yellow area is a histogram representing the LLR produced by 2500 pseudo-experiments and the blue arrow indicates the LLR found in data. The global p-value at this point found to be 0.872, meaning that there is a 87.2% probability that the null hypothesis results in the observed outcome.

Signal Cross-section Limit: The limit on the Z'_{SSM} cross-section is also calculated using the BAT, using the reweighted Z'_{SSM} samples to derive a 95% C.L. limit as described in equation 10.12 for each mass point from 150 GeV–3500 GeV. Similar to the p-value

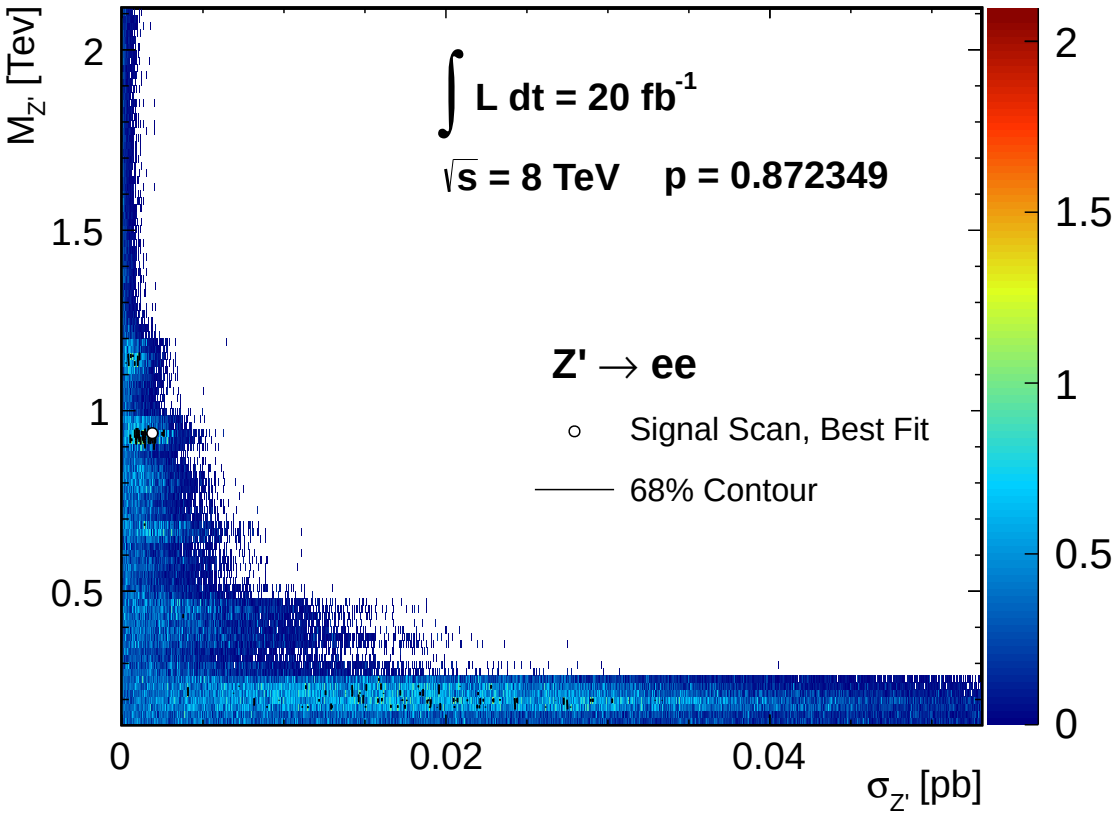

Figure 10.2: Absolute LLR of the search depending on the mass $M_{Z'_{SSM}}$ and its production cross-section $\sigma_{Z'_{SSM}}$. The position of the most signal-like LLR is indicated by the white marker at $M_{Z'_{SSM}} = 950\,\text{GeV}$.

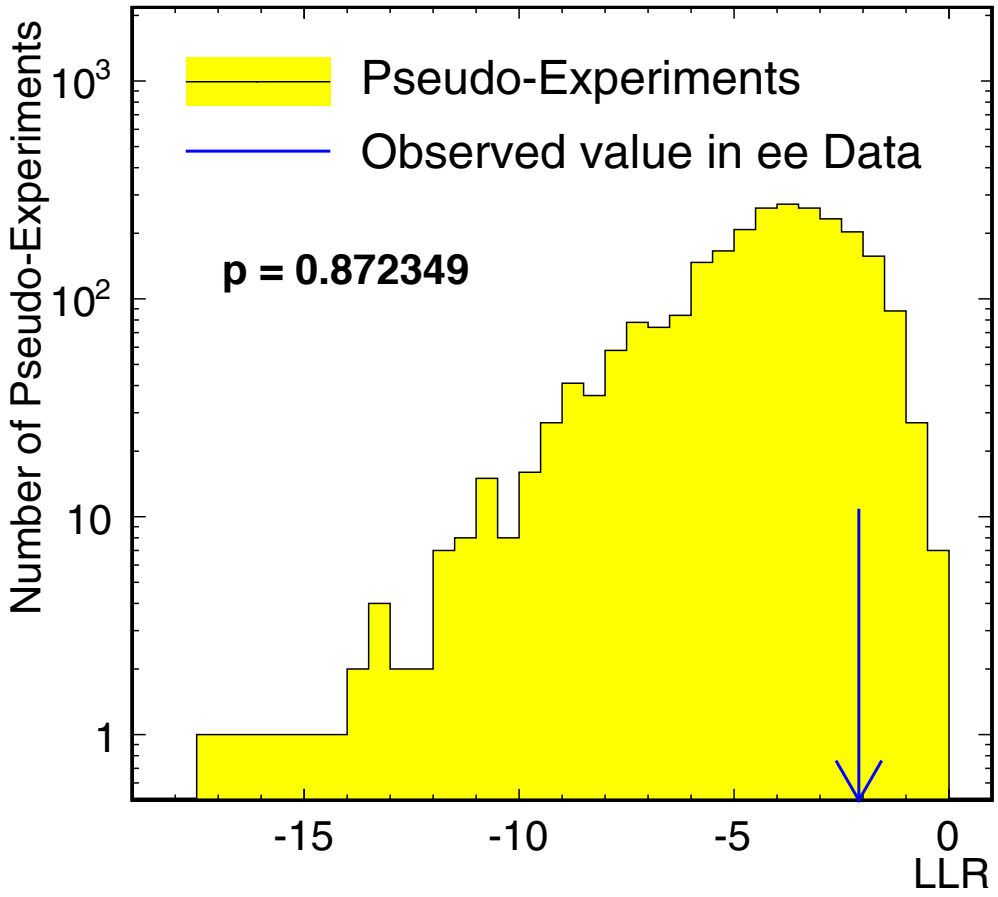

Figure 10.3: Distribution of LLR results from 2500 pseudo-experiments and the LLR found in data (blue arrow).

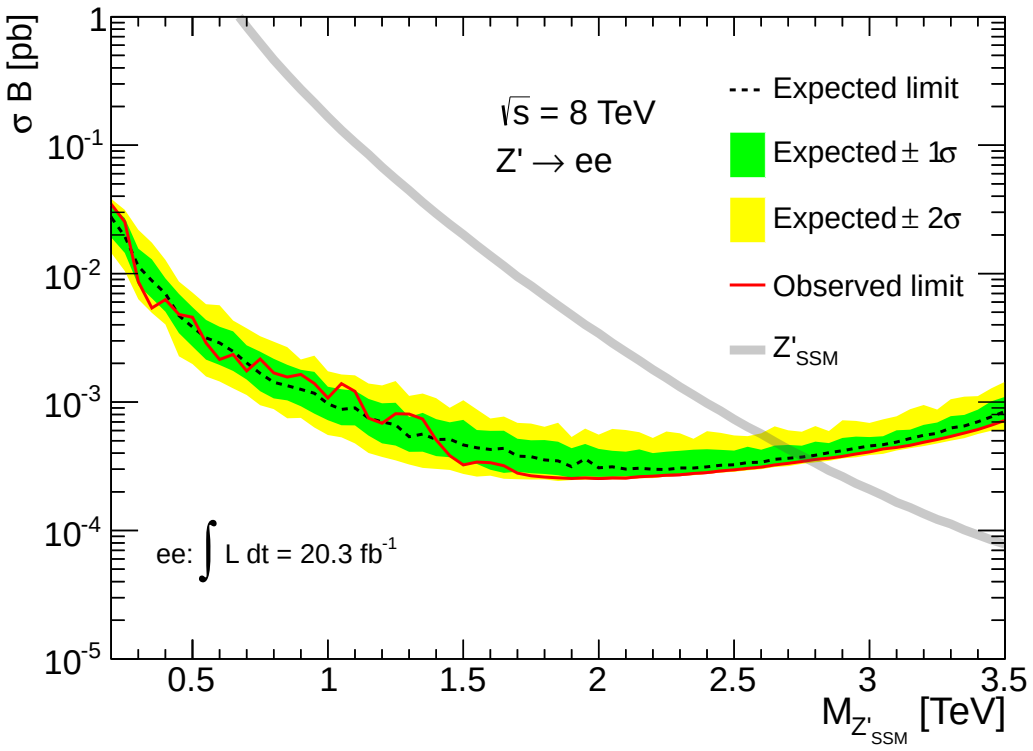

Figure 10.4: Cross-section times branching ratio limit on the Z'_{SSM} production in the $Z' \to ee$ channel with the dotted line and green and yellow bands indicating the expected limit and the $\pm 1\sigma$ and $\pm 2\sigma$ of the expected limit. The red line shows the observed limit and the grey line the Z'_{SSM} cross-section predicted by theory. The intercept between the cross-section prediction and the cross-section limit determines the lower limit on the Z'_{SSM} mass.

determination, pseudo-experiments are used to produce a prediction for the SM-only hypothesis, meaning a signal would show up as a deviation between the expected and the observed limit.

Figure 10.4 shows the result of the procedure with the observed and the expected limits, as well as the theory-predicted Z'_{SSM} cross section. The procedure uses 200 PEs per Z'_{SSM} mass point to determine the expected limit. The region where the observed limit lies below the predicted cross-section is the excluded region, resulting in an observed limit of 2.78 TeV and an expected limit of 2.76 TeV. The expected and predicted cross-section curves rise at higher masses due to the influence of the parton luminosity tail, mirroring the acceptance curve as described in section 10.2.

10.4 Discussion of Results

As the LHC provides pp collisions with an unprecedented luminosity and centre-of-mass energy, this search can access previously unexplored phase space. Nevertheless, no statistically significant excesses with a narrow peak were found in $20.3\,\text{fb}^{-1}$ of recorded di-electron data when compared to the best SM knowledge, leading to a p-value of 87.2% in favour of the SM-only hypothesis.

This analysis places a lower limit on the invariant mass of the Z'_{SSM} at 2.78 TeV, which matches the expected limit of 2.76 TeVwithin the $\pm 1\sigma$ band shown in figure 10.4, confirming the SM-only hypothesis using Bayesian techniques. Using acceptance times efficiency fits from section 10.2, the mass limit is converted into an upper limit on $\sigma \times B$ for Z'_{SSM} resonances of 3.53×10^{-4} pb, with an expected limit of 3.75×10^{-4} pb. As a benchmark model, the Z'_{SSM} exclusion limit also implies that no excesses with a similar shape, namely a narrow resonance peak, can be found in the same mass region. Despite the simplicity of the Z'_{SSM} model, this is a powerful method for restricting the parameter space for beyond the Standard Model physics.

Thanks to the use of the Z'_{SSM} as a benchmark model to establish the sensitivity and range of an experiment, it is possible to compare this result with previous searches for high mass di-lepton resonances, listed in table 10.1. The table lists previous searches at the Tevatron experiments D$\varnothing$ and CDF, which placed limits on the Z'_{SSM} mass around 1 TeV. Comparing the Tevatron results to those of the LHC experiments highlights the power and increased cross-section for beyond the Standard Model physics at the LHC, as even the initial 2010 data periods at much lower integrated luminosity than the Tevatron searches placed limits competitive to the Tevatron limits. The 2011 analyses superseded the Tevatron limits completely and pushed the exclusion into previously inaccessible regions.

This thesis focuses on the Z'_{SSM} as a benchmark model, but the di-lepton resonance search performed at ATLAS [1] also sets limits on other beyond the Standard Model physics, coming to similar conclusions in favour for a wide range of models. Furthermore, similar searches for new heavy charged gauge bosons, W', were performed by the ATLAS [119] and CMS collaborations [120] and placed mass limits on the W'_{SSM} at 3.24 TeV and 3.28 TeV, respectively, further confirming the validity of the SM in the TeV region now accessible thanks to the LHC.

Table 10.1: Overview of Z'_{SSM} limits set by previous analyses, showing the observed and the expected limits in the di-electron channel (e^+e^-) as well as the limits for the combined di-electron and di-muon channels (l^+l^-). To facilitate comparisons with this analysis, the integrated luminosities are for the di-electron channel only. A dash indicates that no data is found or available.

Experiment	$\int Ldt$ [fb^{-1}]	$\sqrt{s}$ [TeV]	Observed Limit e^+e^- [TeV]	Observed Limit l^+l^- [TeV]	Expected Limit e^+e^- [TeV]	Expected Limit l^+l^- [TeV]
CDF (2009) [42]	2.5	1.96	0.96	—	0.96	—
D∅ (2010) [43]	5.4	1.96	1.02	—	1.02	—
ATLAS (2010) [118]	0.04	7	0.96	1.05	0.97	1.09
CMS (2010) [44]	0.04	7	0.96	1.14	—	—
ATLAS (2011) [115]	4.9	7	2.08	2.22	2.13	2.25
CMS (2011) [45]	5.0	7	2.12	2.33	—	—
ATLAS (2012) [1]	20.3	8	2.79	2.90	2.76	2.87
CMS (2012) [121]	19.6	8	2.65	2.96	—	—
This analysis (2012)	20.3	8	2.78	—	2.76	—

Chapter 11

Conclusions

This thesis describes a search for new heavy Z'_{SSM} gauge bosons in the high mass di-electron spectrum for the $20.3\,\text{fb}^{-1}$ of data taken with ATLAS during the 2012 run of the Large Hadron Collider. During this data taking period, the LHC collided protons with a centre-of-mass energy of $\sqrt{s} = 8\,\text{TeV}$, providing unprecedented luminosity and energy to explore previously inaccessible regions of phase space and challenging the Standard Model at the TeV scale.

The di-electron invariant mass spectrum m_{ee} is measured within the region $80\,\text{GeV} < m_{ee} < 4500\,\text{GeV}$. The SM expectation for the spectrum is described using Monte Carlo samples for neutral current Drell-Yan production, photon-induced di-lepton production, diboson and top production. In addition, the background from fake electrons is estimated using data-driven methods.

The previous 2011 data taking and di-lepton resonance searches established limits at roughly 2 TeV. As the search pushed into previously unexplored regions, it became crucial for search efforts to fully understand the Standard Model and associated uncertainties at a mass range of $m_{ee} > 2\,\text{TeV}$. The work in this thesis helped in the development of novel techniques to significantly improve the description of Standard Model background, dominated by neutral current Drell-Yan process in this high mass range for the ATLAS collaboration. These improvements include:

- New higher-order correction factors to the neutral current Drell-Yan cross-section including the impact of systematic uncertainties due to the PDF uncertainty, the α_S uncertainty and the PDF choice.
- A more rigorous approach to the W/Z radiation using mass-dependent correction factors compared to the flat overall correction factors used before.

- Addition of the systematic uncertainty due to higher order electroweak corrections (without QED FSR).
- Inclusion of the photon-induced contribution and associated uncertainties through correction factors.

Using these state-of-the-art descriptions of the Standard Model expectation, the data is compared to expectation and to Z'_{SSM} boson signal templates with pole masses of $150\,\text{GeV} < M_{Z'_{SSM}} < 3500\,\text{GeV}$, generated from a single Monte Carlo sample using a reweighting technique to efficiently produce a large range of templates with small mass steps of 50 GeV. Using a statistical framework, no statistically significant excesses were found, resulting in a p-value of 87.2% in favour of the SM-only hypothesis. Subsequently, a 95% C.L. Bayesian minimum mass limit was set on the Z'_{SSM} at 2.76 TeV corresponding to a maximum $\sigma \times B(Z'_{SSM} \to e^+e^-)$ of 3.53×10^{-4} pb for new heavy Z'_{SSM} gauge bosons in the di-electron mass spectrum.

The work presented here is included in the 2013 conference note [122] of the di-lepton heavy resonance search and the subsequent paper [1], both published by the ATLAS collaboration. Going beyond the ATLAS analysis, this thesis also explores an improved description of the photon-induced background contribution by using Monte Carlo samples. Furthermore, an alternative approach to inclusion of the PDF-based uncertainties in the limit setting is used here, mirroring the approach in the ATLAS W' analysis, as well as a different approach to the fake electron background. Nevertheless, the analysis presented here yields results consistent with the ATLAS analysis, highlighting the robustness of the techniques used.

Appendix A

Further Control Plots

Following are data-Monte Carlo comparison plots that were used to verify the outcome of the Monte Carlo corrections applied as well as to study rapidity y and ϕ-distribution of the e^+e^- system as a whole.

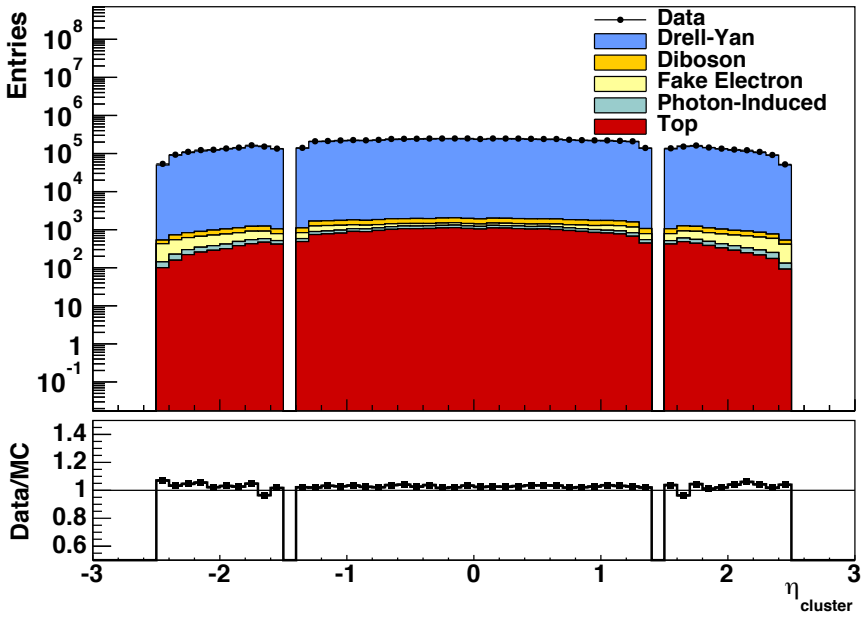

Figure A.1: Distribution of the energy deposition clusters of electron candidates in the ECAL in η for the full mass range of events.

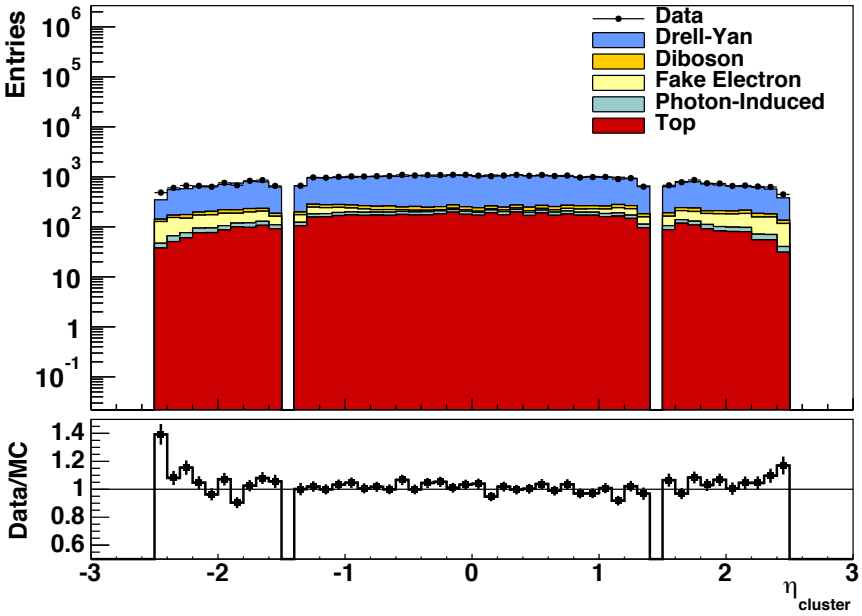

Figure A.2: Distribution of the energy deposition clusters of electron candidates in the ECAL in η for events with $m_{ee} > 200\,\text{GeV}$.

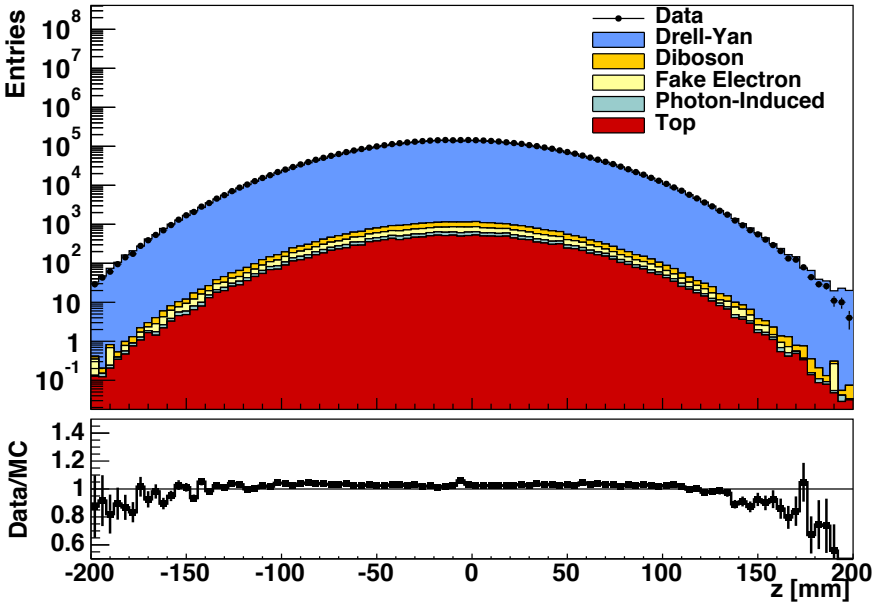

Figure A.3: Z-vertex distribution of the primary event vertex for the full mass range of events.

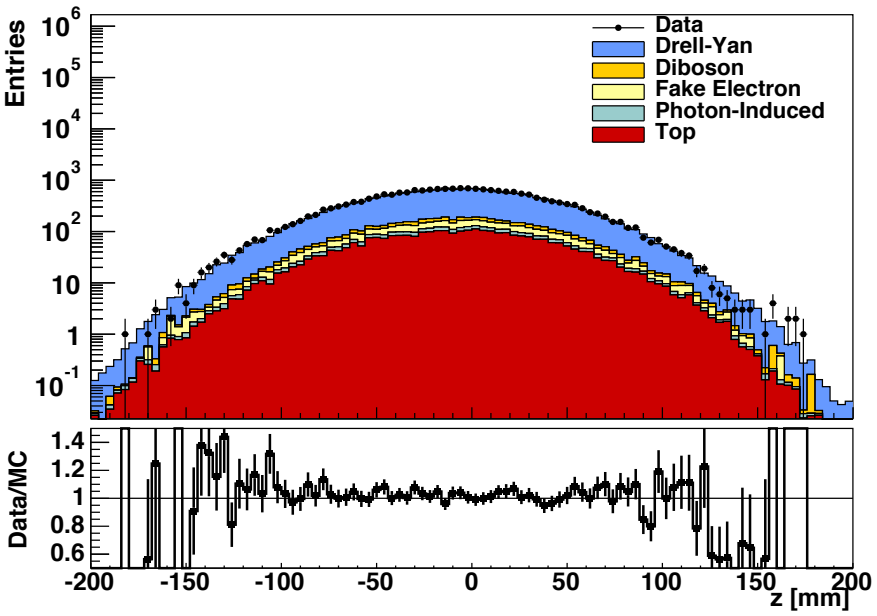

Figure A.4: Z-vertex distribution of the primary event vertex for events with $m_{ee} > 200\,\text{GeV}$.

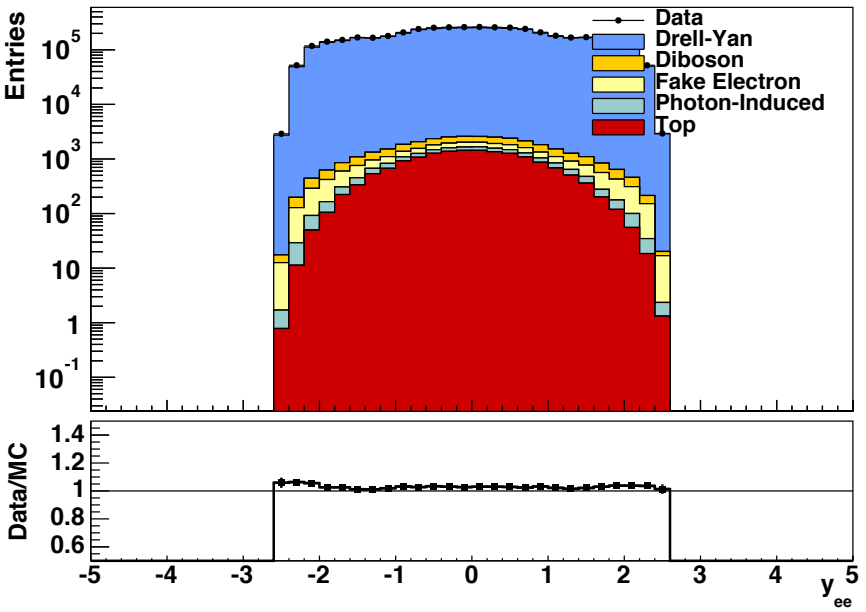

Figure A.5: Rapidity distribution y_{ee} for leading electron pair for the full mass range of events.

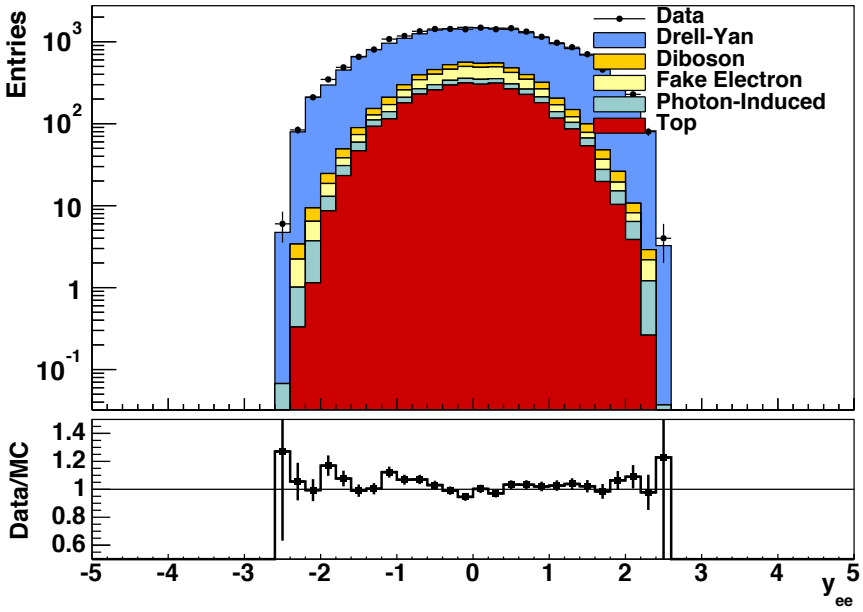

Figure A.6: Rapidity distribution y_{ee} for leading electron pair for events with $m_{ee} > 200\,\text{GeV}$.

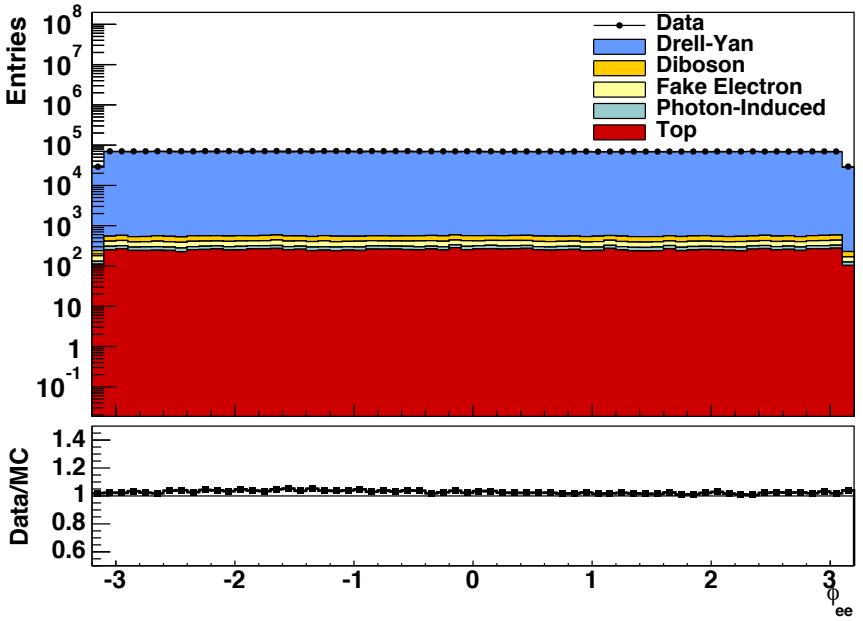

Figure A.7: Angular distribution ϕ_{ee} for leading electron pair for the full mass range of events.

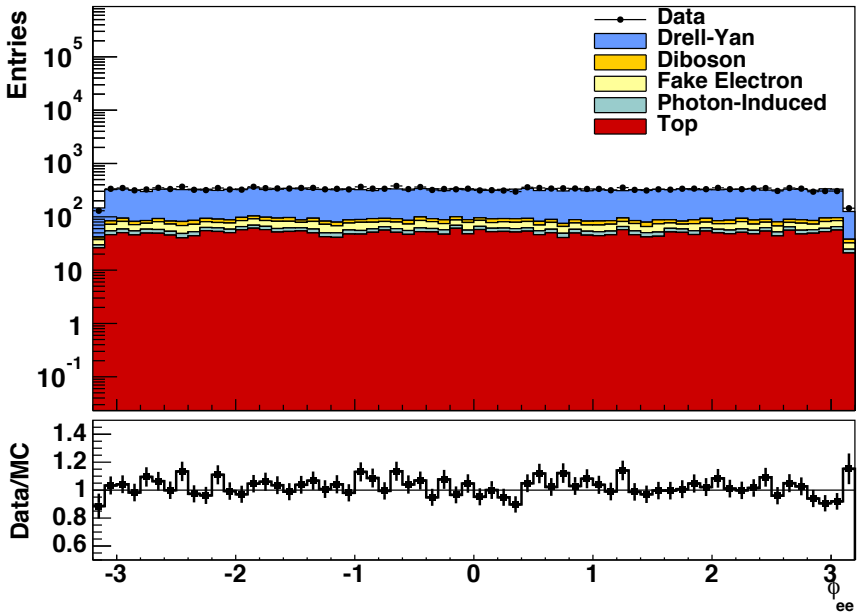

Figure A.8: Angular distribution ϕ_{ee} for leading electron pair for events with $m_{ee} > 200\,\text{GeV}$.

Appendix B

Bayesian Analysis Toolkit Inputs

In order to use the BAT for the statistical analysis, all inputs need to use a uniform format. In this analysis, the inputs take the form of histograms covering the range 0.128 TeV–4.500 TeV, divided into 53 bins with logarithmically increasing width. The input histograms for the systematics show the size of the systematic uncertainty with respect to the total background estimate, whereas in the main text they are usually presented with respect to the associated distribution.

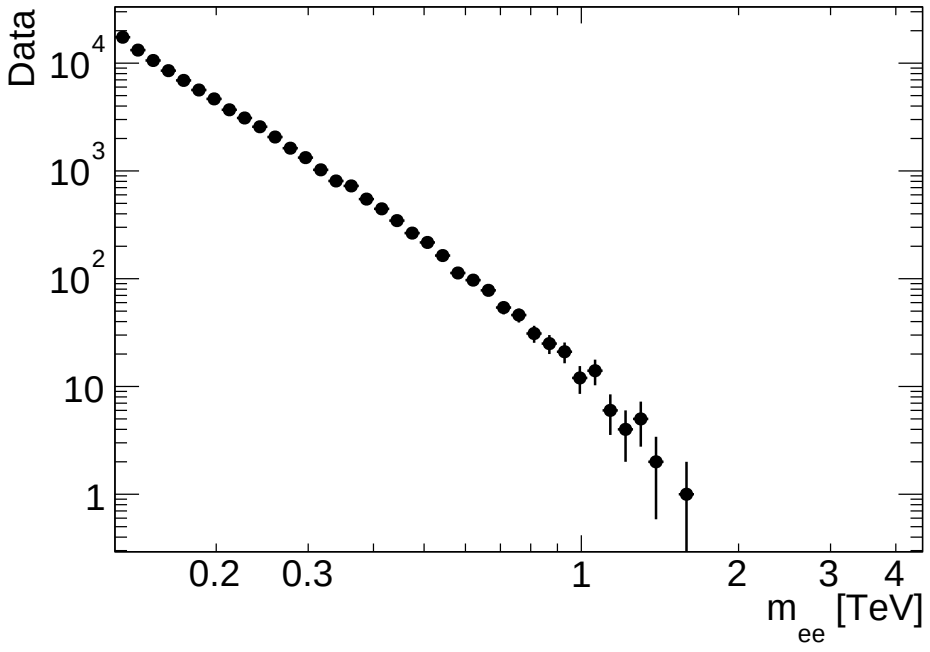

Figure B.1: Data distribution as BAT input histogram for the statistical analysis.

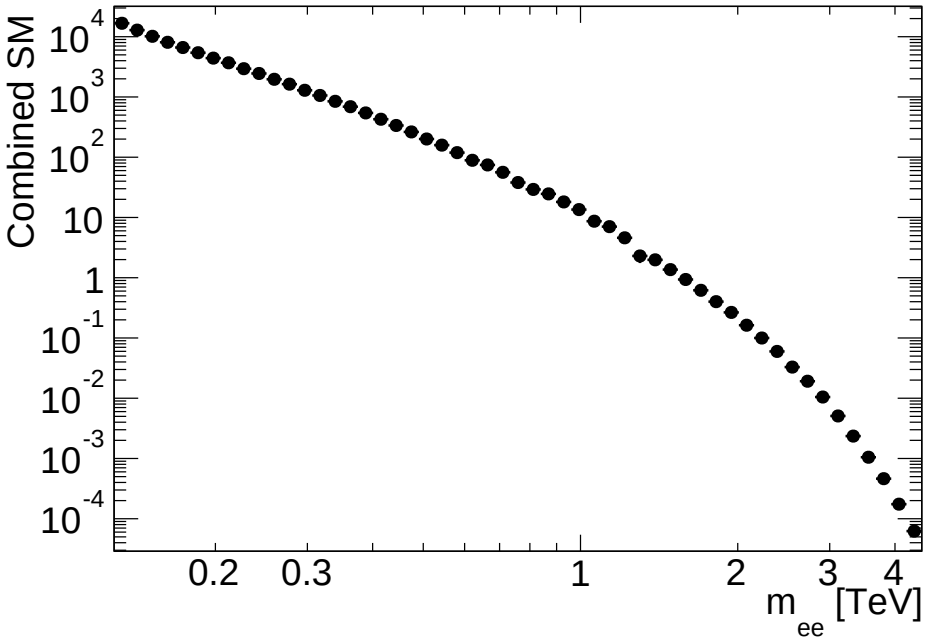

Figure B.2: SM expectation as BAT input histogram for the statistical analysis.

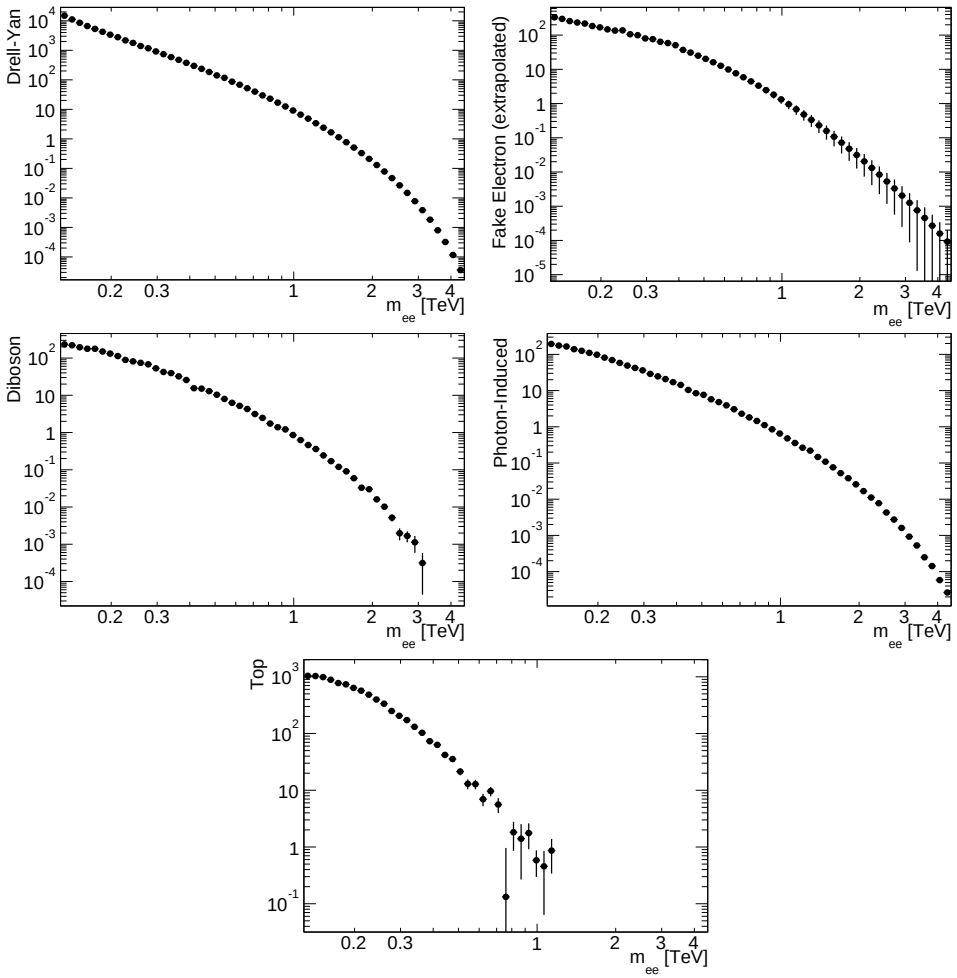

Figure B.3: Individual histograms for various contributions to the SM expectation in B.2. In left-to-right, top-to-bottom order: Drell-Yan contribution, fake electron contribution, diboson contribution, photon-induced contribution and top contribution.

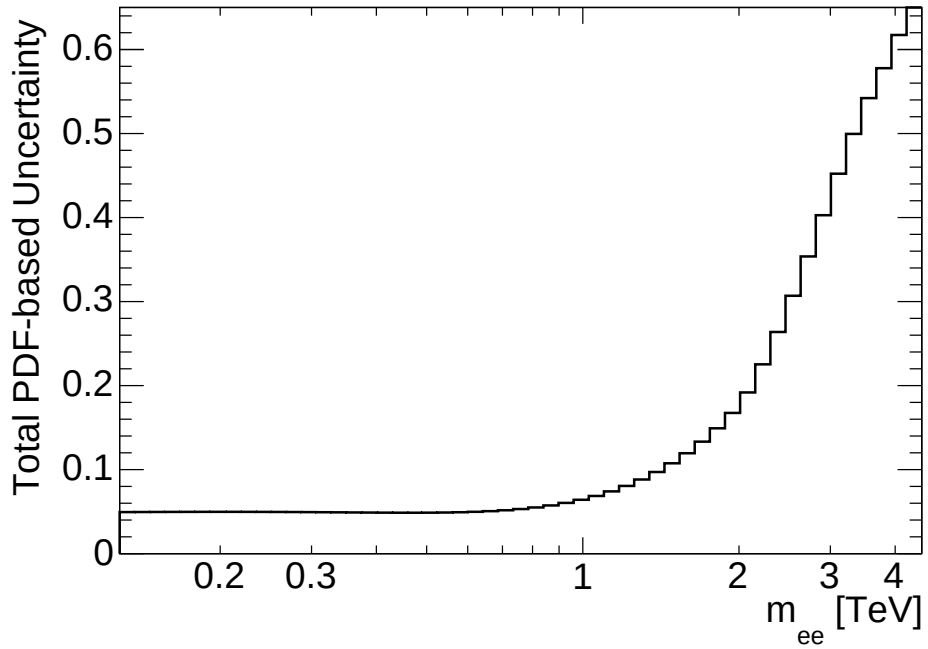

Figure B.4: Systematic uncertainty associated with the α_S+ PDF + PDF choice normalised to the total SM expectation.

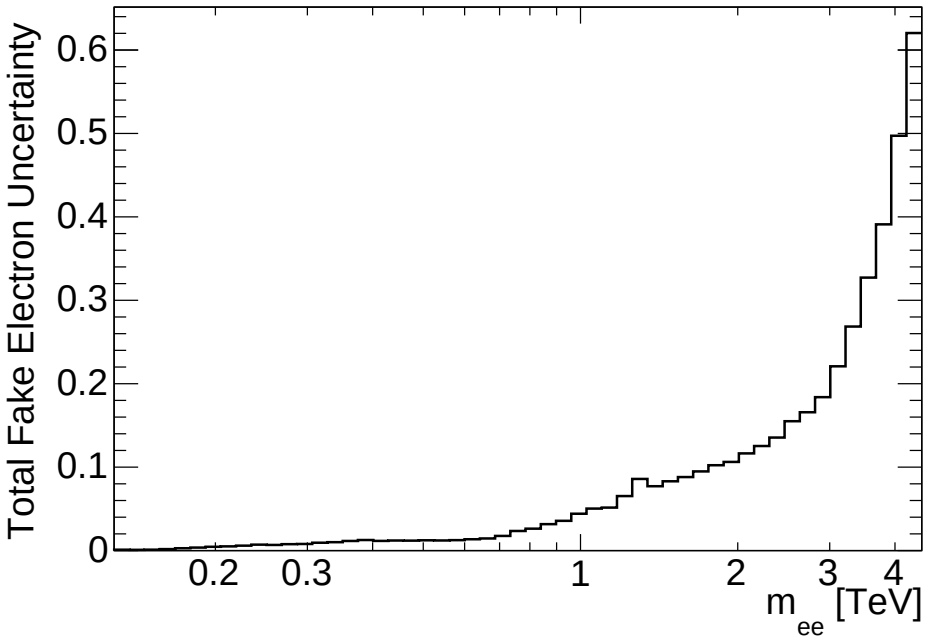

Figure B.5: Systematic uncertainty associated with the fake electron background normalised to the total SM expectation.

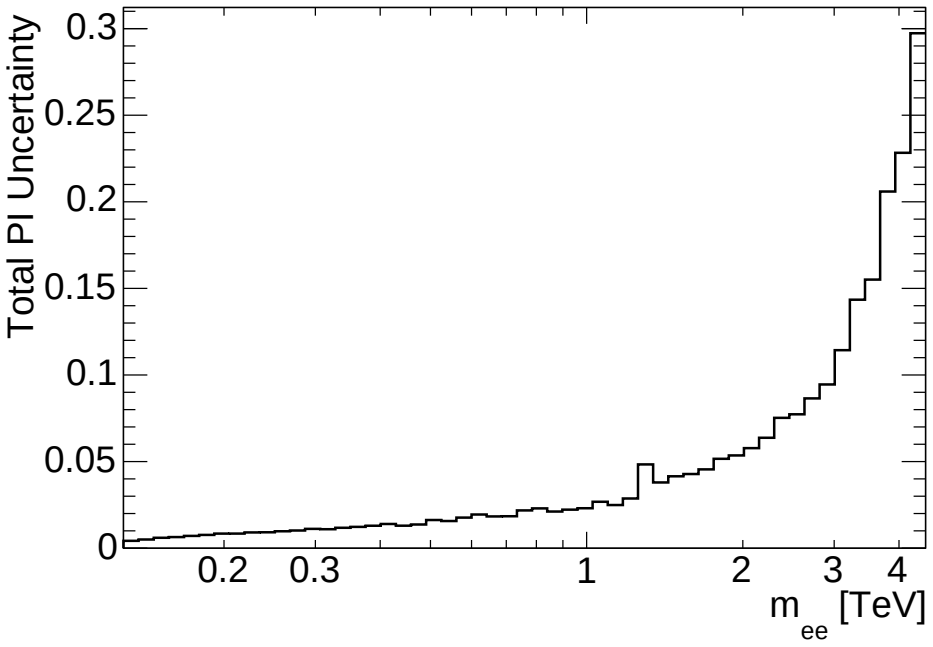

Figure B.6: Systematic uncertainty associated with the photon-induced background normalised to the total SM expectation.

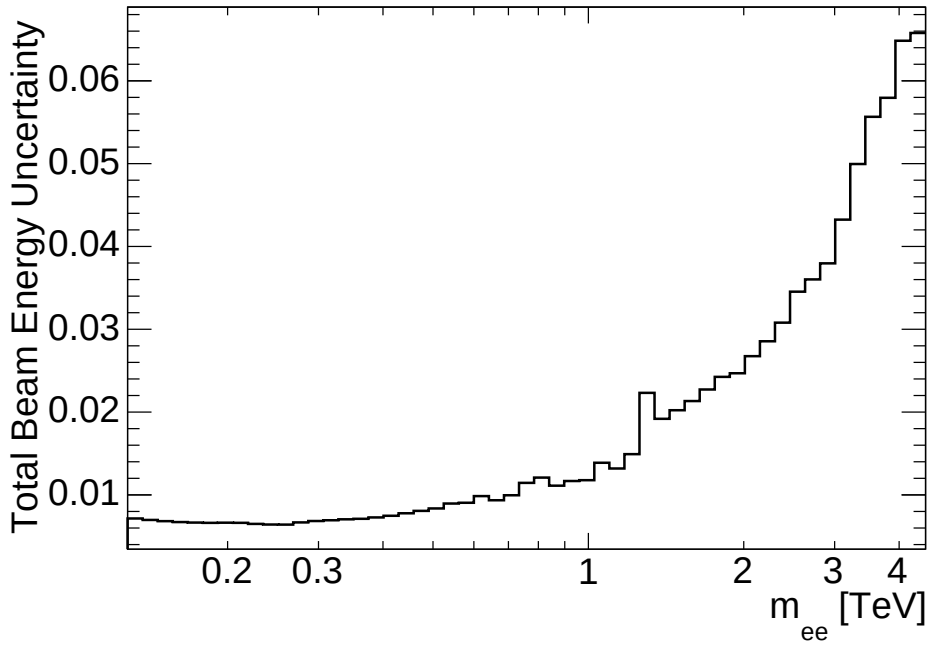

Figure B.7: Beam energy systematic uncertainty as BAT input histogram normalised to the total SM expectation.

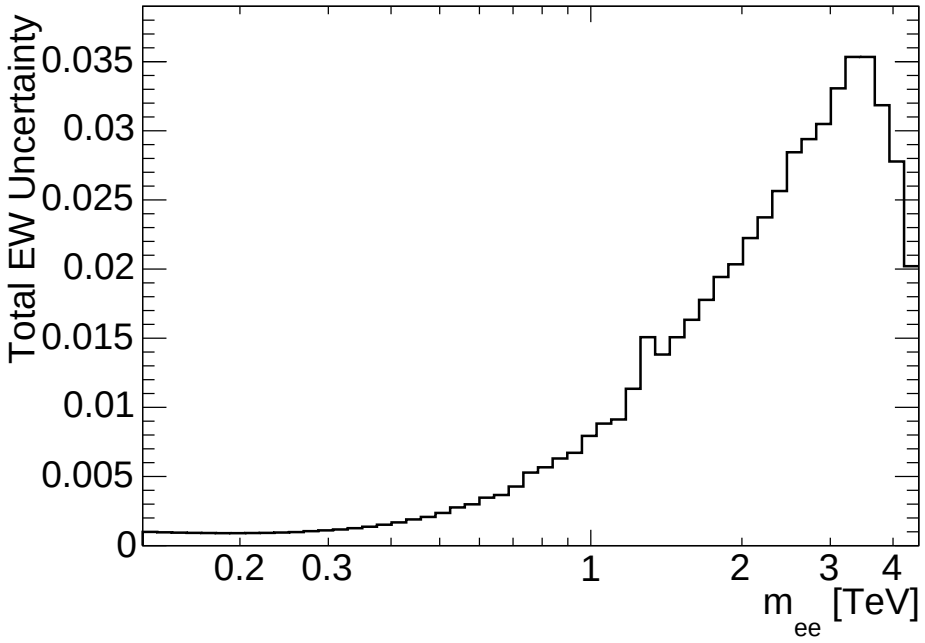

Figure B.8: Higher order electroweak correction systematic uncertainty as BAT input histogram normalised to the total SM expectation.

References

[1] ATLAS Collaboration, G. Aad et al., *Search for high-mass dilepton resonances in pp collisions at $\sqrt{s} = 8\,TeV$ with the ATLAS detector*, arXiv:1405.4123 [hep-ex].

[2] F. Halzen and A. D. Martin, *Quarks and Leptons: An Introductory Course in Modern Particle Physics*. John Wiley and Sons, 1984.

[3] S. L. Glashow, *Partial-symmetries of weak interactions*, Nuclear Physics **22** (1961) no. 4, 579 – 588. http://www.sciencedirect.com/science/article/pii/0029558261904692.

[4] S. Weinberg, *A Model of Leptons*, Phys. Rev. Lett. **19** (1967) 1264–1266. http://link.aps.org/doi/10.1103/PhysRevLett.19.1264.

[5] Particle Data Group Collaboration, K. Olive et al., *Review of Particle Physics*, Chin.Phys. **C38** (2014) 090001.

[6] M. E. Peskin and D. V. Schroeder, *An Introduction to Quantum Field Theory*. Westview Press, 1995.

[7] J. L. Rosner, *The Standard model in 2001*, arXiv:hep-ph/0108195 [hep-ph].

[8] D. Griffiths, *Introduction to Elementary Particles*. Wiley-VCH, 2008.

[9] H. Jones, *Groups, Representations, and Physics*. Taylor and Francis Group, 1998.

[10] ATLAS Collaboration, G. Aad et al., *Observation of a new particle in the search for the Standard Model Higgs boson with the ATLAS detector at the LHC*, Phys.Lett. **B716** (2012) 1–29, arXiv:1207.7214 [hep-ex].

[11] CMS Collaboration, S. Chatrchyan et al., *Observation of a new boson at a mass of 125 GeV with the CMS experiment at the LHC*, Phys.Lett. **B716** (2012) 30–61, arXiv:1207.7235 [hep-ex].

[12] S. D. Drell and T.-M. Yan, *Massive Lepton-Pair Production in Hadron-Hadron Collisions at High Energies*, Phys. Rev. Lett. **25** (1970) 316–320. http://link.aps.org/doi/10.1103/PhysRevLett.25.316.

[13] A. K. Gupta, N. K. Mondal, and S. Raychaudhuri, *Constraining large extra dimensions using dilepton data from the Tevatron collider*, arXiv:hep-ph/9904234 [hep-ph].

[14] S. Dittmaier and M. Huber, *Radiative corrections to the neutral-current Drell-Yan process in the Standard Model and its minimal supersymmetric extension*, JHEP **1001** (2010) 060, arXiv:0911.2329 [hep-ph].

[15] R. Feynman, *The behavior of hadron collisions at extreme energies*, Conf.Proc. **C690905** (1969) 237–258.

[16] R. K. Ellis, W. J. Stirling, and B. Webber, *QCD and Collider Physics*, vol. 8 of *Camb.Monogr.Part.Phys.Nucl.Phys.Cosmol.* Cambridge University Press, Cambridge, 1996.

[17] H. Schellman, *Learn Hadron Collider Physics in 3 Days*, ch. 7, pp. 359–404. 2004. http://particle.physics.ucdavis.edu/workshops/TASI04/schellman.pdf.

[18] T. Han, *Collider phenomenology: Basic knowledge and techniques*, arXiv:hep-ph/0508097 [hep-ph].

[19] G. Altarelli and G. Parisi, *Asymptotic Freedom in Parton Language*, Nucl.Phys. **B126** (1977) 298.

[20] H1 and ZEUS Collaboration, F. Aaron et al., *Combined Measurement and QCD Analysis of the Inclusive $e^{\pm}p$ Scattering Cross Sections at HERA*, JHEP **1001** (2010) 109, arXiv:0911.0884 [hep-ex].

[21] R. Thorne, A. Martin, W. Stirling, and G. Watt, *The Effects of combined HERA and recent Tevatron $W \to l\nu$ charge asymmetry data on the MSTW PDFs*, PoS **DIS2010** (2010) 052, arXiv:1006.2753 [hep-ph].

[22] B. Watt, P. Motylinski, and R. Thorne, *The Effect of LHC Jet Data on MSTW PDFs*, Eur.Phys.J. **C74** (2014) 2934, arXiv:1311.5703 [hep-ph].

[23] ATLAS Collaboration, G. Aad et al., *Measurement of the inclusive $W^{\pm}$ and Z/γ cross sections in the electron and muon decay channels in pp collisions at $\sqrt{s} = 7\,TeV$ with the ATLAS detector*, Phys.Rev. **D85** (2012) 072004,

arXiv:1109.5141 [hep-ex].

[24] A. Martin, W. Stirling, R. Thorne, and G. Watt, *Parton distributions for the LHC*, Eur.Phys.J. **C63** (2009) 189–285, arXiv:0901.0002 [hep-ph].

[25] J. Pumplin, D. Stump, R. Brock, D. Casey, J. Huston, et al., *Uncertainties of predictions from parton distribution functions. 2. The Hessian method*, Phys.Rev. **D65** (2001) 014013, arXiv:hep-ph/0101032 [hep-ph].

[26] *Durham HepData Project PDF Plotter*, Web page. http://hepdata.cedar.ac.uk/pdf/pdf3.html.

[27] A. G. Cohen, D. Kaplan, and A. Nelson, *Progress in electroweak baryogenesis*, Ann.Rev.Nucl.Part.Sci. **43** (1993) 27–70, arXiv:hep-ph/9302210 [hep-ph].

[28] W.-S. Hou, *Source of CP Violation for the Baryon Asymmetry of the Universe*, Chin.J.Phys. **47** (2009) 134, arXiv:0803.1234 [hep-ph].

[29] B. Cleveland, T. Daily, J. Davis, Raymond, J. R. Distel, K. Lande, et al., *Measurement of the solar electron neutrino flux with the Homestake chlorine detector*, Astrophys.J. **496** (1998) 505–526.

[30] J. N. Bahcall and H. A. Bethe, *Solution of the solar-neutrino problem*, Phys. Rev. Lett. **65** (1990) 2233–2235. http://link.aps.org/doi/10.1103/PhysRevLett.65.2233.

[31] T2K Collaboration, K. Abe et al., *Measurement of Neutrino Oscillation Parameters from Muon Neutrino Disappearance with an Off-axis Beam*, Phys.Rev.Lett. **111** (2013) no. 21, 211803, arXiv:1308.0465 [hep-ex].

[32] S. Weinberg, *The cosmological constant problem*, Rev. Mod. Phys. **61** (1989) 1–23. http://link.aps.org/doi/10.1103/RevModPhys.61.1.

[33] T. G. Rizzo, *Z' phenomenology and the LHC*, arXiv:hep-ph/0610104 [hep-ph].

[34] P. Langacker, *The Physics of Heavy Z' Gauge Bosons*, Rev.Mod.Phys. **81** (2009) 1199–1228, arXiv:0801.1345 [hep-ph].

[35] J. J. Aubert et al., *Experimental Observation of a Heavy Particle J*, Phys. Rev. Lett. **33** (1974) 1404–1406. http://link.aps.org/doi/10.1103/PhysRevLett.33.1404.

[36] J. Augustin et al., *Discovery of a Narrow Resonance in e^+e^- Annihilation*, Phys. Rev. Lett. **33** (1974) 1406–1408. http://link.aps.org/doi/10.1103/PhysRevLett.33.1406.

[37] S. W. Herb et al., *Observation of a Dimuon Resonance at 9.5 GeV in 400 GeV Proton-Nucleus Collisions*, Phys. Rev. Lett. **39** (1977) 252–255. http://link.aps.org/doi/10.1103/PhysRevLett.39.252.

[38] UA1 Collaboration, G. Arnison et al., *Experimental Observation of Lepton Pairs of Invariant Mass Around 95 GeV/c^2 at the CERN SPS Collider*, Phys.Lett. **B126** (1983) 398–410.

[39] UA2 Collaboration, P. Bagnaia et al., *Evidence for Z0 –> e+ e- at the CERN anti-p p Collider*, Phys.Lett. **B129** (1983) 130–140.

[40] OPAL Collaboration, G. Abbiendi et al., *Tests of the standard model and constraints on new physics from measurements of fermion pair production at 189 GeV to 209 GeV at LEP*, Eur.Phys.J. **C33** (2004) 173–212, arXiv:hep-ex/0309053 [hep-ex].

[41] P. Langacker, *Z' Physics at the LHC*, arXiv:0911.4294 [hep-ph].

[42] CDF Collaboration, T. Aaltonen et al., *Search for High-Mass e^+ e- Resonances in $p\bar{p}$ Collisions at $\sqrt{s} = 1.96$ TeV*, Phys.Rev.Lett. **102** (2009) 031801, arXiv:0810.2059 [hep-ex].

[43] D0 Collaboration, V. M. Abazov et al., *Search for a heavy neutral gauge boson in the dielectron channel with 5.4 fb-1 of $p\bar{p}$ collisions at $\sqrt{s} = 1.96$ TeV*, Phys.Lett. **B695** (2011) 88–94, arXiv:1008.2023 [hep-ex].

[44] CMS Collaboration, S. Chatrchyan et al., *Search for Resonances in the Dilepton Mass Distribution in pp Collisions at $\sqrt{s} = 7$ TeV*, JHEP **1105** (2011) 093, arXiv:1103.0981 [hep-ex].

[45] CMS Collaboration, S. Chatrchyan et al., *Search for narrow resonances in dilepton mass spectra in pp collisions at $\sqrt{s} = 7$ TeV*, Phys.Lett. **B714** (2012) 158–179, arXiv:1206.1849 [hep-ex].

[46] O. S. Brüning, P. Collier, P. Lebrun, S. Myers, R. Ostojic, et al., *LHC Design Report. 1. The LHC Main Ring*, vol. 1. CERN, Geneva, 2004. http://cds.cern.ch/record/782076.

[47] K. Aamodt et al., *The ALICE experiment at the CERN LHC*, JINST **3** (2008) S08002.

[48] ATLAS Collaboration, *The ATLAS Experiment at the CERN Large Hadron Collider*, J. Instrum. **3** (2008) S08003. 437 p. https://cdsweb.cern.ch/record/1129811.

[49] CMS Collaboration, S. Chatrchyan et al., *The CMS experiment at the CERN LHC*, JINST **3** (2008) S08004.

[50] J. Alves, A. Augusto et al., *The LHCb Detector at the LHC*, JINST **3** (2008) S08005.

[51] AC Team, *The four main LHC experiments*, tech. rep., CERN, June, 1999. http://cds.cern.ch/record/40525.

[52] AC Team, *Diagram of an LHC dipole magnet. Schéma d'un aimant dipôle du LHC*, tech. rep., CERN, June, 1999. https://cds.cern.ch/record/40524.

[53] F. Marcastel, *CERN'S Accelerator Complex*, tech. rep., CERN, Geneva, 2013. http://cds.cern.ch/record/1621583.

[54] M. Lamont, *Status of the LHC*, Journal of Physics: Conference Series **455** (2013) no. 1, 012001. http://stacks.iop.org/1742-6596/455/i=1/a=012001.

[55] J. Wenninger, *Energy Calibration of the LHC Beams at 4 TeV*, Tech. Rep. CERN-ATS-2013-040, CERN, Geneva, May, 2013. https://cds.cern.ch/record/1546734.

[56] ATLAS Collaboration, *ATLAS: Letter of Intent for a General-Purpose pp Experiment at the Large Hadron Collider at CERN*. Letter of Intent. CERN, Geneva, 1992. http://cds.cern.ch/record/291061.

[57] ATLAS Collaboration, *ATLAS inner detector: Technical Design Report, 1*. Technical Design Report ATLAS. CERN, Geneva, 1997. http://cds.cern.ch/record/331063.

[58] ATLAS Collaboration, *ATLAS liquid-argon calorimeter: Technical Design Report*. ATLAS liquid-argon calorimeter: Technical Design Report. CERN, Geneva, 1996. http://cds.cern.ch/record/331061.

[59] ATLAS Collaboration, *ATLAS tile calorimeter: Technical Design Report.* Technical Design Report ATLAS. CERN, Geneva, 1996. http://cds.cern.ch/record/331062.

[60] ATLAS Collaboration, *ATLAS muon spectrometer: Technical Design Report.* Technical Design Report ATLAS. CERN, Geneva, 1997. http://cds.cern.ch/record/331068.

[61] J. Pequenao, *Computer generated image of the whole ATLAS detector*, tech. rep., CERN, Mar, 2008. http://cds.cern.ch/record/1095924.

[62] ATLAS Collaboration, A. Abdesselam et al., *The ATLAS semiconductor tracker end-cap module*, Nucl.Instrum.Meth **A575** (2007) 353–389. http://cds.cern.ch/record/1063618.

[63] ATLAS TRT Collaboration, V. A. Mitsou, *The ATLAS transition radiation tracker*, arXiv:hep-ex/0311058. http://arxiv.org/abs/hep-ex/0311058.

[64] J. Pequenao, *Computer generated image of the ATLAS inner detector*, tech. rep., CERN, March, 2008. http://cds.cern.ch/record/1095926.

[65] M. D. L. Hanlon, *The development of p-type silicon detectors for the high radiation regions of the LHC.* PhD thesis, University of Liverpool, Liverpool, 1998. http://cds.cern.ch/record/784204.

[66] J. Pequenao, *Computer Generated image of the ATLAS calorimeter*, tech. rep., CERN, March, 2008. http://cds.cern.ch/record/1095927.

[67] J. Pequenao, *Computer generated image of the ATLAS Muons subsystem*, tech. rep., CERN, March, 2008. http://cds.cern.ch/record/1095929.

[68] J. Snuverink, *The ATLAS muon spectrometer: commisioning and tracking.* PhD thesis, Twente, Twente University, Enschede, Twente, 2009. http://cds.cern.ch/record/1232051.

[69] L. Evans and P. Bryant, *LHC Machine*, Journal of Instrumentation **3** (2008) no. 08, S08001. http://stacks.iop.org/1748-0221/3/i=08/a=S08001.

[70] C. V et al., *The ATLAS Beam Conditions Monitor*, Journal of Instrumentation **3** (2008) no. 02, P02004. http://stacks.iop.org/1748-0221/3/i=02/a=P02004.

[71] P. Jenni and M. Nessi, *ATLAS Forward Detectors for Luminosity Measurement and Monitoring*, tech. rep., CERN, Geneva, March, 2004. http://cds.cern.ch/record/721908.

[72] ATLAS Collaboration, G. Aad et al., *Improved luminosity determination in pp collisions at $\sqrt{s} = 7\,TeV$ using the ATLAS detector at the LHC*, Eur. Phys. J. **C73** (2013) 2513, arXiv:1302.4393 [hep-ex]. http://arxiv.org/abs/1302.4393.

[73] S. van der Meer, *Calibration of the effective beam height in the ISR*, Tech. Rep. CERN-ISR-PO-68-31. ISR-PO-68-31, CERN, Geneva, 1968.

[74] ATLAS Collaboration, G. Aad et al., *Luminosity Determination in pp Collisions at $\sqrt{s} = 7\,TeV$ Using the ATLAS Detector at the LHC*, Eur.Phys.J. **C71** (2011) 1630, arXiv:1101.2185 [hep-ex].

[75] ATLAS Luminosity Taskforce, *Luminosity Public Results*, Web page, March, 2014. https://twiki.cern.ch/twiki/bin/view/AtlasPublic/LuminosityPublicResults.

[76] ATLAS Collaboration, *ATLAS level-1 trigger: Technical Design Report*. Technical Design Report ATLAS. CERN, Geneva, 1998. http://cds.cern.ch/record/381429.

[77] P. Jenni, M. Nessi, M. Nordberg, and K. Smith, *ATLAS high-level trigger, data-acquisition and controls: Technical Design Report*. Technical Design Report ATLAS. CERN, Geneva, 2003. http://cds.cern.ch/record/616089.

[78] ATLAS Collaboration, G. Aad et al., *Expected Performance of the ATLAS Experiment - Detector, Trigger and Physics*, arXiv:0901.0512. http://arxiv.org/abs/0901.0512.

[79] ATLAS Collaboration, G. Aad et al., *Electron performance measurements with the ATLAS detector using the 2010 LHC proton-proton collision data*, Eur.Phys.J. **C72** (2012) 1909, arXiv:1110.3174 [hep-ex].

[80] W. Lampl, S. Laplace, D. Lelas, P. Loch, H. Ma, et al., *Calorimeter Clustering Algorithms: Description and Performance*. http://cds.cern.ch/record/1099735.

[81] ATLAS Collaboration, G. Aad et al., *Electron efficiency measurements with the ATLAS detector using the 2012 LHC proton-proton collision data*, .

https://cds.cern.ch/record/1706245.

[82] ATLAS Collaboration, G. Aad et al., *Electron reconstruction and identification efficiency measurements with the ATLAS detector using the 2011 LHC proton-proton collision data*, Eur.Phys.J. **C74** (2014) 2941, arXiv:1404.2240 [hep-ex].

[83] T. Sjostrand, S. Mrenna, and P. Z. Skands, *PYTHIA 6.4 Physics and Manual*, JHEP **0605** (2006) 026, arXiv:hep-ph/0603175 [hep-ph].

[84] F. Krauss, *Phenomenology at collider experiments*, Ral summer school lecture notes, 2008. https://www.stfc.ac.uk/PPD/resources/pdf/Krauss_08_Pheno_5.pdf.

[85] S. Agostinelli et al., *Geant4 — A Simulation Toolkit*, Nuclear Instruments and Methods in Physics Research Section A: Accelerators, Spectrometers, Detectors and Associated Equipment **506** (2003) no. 3, 250–303. http://www.sciencedirect.com/science/article/pii/S0168900203013688.

[86] S. Alioli, P. Nason, C. Oleari, and E. Re, *A general framework for implementing NLO calculations in shower Monte Carlo programs: the POWHEG BOX*, JHEP **1006** (2010) 043, arXiv:1002.2581 [hep-ph].

[87] H.-L. Lai, M. Guzzi, J. Huston, Z. Li, P. M. Nadolsky, et al., *New parton distributions for collider physics*, Phys.Rev. **D82** (2010) 074024, arXiv:1007.2241 [hep-ph].

[88] T. Sjostrand, S. Mrenna, and P. Z. Skands, *A Brief Introduction to PYTHIA 8.1*, Comput.Phys.Commun. **178** (2008) 852–867, arXiv:0710.3820 [hep-ph].

[89] P. Golonka and Z. Was, *PHOTOS Monte Carlo: A Precision tool for QED corrections in Z and W decays*, Eur.Phys.J. **C45** (2006) 97–107, arXiv:hep-ph/0506026 [hep-ph].

[90] U. Klein, *Les Houches 2013: Physics at TeV Colliders: Standard Model Working Group Report*, arXiv:1405.1067 [hep-ph].

[91] Y. Li and F. Petriello, *Combining QCD and electroweak corrections to dilepton production in FEWZ*, Phys.Rev. **D86** (2012) 094034, arXiv:1208.5967 [hep-ph].

[92] U. Baur, *Weak Boson Emission in Hadron Collider Processes*, Phys.Rev. **D75** (2007) 013005, arXiv:hep-ph/0611241 [hep-ph].

[93] J. Alwall, M. Herquet, F. Maltoni, O. Mattelaer, and T. Stelzer, *MadGraph 5 : Going Beyond*, JHEP **1106** (2011) 128, arXiv:1106.0522 [hep-ph].

[94] A. Martin, W. Stirling, R. Thorne, and G. Watt, *Uncertainties on alpha(S) in global PDF analyses and implications for predicted hadronic cross sections*, Eur.Phys.J. **C64** (2009) 653–680, arXiv:0905.3531 [hep-ph].

[95] C. Anastasiou, L. J. Dixon, K. Melnikov, and F. Petriello, *High precision QCD at hadron colliders: Electroweak gauge boson rapidity distributions at NNLO*, Phys.Rev. **D69** (2004) 094008, arXiv:hep-ph/0312266 [hep-ph].

[96] S. Alekhin, J. Bluemlein, and S. O. Moch, *ABM11 PDFs and the cross section benchmarks in NNLO*, PoS **LL2012** (2012) 016, arXiv:1302.1516 [hep-ph].

[97] H1 and ZEUS Collaboration, V. Radescu, *Combination and QCD Analysis of the HERA Inclusive Cross Sections*, arXiv:1308.0374 [hep-ex].

[98] R. D. Ball, V. Bertone, S. Carrazza, C. S. Deans, L. Del Debbio, et al., *Parton distributions with LHC data*, Nucl.Phys. **B867** (2013) 244–289, arXiv:1207.1303 [hep-ph].

[99] ATLAS Collaboration, G. Aad et al., *Measurement of the high-mass Drell–Yan differential cross-section in pp collisions at sqrts = 7 TeV with the ATLAS detector*, Phys.Lett. **B725** (2013) 223–242, arXiv:1305.4192 [hep-ex].

[100] A. Martin, R. Roberts, W. Stirling, and R. Thorne, *Parton distributions incorporating QED contributions*, Eur.Phys.J. **C39** (2005) 155–161, arXiv:hep-ph/0411040 [hep-ph].

[101] S. Frixione, P. Nason, and B. R. Webber, *Matching NLO QCD and parton showers in heavy flavor production*, JHEP **0308** (2003) 007, arXiv:hep-ph/0305252 [hep-ph].

[102] S. Frixione and B. R. Webber, *Matching NLO QCD computations and parton shower simulations*, JHEP **0206** (2002) 029, arXiv:hep-ph/0204244 [hep-ph].

[103] S. Frixione, E. Laenen, P. Motylinski, B. R. Webber, and C. D. White, *Single-top hadroproduction in association with a W boson*, JHEP **0807** (2008) 029, arXiv:0805.3067 [hep-ph].

[104] N. Kidonakis, *Two-loop soft anomalous dimensions for single top quark associated production with a W- or H-*, Phys.Rev. **D82** (2010) 054018, arXiv:1005.4451 [hep-ph].

[105] G. Corcella, I. Knowles, G. Marchesini, S. Moretti, K. Odagiri, et al., *HERWIG 6: An Event generator for hadron emission reactions with interfering gluons (including supersymmetric processes)*, JHEP **0101** (2001) 010, arXiv:hep-ph/0011363 [hep-ph].

[106] G. Corcella, I. Knowles, G. Marchesini, S. Moretti, K. Odagiri, et al., *HERWIG 6.5 release note*, arXiv:hep-ph/0210213 [hep-ph].

[107] J. Pumplin, D. Stump, J. Huston, H. Lai, P. M. Nadolsky, et al., *New generation of parton distributions with uncertainties from global QCD analysis*, JHEP **0207** (2002) 012, arXiv:hep-ph/0201195 [hep-ph].

[108] J. Butterworth, E. Dobson, U. Klein, B. Mellado Garcia, T. Nunnemann, J. Qian, D. Rebuzzi, and R. Tanaka, *Single Boson and Diboson Production Cross Sections in pp Collisions at $\sqrt{s} = 7\,TeV$*, Tech. Rep. ATL-COM-PHYS-2010-695, CERN, Geneva, August, 2010. https://cds.cern.ch/record/1287902.

[109] ATLAS Collaboration, G. Duckeck et al., *ATLAS computing: Technical design report*. https://cds.cern.ch/record/837738.

[110] *ATLAS Luminosity Calculator*, Web page. https://atlas-lumicalc.cern.ch/.

[111] ATLAS Collaboration, Z. Marshall, *Simulation of Pile-up in the ATLAS Experiment*, J.Phys.Conf.Ser. **513** (2014) 022024.

[112] W. Stirling, *Parton Luminosity and Cross Section Plots*, Web page, 2012. www.hep.ph.ic.ac.uk/~wstirlin/plots/plots.html.

[113] CDF Collaboration, T. Aaltonen et al., *Search for new particles decaying into dijets in proton-antiproton collisions at $\sqrt{s} = 1.96\,TeV$*, Phys.Rev. **D79** (2009) 112002, arXiv:0812.4036 [hep-ex].

[114] ATLAS Collaboration, G. Aad et al., *Search for New Particles in Two-Jet Final States in 7 TeV Proton-Proton Collisions with the ATLAS Detector at the LHC*, Phys.Rev.Lett. **105** (2010) 161801, arXiv:1008.2461 [hep-ex].

[115] ATLAS Collaboration, G. Aad et al., *Search for high-mass resonances decaying to dilepton final states in pp collisions at $\sqrt{s} = 7\,TeV$ with the ATLAS detector*,

JHEP **1211** (2012) 138, arXiv:1209.2535 [hep-ex].

[116] J. Neyman and E. S. Pearson, *On the Problem of the Most Efficient Tests of Statistical Hypotheses*, Royal Society of London Philosophical Transactions Series A **231** (1933) 289–337.

[117] A. Caldwell, D. Kollar, and K. Kroninger, *BAT - The Bayesian Analysis Toolkit*, Computer Physics Communications **180** (2009) 2197, arXiv:0808.2552.

[118] ATLAS Collaboration, G. Aad et al., *Search for high mass dilepton resonances in pp collisions at $\sqrt{s} = 7\,TeV$ with the ATLAS experiment*, Phys.Lett. **B700** (2011) 163–180, arXiv:1103.6218 [hep-ex].

[119] ATLAS Collaboration, G. Aad et al., *Search for new particles in events with one lepton and missing transverse momentum in pp collisions at $\sqrt{s} = 8\,TeV$ with the ATLAS detector*, JHEP **1409** (2014) 037, arXiv:1407.7494 [hep-ex].

[120] CMS Collaboration, S. Chatrchyan et al., *Search for physics beyond the standard model in final states with a lepton and missing transverse energy in proton-proton collisions at $\sqrt{s} = 8\,TeV$*, arXiv:1408.2745 [hep-ex].

[121] CMS Collaboration, S. Chatrchyan et al., *Search for Resonances in the Dilepton Mass Distribution in pp Collisions at $\sqrt{s} = 8\,TeV$*. http://cds.cern.ch/record/1519132.

[122] ATLAS Collaboration, G. Aad et al., *Search for high-mass dilepton resonances in 20 fb^{-1} of pp collisions at $\sqrt{s} = 8$ TeV with the ATLAS experiment*. https://cds.cern.ch/record/1525524.

List of acronyms

ALICE A Large Ion Collider Experiment

ATLAS A Toroidal LHC ApparatuS

BAT Bayesian Analysis Toolkit

BCM Beam Condition Monitor

BSM Beyond the Standard Model

CC Charged Current

CERN European Organisation for Nuclear Research (formerly: Conseil Europeen pour la Recharche Nucleaire)

CMS Compact Muon Solenoid

CSC Cathode Strip Chamber

DQ Data Quality

DY Drell-Yan

ECAL Electromagnetic CALorimeter

EF Event Filter

EW ElectroWeak

FEWZ Fully Exclusive WZ production

FCAL Forward CALorimeter

GPD General Purpose Detector

GRL Good Run List

HERWIG Hadron Emission Reactions With Interfering Gluons

HLT High Level Trigger

IP Interaction Point

LEP Large Electron-Positron Collider

LHC Large Hadron Collider

LO Leading Order

LUCID LUminosity measurement using Cherenkov Integrating Detector

MC Monte Carlo

MDT Monitored Drift Tubes

MS Muon Spectrometer

NC Neutral Current

NLO Next to Leading Order

NNLO Next to Next to Leading Order

PDF Parton Distribution Function

PI Photon-Induced

POWHEG POsitive Weight Hardest Emission Generator

PRW Pile-up ReWeighting

QCD Quantum ChromoDynamics

QED Quantum ElectroDynamics

SCT SemiConductor Tracker

SM Standard Model

SSM Sequential Standard Model

TRT Transition Radiation Tracker

List of figures

List of tables